Investigation of interactions in two-dimensional electron gases with angular resolved photoemission spectroscopy

THÈSE N^{O} 6572 (2015)

PRÉSENTÉE LE 25 AOÛT 2015

À LA FACULTÉ DES SCIENCES DE BASE
LABORATOIRE DE SCIENCE À L'ÉCHELLE NANOMÉTRIQUE
PROGRAMME DOCTORAL EN PHYSIQUE

ÉCOLE POLYTECHNIQUE FÉDÉRALE DE LAUSANNE

POUR L'OBTENTION DU GRADE DE DOCTEUR ÈS SCIENCES

PAR

Carola STRAßER

acceptée sur proposition du jury:

Prof. V. Savona, président du jury
Prof. K. Kern, directeur de thèse
Prof. F. Baumberger, rapporteur
Prof. J. H. Dil, rapporteur
Prof. F. Reinert, rapporteur

ÉCOLE POLYTECHNIQUE
FÉDÉRALE DE LAUSANNE

Suisse
2015

Abstract

In this thesis, angular resolved photoemission spectroscopy (ARPES) is used to study the electronic structure of different two-dimensional electron systems (2DES). This technique is very surface sensitive and the most direct method to probe the surface band structure of a system. In addition to the band dispersion also signatures from interactions can be detected with ARPES. A careful analysis of peak position and linewidth gives access to the complex self-energy Σ, which describes the energy renormalization and the lifetime of the electrons due to many-body interactions. By using circularly polarized light it is possible to excite electrons selectively and to extract additional information about the electronic states in the surface.

2DESs exist typically either at interfaces or at surfaces. We put our focus on the surface states of topological insulators and investigate Bi_2Te_2Se and $TiTe_{1.5}Se_{0.5}$. The first is known to be a topological insulator with the Fermi energy located in the bulk band gap. A time-dependent doping behavior is observed and we show that the Coulomb interaction in this material is strongly dependent on the charge carrier density and not negligible for very low concentrations. $TiTe_{1.5}Se_{0.5}$ was predicted to be a topological insulator. We are able to present the surface band structure, but due to the fact that ARPES can only probe the occupied states it is impossible to see the predicted topological surface states.

The third system under investigation is a monolayer of epitaxial graphene on SiC(0001) decorated by small amounts of Tl adatoms. ARPES measurements at very low temperature and very low impurity concentrations show that Tl adatoms not only give rise to electron doping but have also a large effect on the quasiparticle scattering rate. The adatoms introduce disorder and act on the graphene electronic structure both as Coulomb long-range scatterers as well as short-range scatterers with a δ-like potential. We show that also for charged impurities short-range scattering can play an important role and is not always negligible. By modeling the self-energy for long- and short-range scattering, we are able to extract a strong short-range scattering potential $\delta = -3.2 \pm 1\,\mathrm{eV}$. A detailed understanding of the underlying scattering mechanisms in graphene is very important for the development of novel impurity-graphene-based electronics.

ARPES experiments are also performed on the surface alloys on Ag(111). For these measurements, we use circularly polarized light and take advantage of the fact that the interaction between light and matter changes for different polarizations. Surface alloys on Ag(111) are formed by depositing 1/3 of a monolayer of bismuth or antimony on the clean Ag(111) surface, where every third Ag atom is replaced by such an alloy atom. These systems are known for their Rashba type spin splitting and the resulting chiral spin structure in the two-dimensional (2D) band structure. We show that circular dichroism (CD) in the angular distribution of the photoelectrons depends strongly on the experimental setup and the energy of the photons. Only under special circumstances it is possible to use CD to access the orbital angular momentum and — in systems with high spin-orbit coupling — maybe even the spin texture of the surface. Because of the final state effects, interpretation of CD data is quite complicated and has to be done very cautiously.

Keywords: ARPES
two-dimensional electron systems
graphene
topological insulator
surface alloys
scattering mechanisms
Coulomb interaction
orbital angular momentum
spintronics

Zusammenfassung

In der vorliegenden Arbeit wird die elektronische Struktur von verschiedenen zweidimensionalen (2D) Elektronensystemen mit winkelaufgelöster Photoemission untersucht. Diese Technik ist sehr oberflächensensitiv und ermöglicht es direkt die Oberflächenbandstruktur eines Materials zu messen. Nicht nur die Dispersion der Bänder sondern auch elektronische Wechselwirkungen können gemessen werden. Durch sorgfältige Bestimmung von Peakpositionen und -breiten kann man die komplexe Selbstenergie Σ berechnen, die den Einfluss der Wechselwirkung von Elektronen mit anderen Teilchen auf die Bindungsenergie und die Lebensdauer der Elektronen beschreibt. Wählt man die zirkular polarisiertes Licht, ist es sogar möglich gezielt Elektronen anzuregen und zusätzliche Information über die elektronischen Zustände an der Oberfläche zu gewinnen.

2D Elektronensysteme existieren typischerweise entweder an Grenzflächen oder an Oberflächen. Wir legen unseren Fokus auf die Oberflächenzustände von topologischen Isolatoren und untersuchen Bi_2Te_2Se und $TiTe_{1.5}Se_{0.5}$. Das erste Material ist bekannt als toloplogischer Isolator, bei dem die Fermienergie in der Bulkenergielücke liegt. Wir beobachten ein zeitabhängiges Dopingverhalten und wir können zeigen, dass die Coulomb-Wechselwirkung in diesem Material stark von der Ladungsträgerdichte abhängt und für kleine Ladungsträgerdichten nicht vernachlässigbar ist. $TiTe_{1.5}Se_{0.5}$ wurde als neuer topologischer Isolator vorgeschlagen. Wir präsentieren die Oberflächenbandstruktur, allerdings ist es nicht möglich die topologischen Oberflächenzustände zu beobachten, da mit Photoemission unbesetzte Elektronenzustände nicht gemessen werden können.

Das dritte System, das wir im Folgenden untersuchen werden, ist eine Monolage von epitaktischem Graphen auf SiC(0001) bedeckt mit einer kleinen Menge von Thalliumadatomen. Photoemissionsmessungen bei sehr tiefen Temperaturen und sehr kleinen Konzentrationen zeigen, dass Thalliumatome nicht nur Elektronen abgeben sondern auch einen großen Einfluss auf die Streurate der Elektronen haben. Die Adatome bringen Unordnung in das System und wirken auf die elektronischen Struktur von Graphen sowohl als Coulomb-Streuer als auch als kurzreichweitige Streuzentren mit einem δ-förmigen Streupotential. Wir zeigen, dass auch für geladene Streuzentren kurzreichweitige Streumechanismen eine wichtige Rolle spielen können und nicht immer vernachlässigbar sind. Durch Modellierung der Selbstenergie für lang- und kurzreichweitige Streuung sind wir in der Lage für das δ-Potential einen Wert von $\delta = -3.2 \pm 1\,\mathrm{eV}$ zu extrahieren. Die zugrunde liegenden Streumechanismen in Graphen zu verstehen ist ein sehr wichtiges Ziel im Hinblick auf die Entwicklung von elektronischen Bauteilen, die auf mit Störstellen dekoriertem Graphen basieren.

Außerdem zeigen wir Ergebnisse von Experimenten an Oberflächenlegierungen auf Ag(111). Für diese Messungen verwenden wir zirkular polarisiertes Licht und nutzen den Vorteil, dass sich die Wechselwirkung zwischen Licht und Materie für verschiedene Polarisationen ändert. Oberflächenlegierungen auf Ag(111) bilden sich, wenn man 1/3 Monolage Wismuth oder Antimon auf eine saubere Silberoberfläche aufdampft. Dabei wird jedes dritte Silberatom von einem solchen Legierungsatom ersetzt. Diese Legierungen sind bekannt für die Rashba-artige Spinaufspaltung und die daraus resultierende chirale Spin-Struktur in der 2D Bandstruktur. Wir zeigen, dass zirkularer Dichroismus in der Winkelverteilung der Photoelektronen stark von der Geometrie des Experiments und der Energie der Photonen abhängt. Nur unter speziellen Umständen ist es möglich zirkularen Dichorismus zu benutzen um experimentellen Zugang zum Bahndrehmoment und — in Systemen mit hoher Spin-Bahn-Wechselwirkung — vielleicht sogar zur Spintextur der Oberfläche zu bekommen. Aufgrund des starken Einflusses der Endzustände ist die Interpretation von Dichroismusdaten höchst komplex und muss besonders vorsichtig durchgeführt werden.

Stichwörter: winkelaufgelöste Photoemission
zweidimensionale Elektronensysteme
Graphen
Topologischer Isolator
Oberflächenlegierungen
Streuungsmechanismen
Coulomb Wechselwirkung
Bahndrehmoment
Spintronik

Contents

1 **Introduction** **1**

2 **Scientific Background** **5**

2.1 Electrons in low dimensions 5
  2.1.1 Electrons in solids 6
  2.1.2 Surface states 7
2.2 Spin-polarized surface states 8
  2.2.1 The Rashba effect 9
  2.2.2 Topological insulators 11
2.3 Surface states vs. 2D states 13
  2.3.1 Surface alloys 14
  2.3.2 Graphene 15

3 **Experimental Techniques** **19**

3.1 Photoemission spectroscopy 19
  3.1.1 The photoemission process 19
  3.1.2 Quasiparticle picture 23
3.2 Angular resolved photoemission 25
3.3 Core level spectroscopy 29

4 **Coulomb interaction in topological insulators** **31**

4.1 Bi_2Se_3, Bi_2Te_3 and Bi_2Te_2Se 32
4.2 Doping behavior 33
4.3 Coulomb interaction at low charge carrier densities 34
4.4 Discussion 38

5 Surface band structure of $\mathbf{TiTe_{1.5}Se_{0.5}}$ 43
5.1 Search for new topological materials 43
5.2 Crystal structure 44
5.3 Electronic structure 45
5.4 Discussion 48

6 Scattering mechanisms in thallium doped epitaxial graphene 51
6.1 Impurities on graphene 52
6.2 Doping effect of Tl adatoms 53
6.3 Linewidth analysis and theoretical description 56
  6.3.1 Long-range scattering 56
  6.3.2 Short-range scattering 58
6.4 Graphene as topological insulator 59
6.5 Discussion 61

7 Circular dichroism in the band structure of surface alloys 63
7.1 Circular dichroism in the angular distribution of photoelectrons 64
7.2 Photoemission experiments 65
7.3 Theoretical description 67
7.4 Orbital angular momentum in surface alloys 69
7.5 Photon-energy dependence 70
7.6 Discussion 72

8 Summary and Outlook 75
8.1 Summary 75
8.2 Outlook 76
  8.2.1 Topological insulators 77
  8.2.2 Circular dichorism measurements 78
  8.2.3 Graphene 78

Chapter 1

Introduction

“God made the bulk; surfaces were invented by the devil.” [1] As the quote from Wolfgang Pauli hypothesizes, the physics of surfaces is quite different compared to the bulk. One reason for the different behavior is the dimensional constraints of the electrons. Since the beginning of the 20th century it is known that in low-dimensional materials the limits of classical physics are reached. As soon as the dimensions of an object are smaller than the wavelength of the conduction electrons, quantum phenomena emerge. Surfaces can be described as two-dimensional electron systems (2DESs) where the electrons are confined in one direction but can move freely in the plane. Some famous examples for physical effects that can only be explained by a quantum-mechanical picture like the quantum Hall effect are found in 2DES [2–4].

For investigation of such phenomena, accurate fabrication of low-dimensional materials is required. The enormous development of technical knowledge and experimental methods in the last decades allows scientists to design and investigate new low-dimensional systems with fascinating properties that can be described by quantum mechanics. It is possible to study materials at the nanoscale in real space with atomic force microscopy (AFM) and scanning tunneling microscopy (STM). For determination of the atomic structure at the surface low energy electron diffraction is a very useful technique. To explore the electronic structure at the surface x-ray photoelectron spectroscopy (XPS) and angular resolved photoemission spectroscopy (ARPES) are the methods of choice. In this thesis, the electronic properties of 2DESs localized at the surface are investigated using ARPES.

In particular, the focus of this thesis lies on topological insulators (TIs). TIs are materials that have an insulating bulk but are conducting on their surface. The conducting surface states are very interesting due to their spin polarization and their robustness against defects. Many of them have a linear dispersion relation and are very promising candidates for fast spintronic devices. Common theoretical descriptions of TIs are formulated in terms of single-particle quantum mechanics [5]. Usually, the electron-electron interaction is neglected since the dielectric constant in TIs is extremely high and the interaction is effectively screened. However, the strength of the interaction is also dependent on the charge carrier density. If the charge carrier density is low enough, electron-electron interaction can play an important role - it can even turn the topological phase into an insulating ground state [6]. Therefore, it is a crucial issue to understand the interplay between strong electron-electron interactions and the topological surface states. While studying the Coulomb interaction in Bi_2Te_2Se it was found that the bands are substantially affected by the electron-electron interaction. Depending on the charge carrier density the band structure is renormalized and in addition an aging-induced band bending was observed.

Beside the detailed investigation of known TIs, it is also very important to look for new topological materials. In this thesis first results of an ARPES study of $TiTe_{1.5}Se_{0.5}$, which is assumed to be a TI, are presented. Due to their high atomic spin-orbit coupling (SOC) strength transition metal dichalcogenides are very promising candidates for materials with a topologically nontrivial surface state. Some theoretical studies predicted $TiS_{2-2x}Te_{2x}$ to turn into a TI for $0.48 < x < 0.80$. To check if $TiTe_{1.5}Se_{0.5}$ behaves similarly the first ARPES measurements on this system were performed. The band structure looks promising, but to identify the systems as a TI, further studies are necessary since the assumed topological surface states are located in the unoccupied states.

In addition to TIs, epitaxial graphene on SiC(0001) was studied. It was shown that chemical doping is an efficient method to tune the electronic structure and to shift the Fermi level in either direction. However, every time dopants are deposited on graphene they unavoidably introduce disorder and change the charge carrier mobility. A very important issue for the development of future electronic devices based on impurities on graphene is the ability to predict the involved scattering mechanisms and account for them accordingly. In general, long-range scattering is said to be the dominant scattering mechanism in graphene transport devices. For thallium atoms on graphene, which can be considered paradigm long-range scatterers, significant scattering contributions from short-range scattering were found. Using signatures of quasiparticle scattering in the photoemission spectral function and a self-energy model for both long-range and short-range scattering mechanisms, Tl adatoms could be identified also as efficient short-range scattering centers.

In the third topic of this thesis, the use of circular dichroism (CD) measurements as a method to access the orbital angular momentum (OAM) or even the spin of a surface state is discussed. Surface alloys on the Ag(111) surface show a large spin splitting in the surface states due to the Rashba-Bychkov effect [7]. Besides the great potential for applications in the field of spintronics, these alloys are also perfect test systems for surfaces with giant spin splitting. By using circularly polarized light one can measure a CD signal in the surface alloys on Ag(111). It was found that the CD signal is strongly dependent on the photon-energy and does not directly contain information about the spin. Instead of following the spin direction, CD is dominated by the geometry of the experimental setup, by the dipole selection rules and by the final state.

This thesis is organized as follows: In Chap. 2 an introduction to the scientific background required for the understanding of the experimental results is given. Chap. 3 describes the technical background and the experimental setups that were used to carry out the experiments. The results from the studies about the electron-electron interaction in TIs are presented in Chap. 4. In Chap. 5 the surface band structure of a titanium dichalogenide is introduced. Chap. 6 is dedicated to our experimental results on Tl doped epitaxial graphene. In Chap. 7 the possibility of accessing the spin orientation in surface states using circularly polarized light in ARPES experiments is discussed. Finally, a detailed summary of the main results is given in Chap. 8 and some ideas for future research projects based on the previous chapters will be presented.

Chapter 2

Scientific Background

In solid state physics the main focus is on crystals and the investigation of their properties. Scientists are interested in electrical, magnetic, optical, or mechanical characteristics. In addition to the crystal structure, the electronic properties of a solid are of special interest. The latter are determined by the electrons inside the crystal. Moreover the potential in which the electrons are embedded plays a very important role. For example, electrons in a low-dimensional environment behave quite different from free electrons.

2.1 Electrons in low dimensions

Generally, electrons in solids move in three dimensions, but by reducing the spatial characteristics of the crystal, for example, by creating surfaces or interfaces, electrons can be forced to stay in less than three dimensions. If they are confined to certain directions or planes, their energy E and momentum $\vec{k}$ in the relevant direction will be quantized. In a quantum well, electrons are confined in only one direction, in a quantum wire they are confined in two directions and in a quantum dot confinement exists in all three directions.

The simplest case of electron confinement is shown by an electron in a potential well in one dimension. The potential well of the length L is shown in Fig. 2.1 (a) and can be described by [8, 9]

$$V(x) = \begin{cases} 0, & \text{for } 0 < x < L \\ \infty, & \text{else} \end{cases}$$

Solving Schrödinger's equation for this potential gives the same dispersion relation as

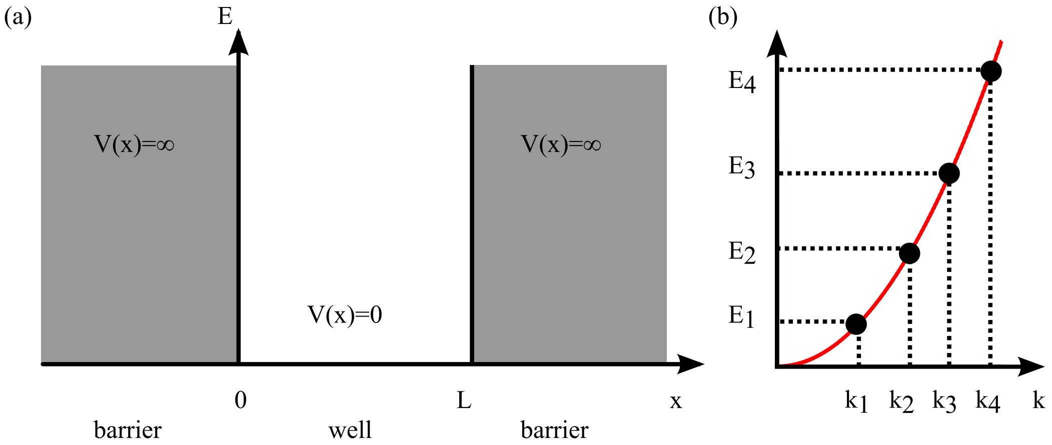

Figure 2.1: One-dimensional quantum well: (a) Outside the one-dimensional well the barriers have infinitely large potential, while inside the potential is zero. (b) The energy of an electron in a one-dimensional quantum well (black circles) and a free electron (red line), both depend on the wave vector in the same way [see Eq. 2.1]. However, the electron in the well may only have certain, discrete energy levels.

for free electrons

$$E(\vec{k}) = \frac{\hbar^2 \vec{k}^2}{2m} \tag{2.1}$$

but for the potential well there are only discrete momentum values allowed that satisfy $k = n\pi/L$ with $n \in \mathbb{N}$ [see Fig. 2.1 (b)]. $\hbar$ represents Planck's constant h divided by 2π and m is the mass of the electron.

Confined electron systems are of particular interest because they give access to special physical phenomena that are based on quantum physics. Particularly, in two dimensions i.e. at surfaces or interfaces, many interesting physical effects can happen, like the (fractional) quantum Hall effect [10]. In this thesis we are focusing on electrons at surfaces, i.e. on 2DES.

2.1.1 Electrons in solids

In a very simple picture solids can be modeled by atoms of the same kind that come close together. Electrons in solids feel a periodic potential $V(\vec{r}) = V(\vec{r} + \vec{R})$ where $\vec{R}$ gives the lattice periodicity [8]. The solutions for the Schrödinger equation with such a potential are Bloch waves $\Psi_k(\vec{r}) = u_k(\vec{r})e^{i\vec{k}\vec{r}}$ with $u_k(\vec{r}) = u_k(\vec{r} + \vec{R})$. Accordingly, also the energy eigenstates show periodic behavior and the free electron parabola is duplicated at every lattice vector, as shown schematically in Fig. 2.2 (a) and (b).

Since the band structure is periodic in $\vec{R}$ it is sufficient to draw the bands only in the

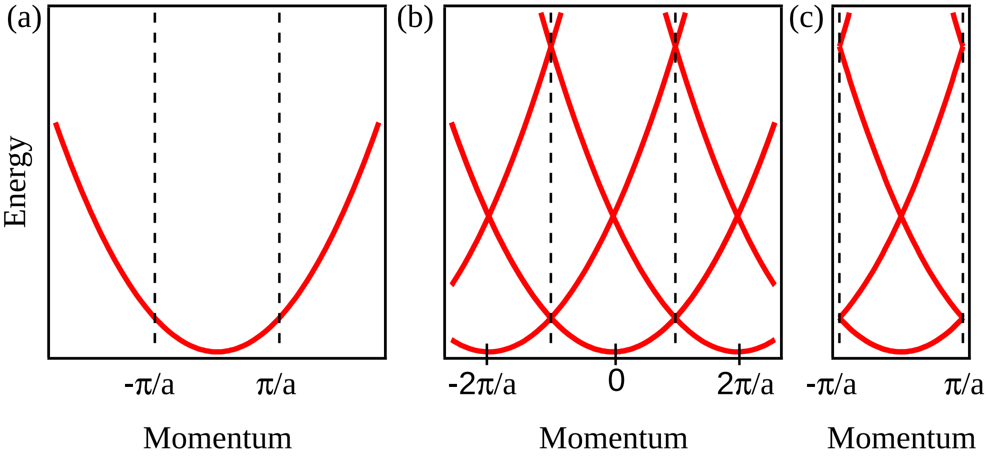

Figure 2.2: Electronic band structure for electrons in a periodic potential: (a) The free electron parabola. (b) Periodic zone scheme of the band structure in a solid. (c) Reduced zone scheme in the first Brillouin zone.

first Brillouin zone like in Fig. 2.2 (c). Due to the lattice potential small energy gaps will be opened at the crossing points which lead to the electronic band structure that consists of the allowed bands and band gaps [not shown in Fig. 2.2].

2.1.2 Surface states

As shown in Sec. 2.1.1 the solutions to the Schrödinger equation in an infinite crystal are Bloch waves. By creating a surface the potential deviates from its perfect periodicity. For a potential that is not perfectly periodic there are additional solutions for the Schrödinger equation that can be divided into two groups: (i) the Bloch waves, which decay exponentially into vacuum [see Fig. 2.3 (a)] and (ii) states, which are damped exponentially into the vacuum as well as into the bulk. The latter are the so-called surface states and are schematically drawn in Fig. 2.3 (b). Their energy eigenvalues are located in the projected bulk band gap and their wave vector $k_{||}$ is imaginary. Electrons within these surface states are strongly confined in the direction perpendicular to the surface, whereas they can propagate freely within the surface. Therefore, surface states constitute a 2DES.

In the discussion of surface states one distinguishes Shockley states from Tamm states [11]. In principle both are terms for the description of the same physical phenomenon, i. e. surface states but the mathematical approach is different. Shockley surface states are described in the framework of the nearly free electron model for clean and ideal surfaces and exist simply due to crystal termination at the surface [12]. In contrast, the Tamm states

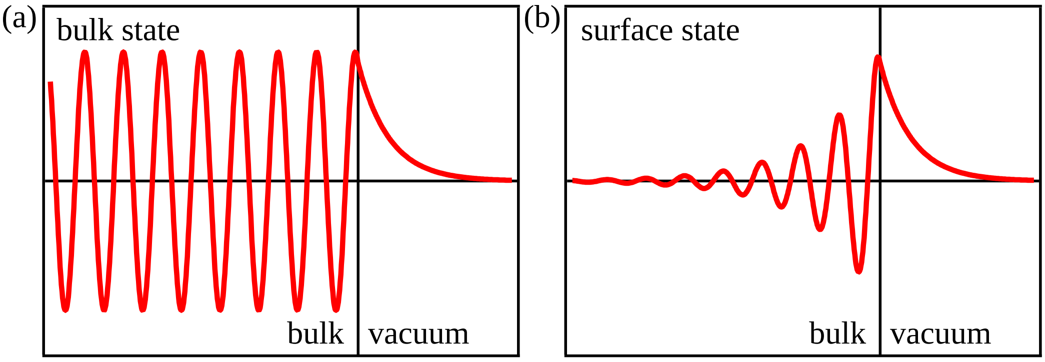

Figure 2.3: (a) In a semi-infinite crystal the Bloch waves are exponentially damped in the vacuum region. (b) Due to the missing periodicity at the surface there are additional solutions to the Schrödinger equation, which have imaginary wave vector. They decay exponentially into vacuum as well as into the bulk.

are obtained using the tight binding model. The existence of Tamm surface states implies a considerable perturbation of the potential in the surface region due to reconstruction [13]. In addition to these surface states, there are surface resonances that decay exponentially into vacuum but show a sizable amplitude in the bulk.

2.2 Spin-polarized surface states

In general, in a three-dimensional (3D) solid time reversal $[E(\uparrow,\vec{k}) = E(\downarrow,-\vec{k})]$ as well as spatial inversion symmetry $[E(\uparrow,\vec{k}) = E(\uparrow,-\vec{k})]$ are fulfilled. The combination of both gives rise to Kramers spin degeneracy [14], expressed as

$$E(\uparrow,\vec{k}) = E(\downarrow,\vec{k})$$

However, SOC can lift the spin degeneracy if one of the symmetries is broken [15]. In current surface science research, there are two main classes of spin-polarized surface states [16,17] that are of interest; Rashba-split surface states and the surface states in TIs. In the next two sections both will be introduced and compared to each other.

2.2.1 The Rashba effect

The spatial inversion symmetry of a solid can be easily broken, for example, due to bulk inversion asymmetry in noncentrosymmetric semiconductors. As a consequence of SOC the spin degeneracy can be removed [18–20]. Also, a structural inversion asymmetry, which is caused simply by the presence of the surface in a semi-infinite crystal, breaks space inversion symmetry. Electronic states at the surface feel the structural inversion asymmetry and become spin-polarized due to SOC. The case in two dimensions (2D) is usually considered as the Rashba-effect [7, 21]. For the theoretical description of the spin splitting in a 2DES with inversion asymmetry along the z-direction, the Rashba Hamiltonian is added to the quasi-free 2D electron gas confined in the $(x; y)$-plane. The Hamiltonian describes SOC in propagating electronic states and is given by

$$H_{RB} = \alpha_R \vec{\sigma}(\vec{k}_{||} \times \vec{e}_z) \tag{2.2}$$

with the Rashba parameter α_R determined by the potential gradient perpendicular to the 2DES, the Pauli matrices $\vec{\sigma} = (\sigma_x, \sigma_y, \sigma_z)$, the electron momentum in the plane $\vec{k}_{||}$ and the unit vector $\vec{e}_z$ perpendicular to the plane of the 2DES. Solving the Schrödinger equation for the Rashba Hamiltonian gives

$$E(k_{||}) = E_0 + \frac{\hbar^2 k_{||}^2}{2m^*} \pm \alpha_R k_{||} = E_0 + \frac{\hbar^2}{2m^*}\left(k_{||} \pm k_R\right)^2$$

for the energy dispersion. The resulting band structure consists of two parabolas with an effective mass m^*, which are shifted by the momentum offset $\pm k_R = \alpha_R m^*/\hbar^2$ from the original momentum. However, at high symmetry points the dispersion has to be spin degenerate because of time reversal symmetry. A typical dispersion is schematically drawn in Fig. 2.4 (a) and (b).

A third characteristic parameter that results from the momentum offset k_R is the so called Rashba energy $E_R = \hbar^2 k_R^2/(2m^*) = m^* \alpha_R^2/(2\hbar^2)$. It describes the energy difference between the band extremum and the crossing point at the high symmetry point. A cut through the band structure at a constant energy above the crossing point gives two concentric circles [see Fig. 2.4(c)]. Due to the vector product in Eq. 2.2 the spin vector is expected to be entirely in-plane, i.e. perpendicular to $\vec{e_z}$ and perpendicular to the momentum $k_{||}$ of the electron. Consequently the spin vector points tangential along the constant energy contours; it rotates clockwise on the inner circle and counterclockwise on the outer one.

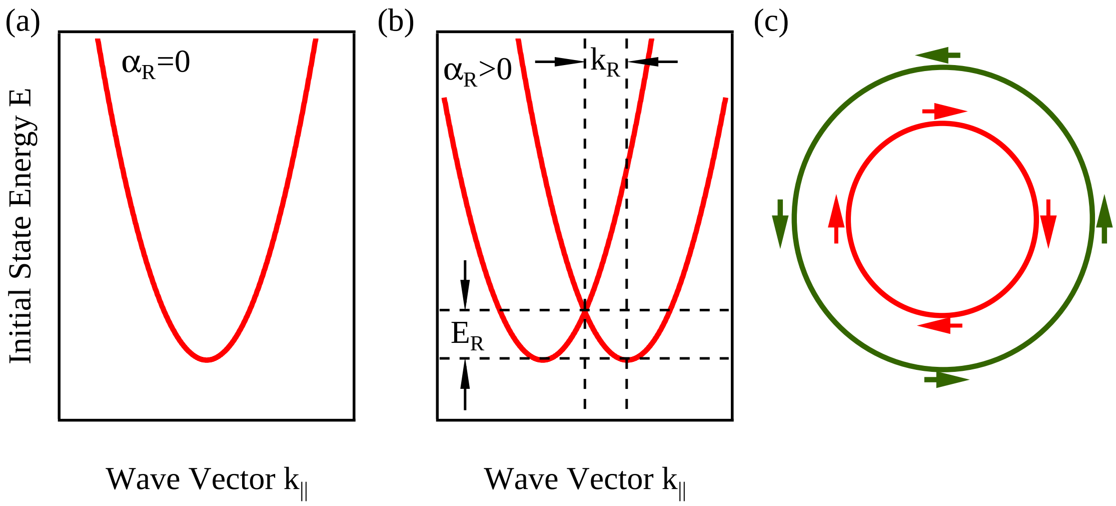

Figure 2.4: Energy dispersion of a 2D electron gas (a) without and (b) with Rashba SOC. The characteristic parameters of the model, E_R and k_R, are marked. (c) Spin polarisation on a constant energy contour above the crossing point.

However, in total the system is not magnetic since an integration over the whole reciprocal space gives no net spin.

The first example for a Rashba-split surface state is the one on Au(111). LaShell *et al.* [22] observed an energy splitting that is proportional to the wave vector and about 110 meV at the Fermi level. Different approaches have been chosen to tune [23] or to enhance the spin splitting for example by adsorption of Ar, Kr or Xe [24].

In order to be able to manipulate the spin splitting at the surface in a desired fashion, it is very important to understand the underlying mechanism. In a very simple picture the spin-splitting of the 2D states caused by the Rashba effect can be seen as a spin-polarization due to the Zeemann effect. The effective magnetic field B_{eff} would be $\vec{k}$-dependent and described by $\alpha_R(\vec{k}_{||} \times \vec{e}_z)$. The direction of B_{eff}, i.e. the spin quantization axis, would be given by the vector product and the size of the splitting is determined by the Rashba constant α_R, which is proportional to the gradient of the potential confining the electrons to the surface. But within the framework of the quasi-free electron model typical values for the spin splitting would be several orders of magnitude smaller than experimentally observed [25, 26]. Using a simple tight binding model it was shown [25] that α_R is proportional to the atomic SOC and an asymmetry parameter γ.

Recently, it was proposed by Park *et al.* [27] that the Rashba-type spin-splitting is a consequence of the existence of local OAM. The local OAM is the quantum number given by the orbital angular momentum operator **L**, often called the magnetic quantum number. The OAM produces an asymmetric charge distribution by inducing small dipoles. The electric field perpendicular to the surface aligns the electric dipole and results in chiral OAM states and the spin splitting. The characteristic chiral spin structure is formed through SOC and is claimed to be a consequence of the chiral OAM. The authors show that by considering the OAM as the origin of the spin splitting the predicted size of the spin splitting is much closer to the measured value. They confirm by them that the atomic SOC size plays an important role.

In addition to the effort towards a theoretical understanding, it was found that the spin splitting can be enhanced by corrugation of the surface potential and outward relaxation of some atoms [28]. It is also possible to transfer the spin-polarized surface states on a semiconducting substrate [29]. The main goal in the field of spintronics is to tune the spin splitting via an external electrical field. The Rashba effect on semiconducting substrates seems to build the basis for many different electrical devices like the spin field effect transistor of Datta and Das [30].

2.2.2 Topological insulators

The surface states in a 3D TI constitute another spin-polarized 2DES that is discussed in this section. A TI is a material that has an energy gap in its bulk but is conducting at the edges. In three dimensions, the bulk itself is insulating but the surfaces are metallic. There are also 2D TIs, which have one-dimensional gapless edge states. As explained in Sec. 2.1.2 surface states exist in the energy band gap of the bulk material. There are topologically trivial and non-trivial surface states. The non-trivial ones are called topological surface states. Trivial surface states arise from and end in the same bulk band and they exist also in projected bulk band gaps. Topological surface states, however, connect two different bulk bands and the corresponding band gap is a true bulk band gap. In addition, this band gap is inverted, which means that the order of conduction and valence band in a TI is reversed compared to the band structure of trivial materials. By connecting a TI with a normal insulator like, for example, vacuum the topology of the band structure changes at the interface. In order to restore the order of the bulk bands the band gap will be closed and reopened, which results directly in metallic edge states at the surface.

In general, the surface states in a TI are Dirac-like and show conical dispersion but in contrast to graphene the bands are spin-polarized because of the strong SOC. The broken inversion symmetry at the surface dictates the spin-splitting of the surface states.

Time-reversal symmetry gives rise to the so-called spin-momentum locking; all electrons with spin up (down) travel to the right (left) side. Accordingly, chiral spin textures are found in momentum space with the sense of chirality reversed across the Dirac point. Electrons in the surface states are immune to back scattering from disorder and non-magnetic impurities, since for back scattering the electron would need to flip also its spin. Due to this fact, such surface states are extremely robust to disorder and they are called 'topologically protected'. An idealized band structure for a TI is shown in Fig. 2.5. The simplest criterion to identify topologically non-trivial surface state is an odd number of Fermi level crossings between the Brillouin zone center and the boundary. In the simple example in Fig. 2.5, it would be just one crossing.

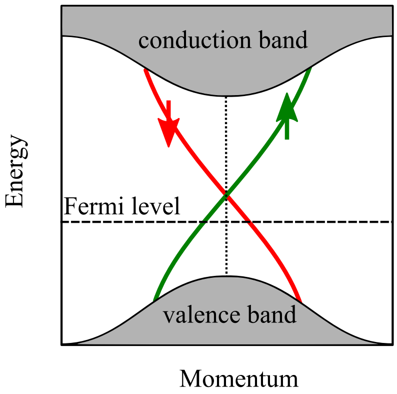

Figure 2.5: An idealized band structure for a topological insulator. The Fermi level falls within the bulk band gap which is traversed by topologically-protected surface states.

A TI in 2D is also known as a quantum spin Hall insulator. This state was theoretically predicted in 2005 [31] for graphene at low temperatures. Since the SOC in carbon atoms is very small, the predicted gap is only of the order of some μeV and experimentally not observable. Subsequently, Bernevig *et al.* [32] claimed that there is a quantum spin Hall state in HgCdTe quantum well structures. One year later the first experimental observation of a TI was reported in that system [33]. Several materials of 2D TIs have been proposed theoretically [31,32,34].

Theoretical predictions about topological surface states were also made for several 3D materials [35,36] like $Bi_{1-x}Sb_x$ and strained HgTe and α-Sn [37]. The first experimental discovery of a 3D TI was reported in 2008 by Hsieh *et al.* [38]. For $Bi_{1-x}Sb_x$ five Fermi level crossings were found.

Shortly later many theoretically predictions for simpler versions of 3D TIs were published. For example, Bi_2Te_3, Sb_2Te_3 [39] and Bi_2Se_3 [40] should show a large bulk band gap and a gapless surface state consisting of only one single Dirac cone at the Brillouin zone center. Indeed, the linear dispersion relation of these surface states were subsequently observed in ARPES experiments [40, 41]. Since then, the field has expanded at a rapid pace [42–46]; many new compounds are predicted to be topologically non-trivial [47, 48] and some already experimentally proven [5, 49, 50].

One obstacle in real TIs is the high conductivity of the intrinsically doped bulk due to unavoidable defects and vacancies formed during the growth procedure. In Bi_2Se_3, for example, Se vacancies are responsible for the doping level of the bulk. The challenge in every experiment is to distinguish between surface and volume effects. For transport measurements in highly doped TIs, differentiation can be quite difficult or even impossible. Therefore, a TI with a large bulk band gap and the Fermi level inside the gap would be desirable. There are different approaches to solve this problem like, for example, reducing bulk carrier density by doping [51, 52]. One possibility is to mix the elements and get materials that fulfill the requirements, like Bi_2Te_2Se [53–55]. Another option is to reduce the thickness of the sample in order to increase the surface-to-volume ratio. For such nanofabrication three main methods are used; mechanical exfoliation [56], growing nanoplates and nanoribbons by vapor-liquid-solid synthesis [57], and growth of TI nanostructures by molecular beam epitaxy (MBE). The last approach allows for layer by layer growth with large areas, high crystalline quality, and accurate thickness and chemical composition from one to several quintuple layers (QLs) [58].

The surface states of TIs are not only of fundamental importance but have also great potential applications. Despite disorder due to impurities they are predicted to stay metallic even at $T = 0$ because of forbidden back scattering [59]. Due to the dissipation-less transport the edge states of TIs are of huge interest for room temperature spin-based electronic devices [60] and applications in quantum computation [46, 61]. In addition, the helical surface states of TIs could provide access to novel physical phenomena like Majorana fermions [62].

2.3 Surface states vs. 2D states

In addition to topological surface states, we investigated 2DESs of two other types. We had a closer look at the electronic structure of surface alloys on Ag and we studied the effect of impurity scattering in the band structure of graphene. All systems of interest in this work are treated as 2D but the way they are fabricated and their resulting properties are quite different. Surface alloys on Ag, for example, show spin splitting due to the Rashba effect and the graphene band structure is spin degenerate. Building a surface alloy on Ag shows consequences for the first few atomic layers at the surface whereas graphene, being exactly one atom thick, is a perfect 2D crystal. The electrons in graphene behave like massless particles while the electronic states in the surface alloys show parabolic dispersions. In the following section both systems are introduced and their basic principles and properties are presented.

2.3.1 Surface alloys

Surface alloys on Ag(111) are known for their huge Rashba-type spin splitting in the surface states [63, 64]. For the preparation of the surface alloys a third of a monolayer of Bi or Sb is deposited on the clean Ag(111) surface. Every third atom in the Ag(111) surface is replaced by an alloy atom and a long range ordered surface alloy is formed. The resulting $(\sqrt{3} \times \sqrt{3})$R30° structure is shown in Fig. 2.6.

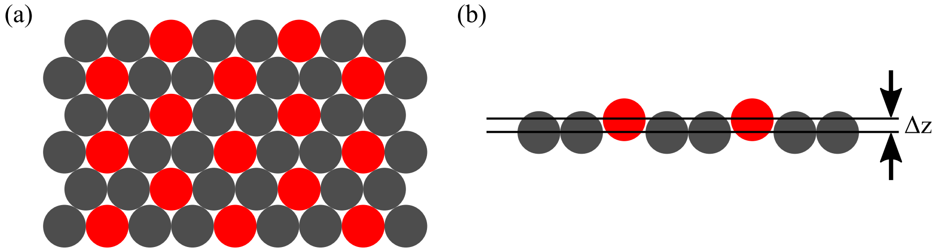

Figure 2.6: Surface alloys on Ag(111): (a) Top view and (b) side view of the $(\sqrt{3}\times\sqrt{3})$R30° structure formed by surface alloys. Every third silver atom (grey) is replaced by an alloy atom (red). The relaxation out of the surface plane is described by Δz.

The band structure of the surface alloys has been extensively investigated and discussed in literature [28,65]. The dispersion shows two spin-polarized bands with the characteristic momentum offset k_R. The surface alloy Bi/Ag(111) shows a huge spin splitting of $E_R = 200\,\text{meV}$. The spin-splitting mechanism and the origin of the huge Rashba energies is not completely understood but it was shown that there are three important ingredients; structural inversion symmetry, atomic SOC and the outward relaxation of the alloy atoms. With increasing relaxation Δz the asymmetry grows and the resulting spin splitting gets larger [25, 28, 66]. It was theoretically shown that the orbital character of the bands is determined by the relaxation, which varies for different alloy atoms.

In addition to the orbital character, the spin structure is affected by the corrugation of the surface potential. Surface alloys show not only in-plane but also out-of-plane spin components [64,67]. This can be explained by an in-plane inversion asymmetry that results in an in-plane component of the potential gradient at the surface [68].

All these extra features of the spin splitting are not included in the original Rashba model. However, for building spintronic devices it would be very desirable to have one combined theory describing all ingredients and features of the spin splitting mechanism. A more detailed understanding of tuning the spin splitting would allow one to fabricate all different kinds of devices with the proper spin textures for any application.

2.3.2 Graphene

The last candidate for a 2DES in this work is the perfect 2D crystal found in the carbon allotrope graphene. It is one single atomic plane of graphite and consists of sp^2 bonded carbon atoms arranged in a honeycomb lattice.

The theoretical description of a single layer of graphite was already presented in 1947 by P. R. Wallace [69], but it was believed for a long time that it would be very unstable and impossible to isolate. In 2004, Novoselov and Geim succeeded in isolating a single layer of graphene. They used the micromechanical exfoliation procedure, also known as the 'Scotch tape technique' and transferred the graphene sheet onto a SiO_2 substrate [70]. After the successful experimental isolation of graphene the research on this material increased rapidly. Many interesting effects could be shown like, for example, the anomalous integer quantum Hall effect in graphene [71, 72]. Single layers of graphite were known before, but the breakthrough was given by the fact that graphene on SiO_2 shows an optical contrast that makes it easy to differentiate single and double layer graphene. For their “groundbreaking experiments regarding the two-dimensional material graphene” Novoselov and Geim received the Nobel prize in physics in 2010.

The electrons in graphene behave like massless particles and can be described by the Dirac equation. Due to the presence of two equivalent sublattices [see Fig. 2.7(a)], the wave function shows 2-spinor character and determines the electronic properties. Graphene has two π-bands that touch each other exactly at the Fermi energy at the $\overline{\mathrm{K}}$-points — the six corners of the Brillouin zone [Fig. 2.7(b)] and behaves like a semi-metal. These points are the so-called Dirac points. Close to those points, the bands disperse linearly and the band structure has the shape of a cone [see Fig. 2.7(c)], where the band velocity is about $v_F \approx 10^6\,\mathrm{m/s}$. The dispersion can be described by the following equation:

$$E(k_{||}) = \hbar v_F k_{||}$$

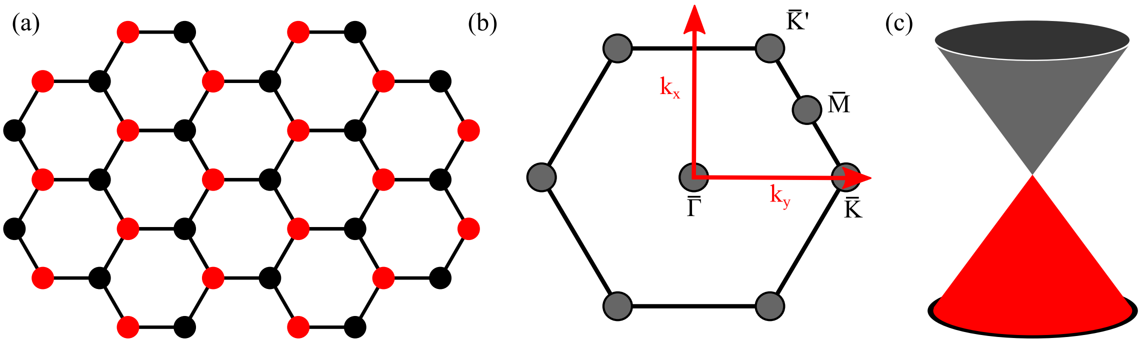

Figure 2.7: Structure of graphene: (a) two equivalent sublattices shown in red and black result in graphene's honeycomb lattice, (b) the corresponding hexagonal Brillouin zone with the most important high symmetry points indicated. (c) Close to the $\overline{\mathrm{K}}$-point the band structure can be approximated by a cone.

Current research on graphene can be divided into two section. One is dealing with the fundamental properties and interesting quantum effects that can be observed in graphene. The other section is involved in pushing graphene further in the direction of applications in electronic devices. But in this field, there are some major problems and questions to solve: It is still not clear what causes the minimum conductivity of $4\ e^2/h$ in graphene [73, 74]. A possible explanation could be the charge puddles in graphene sheets that give rise to higher scattering rate [75]. Another problem is the missing energy band gap in graphene and the resulting low ratios between the 'on' and 'off' state in a field effect transistor built out of graphene [73].

Graphene production

In principle, there are three main approaches to produce graphene [9]: Pulling one single layer from graphite, which is known as mechanical exfoliation, or growing a layer of carbon on a substrate either via epitaxial growth or via chemical vapor deposition (CVD).

Exfoliation: To get one single layer of graphene by exfoliation, multiple peeling steps with an adhesive tape until only one is left are required. After cleaving, the flakes are transferred onto a SiO_2 substrate where the number of layers can be determined with an optical microscope. This method results in flakes with a lateral size of about one millimeter [76]. Exfoliated graphene samples show very high quality and high charge carrier mobility and are the best for proof-of-principle devices in basic research. However, this technique is not suitable for large scale production of graphene.

Epitaxy: Graphene can be grown on various metallic substrates by CVD or epitaxially on a semi-insulating substrate like silicon carbide (SiC) by high temperature annealing. Already decades before the discovery of graphene in 2004, it was known that hydrocarbons can be cracked on catalytic metal surfaces. In particular, it was shown that CVD-graphene grows well on Ni [77–79], Rh [80], Ru [80], Ir [81, 82] and Pt [80, 83, 84]. The advantage of that method is the self-limiting character which leads exactly to one layer of carbon atoms. However for many applications the metallic substrate is undesirable.

A more promising way to build graphene devices on a large scale is the epitaxial growth on SiC wafers. Silicon has a higher vapor pressure and leaves the carbon atoms at the surface. By heating a SiC wafer to temperatures above 1100°C in ultra high vacuum (UHV) graphene is formed on the surface [85]. Its thickness, electron mobility and charge carrier density depends very much on which side of the SiC wafer is used for graphene formation. The growth on SiC(000$\bar{1}$) — the carbon-terminated or C-face — results in rotationally disordered multilayer graphene due to the weak interaction between the graphene layers and the substrate. Due to this rotational disorder the layers are electronically decoupled and show pretty high carrier mobilities that are comparable with isolated graphene sheets [86, 87]. However, controlling the thickness is quite limited on that side [88, 89].

On the opposite side — the silicon-terminated or Si-face — graphene grows in large sheet and covers whole terraces [89–92]. However, the commercially available SiC wafers have typically a lot of scratches on this surface, which have to be removed by hydrogen etching at elevated temperatures. After etching away several hundred nanometers the surface show large and clean terraces with a width of 1500 Å and a step height of only one unit cell [93, 94]. The following annealing step can either take place in UHV or in 900 mbar Ar. Graphitization of SiC in UHV is accompanied by a considerable roughening of the surface. This can be avoided by annealing in Ar at elevated temperatures, which results in step bunching and much larger terraces [95]. In both cases, the first carbon layer that is formed has a honeycomb structure, but does not show graphene-like electronic properties. Since every third atom of the carbon layer is sp^3 hybridized and covalently bound to the substrate the π-bands cannot be formed [96]. The growth process is schematically drawn in Fig. 2.8.

In addition, this so-called zerolayer forms a $(6\sqrt{3} \times 6\sqrt{3})\mathrm{R}30°$ reconstruction with respect to the SiC substrate [88, 91, 98–100]. With increasing temperature further carbon layers will be formed. The second carbon layer is called monolayer graphene [see Fig. 2.8 (b)] and shows a Dirac cone at the $\overline{\mathrm{K}}$-point. However, the band structure contains

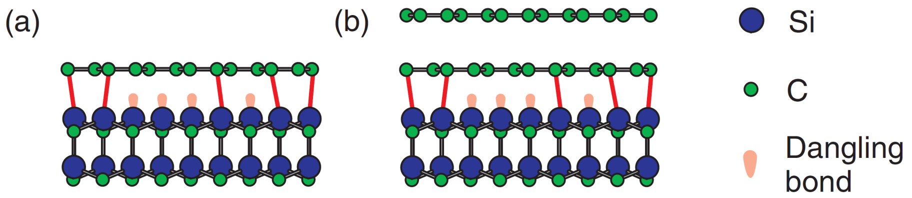

Figure 2.8: Side view models for (a) the $(6\sqrt{3} \times 6\sqrt{3})$R30° reconstruction of SiC(0001) (called zerolayer) and (b) epitaxial monolayer graphene (taken from [97]).

signatures of the substrate. Due to charge transfer from the substrate to the graphene layer the Dirac point is about 420 meV below the Fermi level [97,101–103] and the charge carrier mobility is quite low compared to exfoliated graphene [104]. Since nucleation of a new graphene layer starts at step edges, Ar-annealed samples are much more homogeneously covered [95]. By choosing the right annealing temperature and duration the number of graphene layers can be controlled quite easily.

Chapter 3

Experimental Techniques

3.1 Photoemission spectroscopy

Photoemission spectroscopy (PES) is based on the photoelectric effect discovered by H. Hertz in 1887 [105]. About 20 years later Einstein was able to explain this effect by postulating the quantum nature of light [106], for which he was awarded the Nobel prize in physics in 1921. In the following sections an introduction to this experimental technique and a theoretical description are given.

3.1.1 The photoemission process

Light exists as discrete quantized packets called photons, with an energy $\hbar\omega$. If they impinge on a surface and their energy is larger than a characteristic value Φ, called the work function, they release electrons with kinetic energy E_{kin} from the surface. If E_{kin} is measured by an analyzer, the binding energy E_B of the electron can be determined via

$$E_B = \hbar\omega - \Phi - E_{kin} \tag{3.1}$$

For photoemission measurements the work function of the spectrometer has to be used. Sample and spectrometer are usually in electrical contact and thus the Fermi level is aligned. All relevant energies involved in the photoemission process are shown in Fig. 3.1. Note that E_B is referenced to the Fermi level (E_F is equivalent to zero binding energy), while the kinetic energy is measured with respect to the vacuum level. Depending on the energy of the incident photons there are two different types of photoemission spectroscopy experiments: For the excitation of valence electrons, photons in the ultraviolet

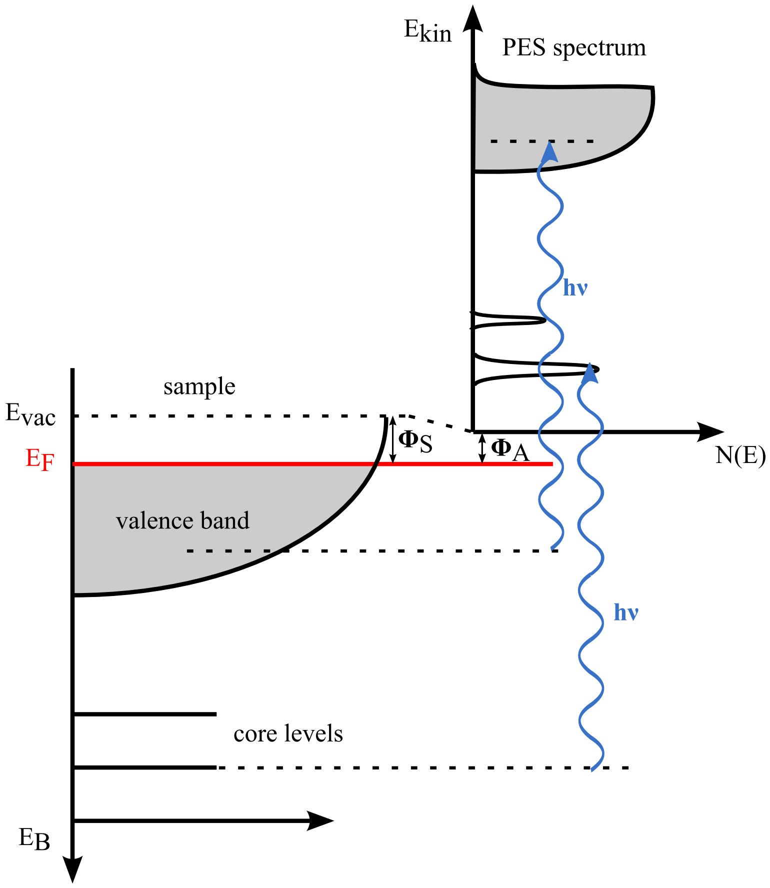

Figure 3.1: Schematic illustration of the energies involved in a photoelectron emission process from a solid. $N(E)$ is the energy distribution of the photoemitted electrons. After [107].

(UV) range are used (ultraviolet photoemission spectroscopy, UPS) whereas the use of x-rays gives access to the core levels, electronic states with much higher binding energy (x-ray photoemission spectroscopy, XPS).

Since Eq. 3.1 is only valid for electrons that did not experience any inelastic event while leaving the material, the probing depth of those techniques can be estimated by the mean free path λ of the electrons which gives the average distance electrons travel without energy loss. It is a measure for the escape depth of the electrons in a solid. For the relevant energies in PES the electrons can be described as a free electron gas. In this case λ depends only on the electron concentration. Since this is roughly equal in all materials the mean free path follows a universal curve that is shown in Fig. 3.2. This curve can be described

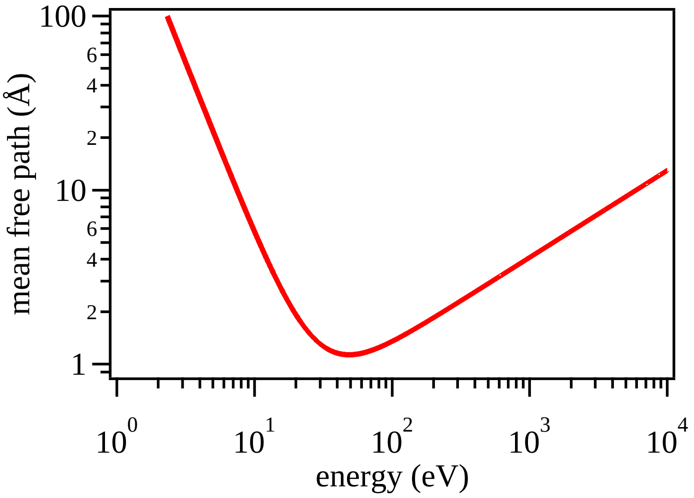

Figure 3.2: Universal curve: Mean free path as function of energy, calculated using Eq. 3.2. The escape depth of the electrons in a solid is almost independent of the material. For the relevant energies the mean free path is about several Å.

by the phenomenological function [108]

$$\lambda(E) = \frac{538}{E^2} + 0.41\sqrt{aE} \tag{3.2}$$

where a is the thickness of a monolayer in nm. The curve has a broad minimum in the energy range of 50-100 eV. Using those energies for PES means that the escaping electrons originate from the first few atomic layers at the surface. This makes PES a very surface sensitive technique.

The photoemission of an electron [Eq. 3.1] can be described in a simple picture as follows: A photon impinges on a surface of a solid and excites an electron via the photoelectric effect. The excited electron escapes into the vacuum while energy and momentum have to be conserved. Since the photon momentum is small compared to the momentum of the electron $\vec{k}$, it can be neglected. The resulting direct transition is possible in a crystal lattice, where a lattice vector can compensate for the missing momentum [compare Sec. 2.1.1]. For a quantitative interpretation of photoemission experiments a more elaborate picture of the photoemission process is needed.

There are two basic approaches to describe the photoemission process theoretically: The rather simple three-step model and the more realistic one-step model. The following theoretical description is based on the references [9, 107, 109]. Within the framework of the three-step model the process is decomposed into three independent steps; (1) electron excitation, (2) electron propagation to the surface and (3) escape through the surface into vacuum [see Fig. 3.3]. Here it has to be pointed out that only elastically scattered electrons are of interest since only those carry information about the initial state in the solid. The measured photocurrent I is proportional to the product of the probability of the photoexcitation, the probability of the electron traveling to the crystal-vacuum interface without being scattered, and the transmission function for the interface.

The separation into three independent steps is somewhat artificial. In the so-called one-step model this is eliminated and the whole photoemission process is considered as one single step. It describes the excitation from an initial Bloch state into a damped final state near the surface. This damping takes care of the short mean free path of the electrons in a solid.

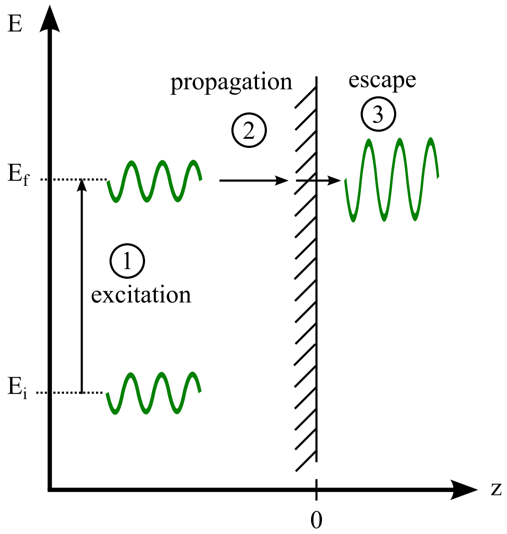

Figure 3.3: Schematic drawing of the three-step model. The photoemission process is divided into three steps; (1) photoexcitation, (2) electron propagation to the surface and (3) escape through the surface into vacuum.

The calculation of the photocurrent is based on Fermi's Golden Rule. For making the calculation feasible the sudden approximation [107] is mostly used. Here, the electron is assumed to immediately exit the surface of the material, without interacting with the remaining electrons and the photohole it leaves behind. The photocurrent is then proportional to the transition probability ω_{fi} from the initial Ψ_i to the final state Ψ_f. Using the dipole approximation gives [107]

$$I \propto \frac{2\pi}{\hbar} |\langle \Psi_f | \vec{A}\vec{p} | \Psi_i \rangle|^2 \delta(E_f - E_i - \hbar\omega)$$

To simplify the transition matrix element a one-electron view is taken for the initial and final state wave function. The initial state can be written as a product of the orbital $\Phi_{i,\vec{k}}$ from which the electron is excited, and the wave function of the remaining electrons:

$$\Psi_i^N = \Phi_{i,k}\Psi_i^k(N-1)$$

Accordingly, the final state is written as a product of the wave function of the photoemitted electron $\Phi_{f,E_{kin}}$ and that of the remaining $(N-1)$ electrons:

$$\Psi_f^N = \Phi_{f,E_{kin}}\Psi_f^k(N-1)$$

The square of the absolute value of the wave function of the remaining electrons gives the spectral function, i.e. $\sum |\langle\Psi_f^k(N-1)|\Psi_i^k(N-1)\rangle|^2 = A(\vec{k},E)$, and the photocurrent turns into

$$I \propto \sum_{f,i,\vec{k}} |\langle\Phi_{f,E_{kin}}|\vec{r}|\Phi_{i,k}\rangle|^2 A(\vec{k},E)f(E,T)$$

where $f(E,T) = (e^{\beta(E-\mu)+1})^{-1}$ is the Fermi-Dirac distribution function that accounts for the occupation of the electronic states with $\beta = (k_B T)^{-1}$, the Boltzmann constant k_B and the chemical potential μ. The spectral function can be related to the single particle Green's function $G(\vec{k},E)$ via

$$A(\vec{k},E) = \frac{1}{\pi}\mathrm{Im}\left(G(\vec{k},E)\right)$$

The Green's function for a system with non-interacting electrons is given by the formula $G_0(\vec{k},E) = 1/(E - E_{\vec{k}}^0 - i\gamma)$, where γ is a infinitesimally small number and $E_{\vec{k}}^0$ is the dispersion $E_{\vec{k}}^0 = \hbar^2\vec{k}^2/(2m^*)$. The corresponding spectral function in this case is a δ-function $A_0(\vec{k},E) = \frac{1}{\pi}\delta(E - E_{\vec{k}}^0)$.

3.1.2 Quasiparticle picture

So far, all formulas were based on the independent electron approximation, which covers a single electron moving in an effective potential $U_{eff}(\vec{r})$ of the atomic cores and the remaining $(N-1)$ electrons with the resulting bare band dispersion $E_{\vec{k}}^0$. For a complete description of an electron in a solid, one has to account also for many-body effects, resulting in the independent electron picture breaking down. However, the properties of a system with interacting electrons, called a 'Fermi liquid', can be mapped onto those of a system of non-interacting electrons by a formalism of Landau. The bare electron combined with many-body interactions are handled as new particles, so-called 'quasi-particle'. The main conclusions of the independent electron approximation remain valid. The spectral properties measured by photoemission spectroscopy of a Fermi liquid differ in four respects from the free electron gas [107]: (1) The energy of the interacting system ($E_{\vec{k}}$) is renormalized relative to that of the non-interacting system ($E^0_{\vec{k}}$). (2) The quasi-particles have a finite lifetime. (3) There is an incoherent background due to electron-hole pairs. (4) The height of the Fermi step is reduced.

In systems where many-body interactions are taken into account, it is useful to introduce the so-called self-energy $\Sigma(\vec{k},E)$, which accounts for the renormalization of the electron energy. The Green's function turns into $G(\vec{k},E) = \frac{1}{E-E^0_{\vec{k}}-\Sigma(\vec{k},E)}$ and the spectral function for an interacting system is given by

$$A(\vec{k},E) = \frac{1}{\pi}\frac{Im\left(\Sigma(\vec{k},E)\right)}{\left[E - E^0_{\vec{k}} - Re\left(\Sigma(\vec{k},E)\right)\right]^2 + \left[Im\left(\Sigma(\vec{k},E)\right)\right]^2} \tag{3.3}$$

In the simplest case, $\mathrm{Im}(\Sigma)$ is constant and $\mathrm{Re}(\Sigma) = 0$. The spectral function is then a Lorentzian at $E^0_{\vec{k}}$ with full width at half maximum $\Gamma = 2\mathrm{Im}(\Sigma)$. The real part of Σ causes deviations from the bare energy dispersion $E^0_{\vec{k}}$ and the imaginary part is responsible for the linewidth. The latter includes the intrinsic linewidth as well as broadening due to interactions. $E^0_{\vec{k}}$ is solely determined by the symmetries of the lattice potential. All the influences of many-body interactions like electron-electron and electron-phonon scattering can be expressed in terms of the complex self-energy Σ.

With ARPES one yields information about the properties of the quasi-particles, i.e. one measures the renormalized dispersion. Due to the high resolution of state-of-the-art analyzers a very accurate determination of the photoemission linewidth is possible and ARPES became a powerful tool for the investigation of many-body interactions in solids. For two- or one-dimensional electronic states the measured linewidth corresponds to the width of the hole state and equals the imaginary part of the self-energy. In this case the full-width-at-half-maximum (FWHM) of the photoemission peaks is related to the quasiparticle lifetime τ via $\tau = \hbar/\Gamma$. The quasiparticle lifetime is a sum of three main contributions

$$\Gamma = \Gamma_{e-e} + \Gamma_{e-ph} + \Gamma_{e-imp}$$

where Γ_{e-e} is the electron-electron scattering, Γ_{e-ph} the electron-phonon scattering and

Γ_{e-imp} the impurity scattering [110].

For an electron at the Fermi level, $\Gamma_{e-e} = 0$ when $T = 0$, which means there is no phase space for any scattering events and the lifetime of the electron is infinite. At energies $E < E_F$, the scattering rate is proportional to $(E - E_F)^2$. At finite temperature there will be partially occupied electronic levels in a shell of width $k_B T$ about E_F. The scattering rate is then proportional to $(k_B T)^2$. The total scattering rate due to electron-electron interaction is therefore

$$\Gamma_{e-e} = 2\beta[(\pi k_B T)^2 + (E - E_F)^2] \tag{3.4}$$

with the electron-electron interaction constant β. In the case of electron-phonon scattering not only the lifetime is affected but also the energy dispersion. The band renormalization due to electron-phonon scattering can be expressed as a change of the electronic velocity $v(k) = 1/\hbar(\partial E/\partial k)$. The renormalized velocity can be calculated via [111]

$$v(k) = \frac{1}{1+\lambda} v_0(k)$$

with the velocity of the non-interacting case $v_0(k) = 1/\hbar(\partial E_0/\partial k)$ and the electron-phonon coupling constant λ. Electron-phonon interactions decrease the slope of the dispersing bands and lead to a kink around the Fermi level. The contribution to the linewidth due to scattering at impurities is independent of energy E and temperature T. It is a constant contribution ($\Gamma_{e-imp} = const.$) and changes only with impurity concentration.

3.2 Angular resolved photoemission

With an angular resolved photoemission experiment it is possible to determine the angular dependence of photoemitted valence band electrons as a function of their binding energy. Therefore, not only the kinetic energy E_{kin}, but also the emission angle θ of the photoelectron is measured. When the photoexcited electron passes through the surface into vacuum a free-electron like final state with $E_{kin} = p^2/2m$ is assumed. While escaping, the electron momentum perpendicular to the surface is changed but the in-plane component $k_{||}$ is conserved. According to Fig. 3.4 $k_{||}$ can be determined directly from the emission angle θ of the photoelectron via

$$k_{||}\ [\text{Å}^{-1}] = \sqrt{\frac{2m_e E_{kin}}{\hbar^2}} \sin(\theta) = 0.512\,\sqrt{E_{kin}\ [\text{eV}]}\,\sin(\theta)$$

where m_e is the electron mass and θ the angle between $k_{||}$ and normal emission. The binding energy of the electron in the initial state is determined as before using Eq. 3.1.

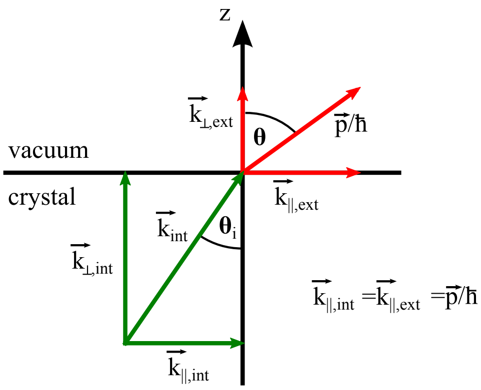

Figure 3.4: Relations between the crystal momentum and the measured electron momentum in the free-electron final state approximation.

The setup for an angular resolved photoemission spectroscopy (ARPES) experiment consists of a photon source in the UV range and an electrostatic analyzer that measures E_{kin} and θ. The photon source can either be a gas discharge lamp, a laser or synchrotron radiation. The typical beam spot size of a UV source is $1\,\mathrm{mm}^2$, whereas at the synchrotron the illuminated area can be much smaller and the intensity much higher. Concerning the analyzer, the availability of 2D charge-coupled device (CCD) detectors has made ARPES an extremely detailed and precise tool to directly measure the electronic band structure ($E_B(k_{||})$) of a 2DES. A typical setup is shown in Fig. 3.5. The in-plane momentum can be varied by turning the sample around θ and Φ, respectively, as indicated.

For the analysis of photoemission data the 2D spectra are usually divided into either momentum distribution curves (MDCs) or energy distribution curves (EDCs). While MDCs show the photocurrent as a function of the emission angle at a constant binding energy, EDCs display the measured intensity at a constant emission angle dependent on the binding energy. For quantitative conclusions an appropriate background has to be subtracted from the spectra. Therefore, the spectrum is divided into a primary spectrum and a secondary spectrum where the latter represents inelastic events like electron-electron and electron-ion scattering [107]. There are several sophisticated formulas for backgrounds, like for example the version given by Tougaard [112], but usually it is sufficient to apply a constant background that accounts for the dark count rate in the detector plus the so-called Shirley background $B_S(E)$. This type of background is proportional to the weight

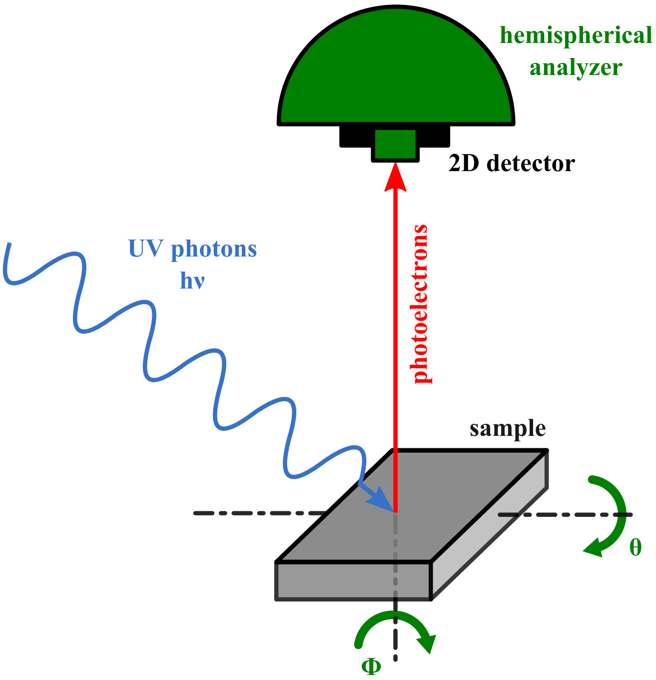

Figure 3.5: Typical angular resolved photoemission setup: Photons with the energy $h\nu$ impinge on the sample surface and excite electrons. The emitted photoelectrons are focused into a hemispherical analyzer. The kinetic energy as well as the emission angle will be measured. The emission angle is varied by turning the sample around θ and Φ and the third direction is covered by the acceptance angle of the analyzer. After passing the analyzer the electrons are detected with a 2D CCD camera.

of the primary spectrum [107]. When analyzing EDCs one has to consider also the cut-off at the Fermi level due to the change in occupation of the electronic states. For the fitting procedure of the remaining primary spectrum peaks with a Voigt line shape, a convolution of Lorentzian and Gaussian functions, are used. The complete fitting function for an EDC is given by:

$$I(E) = c + B_S(E) + \left[\sum_i L(E, E_i, \Gamma_i) * G(\Gamma_{res}) \right] f(E - E_F, T)$$

The constant offset c accounts for the dark count rate in the detector. $L(E, E_i, \Gamma_i)$ are the Lorentzians [see Eq. 3.3] with the peak positions at E_i and the full width at half maximum $\Gamma_i = 2Im(\Sigma)$ that describe the single peaks. The Gaussian function $G(\Gamma_{res})$ accounts for the experimental resolution Γ_{res}.

The measurements presented in Chap. 4 and 5 have been carried out at the Max Planck Institute for Solid State Research (MPI-FKF) in Stuttgart. A hemispherical SPECS electron analyzer (energy and angular resolution are 15 meV and 0.5°, respectively) and a monochromatized He lamp that offers UV radiation at $h\nu = 21.2\,\text{eV}$ (He I) and $h\nu = 40.8\,\text{eV}$ (He II) are attached to the UHV chamber with a base pressure $p = 2 \cdot 10^{-10}\,\text{mbar}$. The manipulator can be cooled with liquid nitrogen to about $-180\,^\circ\text{C}$.

The ARPES experiments shown in Chap. 6 have been performed at the University of British Columbia in Vancouver. The UHV chamber is equipped with a SPECS Phoibos 150 hemispherical analyzer and a UVS300 monochromatized gas discharge lamp. Energy and angular resolution were set to 15 meV and 0.3°. Linearly polarized photons with an energy of 40.8 eV were used. During ARPES measurements the samples were kept at 8 K at a pressure less than $7 \cdot 10^{-11}$ mbar.

The data shown in Chap. 7 were taken at the Synchrotron Radiation Center (SRC) in Stoughton, Wisconsin, USA at the variable polarization VLS-PGM beamline. This beamline was equipped with an elliptically polarized Apple II undulator that delivers p- and s-polarization of photons in an energy range from 15 eV to 250 eV. A Scienta analyzer with an energy resolution of about 10 meV and an angular resolution of 0.4° has been used. The manipulator could be cooled with liquid helium down to 30 K. The base pressure of the UHV chamber was $p = 1 \cdot 10^{-10}$ mbar.

3.3 Core level spectroscopy

Core level spectroscopy, also known as X-ray photoemission spectroscopy (XPS) is a powerful tool to study the chemical composition or to determine the binding energies of the atomic core levels of elements in a solid [113]. A photon source that delivers photons in the soft X-ray region is needed to provide enough energy for excitation of core electrons. The binding energy of the core levels is determined by measuring E_{kin} of the photoelectrons for normal emission and using Eq. 3.1. A schematic illustration of the photoemission process in XPS is drawn in Fig. 3.1.

Since every element has a characteristic series of binding energies for its core electrons XPS serves to determine the chemical composition of the sample surface by comparing the measured peak positions to reference spectra. For precise identification one can additionally check the intensity ratio and separation of some spin doublets for p, d and f lines. Due to SOC all core levels with non-zero angular momentum ($l \neq 0$) are split into branches. Furthermore the holes created in the atoms give rise to the emission of so-called Auger electrons, which can be detected in the spectrum too.

When elements are mixed in compounds, the binding energy of the peak under investigation shifts slightly by an amount ΔE_B, which is called the chemical shift. Whether this shift is positive or negative is determined by the effective electronic potential variation induced by the charge distribution between the elements forming the compound. Furthermore, the shift depends on the bonding type, on the electronegativity of the elements, and on the interaction between the photoionized atom and the rest of the crystal [107]. By measuring the small shifts one can use XPS to determine the chemical state of an atom. This is the reason why formerly XPS was also called ESCA which stands for electron spectroscopy for chemical analysis.

It is also possible to analyze XPS spectra quantitatively. The integrated intensity of the peaks give access to the concentration of a particular material. One has to take care about the secondary electrons. The main peaks in the photoemission spectrum correspond to electrons that leave the surface without energy loss. Electrons that undergo inelastic scattering events contribute to the Shirley background.

All core level spectra shown in this thesis were measured at the MPI-FKF in Stuttgart. The measurements have been performed at room temperature using non-monochromatized Mg K_α radiation at $h\nu = 1253.6\,\mathrm{eV}$. The spot size of a conventional X-ray source is about a few mm^2. XPS has been used mainly to check the cleanliness of the substrate.

Chapter 4

Coulomb interaction in topological insulators

A 3D TI is a quantum state of matter characterized by an insulating bulk state and gapless surface states that show a peculiar spin texture [see Sec. 2.2.2]. Possible applications of TIs in electronic devices require a highly insulating bulk and tunable Dirac carriers. Due to the coexistence of both bulk and surface conduction in Bi_2Se_3, it is difficult to investigate the topological properties separately. In ongoing research, there are extensive efforts to reduce bulk carriers in Bi_2Se_3 through material doping [41, 51, 114], nanostructuring [57, 115, 116] and electric gating [117, 118]. By replacing Se with Te atoms, the bulk insulating property could be considerably improved. Accordingly, Bi_2Te_2Se is a system where the energy gap is $\Delta \approx 0.3\,\mathrm{eV}$ and the chemical potential is located within the bulk band gap [119].

Common theoretical descriptions of TIs are formulated in terms of single-particle quantum mechanics. Due to quite large lattice dielectric constants (> 50) in TIs and the very small corresponding effective fine structure constant, it is often claimed that electron-electron interactions are negligible and does not alter the topological properties [59]. But it was shown that the electron-electron interaction is often needed to describe experimental observations [120–122]. If the interaction is very strong it can even turn the topological phase into an insulating ground state [6] or induce a novel critical state on the surface [123]. Therefore, it is a crucial issue to understand the interplay between strong electron-electron interaction and the topological surface states [124, 125].

4.1 Bi_2Se_3, Bi_2Te_3 and Bi_2Te_2Se

The 3D TIs Bi_2Se_3 and Bi_2Te_3 and also the mixture Bi_2Te_2Se have a tetradymite structure. All materials of this family crystallize in covalently bonded QLs weakly interacting via van der Waals force [5]. As shown in Fig. 4.1(a) the stacking order is A-B-C-A-B-C. Each quintuple layer is about 1 nm thick and the lattice constant along the *c*-axis is about 3 nm.

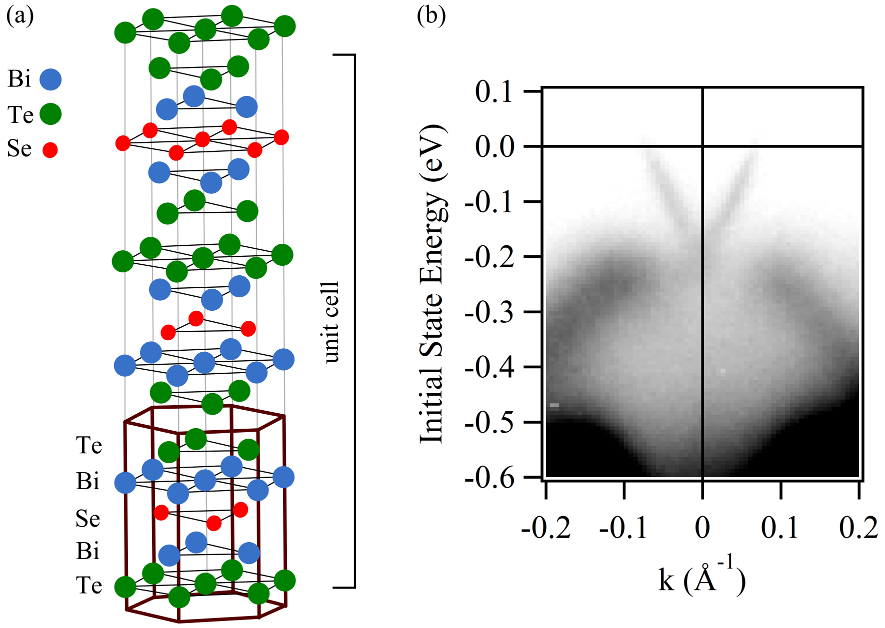

Figure 4.1: Crystal structure of tetradymite chalcogenides, using the example of Bi_2Te_2Se and the corresponding surface band structure. (a) QL enclosed by the brown cage is the building block of this type of materials. The stacking order of the QLs is A-B-C-A-B-C, and hence the unit cell consists of a stack of 3 QLs. (b) Topological surface state measured with ARPES.

The interesting properties of those materials are connected to their electronic structure and, particularly, the low energy region. The states close to the Fermi energy are mainly p orbitals. Therefore, the opposite parities originate from bonding and anti-bonding states. By taking into account chemical bonding, crystal field splitting and SOC, a pair of inverted energy bands is found at the Fermi level. This inversion drives the system into a TI phase. The bulk insulating gap is $\Delta \approx 0.3\,\text{eV}$, which results in the possibility of having a topological phase at room temperature. To describe the low-energy properties of those systems an effective Dirac model is used.

Due to naturally occurring crystalline defects in Bi_2Se_3 and Bi_2Te_3, their bulk is always highly doped and their transport properties are always dominated by bulk carriers. The key for the preparation of a TI with large bulk resistivity is to shift the Fermi level into the bulk band gap. For example, by mixing Te and Se atoms, Bi_2Te_2Se can be fabricated, in which the chemical potential is located between valence and conduction band of the bulk and which shows a large bulk resistivity exceeding $1\,\Omega$cm [119]. By this shift of the chemical potential the contribution from the surface states to the conducting electrons is strongly enhanced. It is the first 3D TI where detailed transport studies of the topological surface state are possible. Clear Shubnikov-de Haas oscillations are observed and they contribute $\sim$ 6% to the total conductance in a 260-μm-thick bulk crystal. Xiong and coworkers reported an even larger resistivity of $6\,\Omega$cm [126].

For the investigation of the surface state band structure including many-body effects in 3D TIs ARPES is the technique of choice. ARPES probes directly the 2D band structure which contains all the many-body phenomena [see Chap. 3.1.2]. Bi_2Te_2Se crystals were grown in the group of Prof. Claudia Felser at the MPI-CPfS in Dresden. The samples were glued to a sample holder and cleaved in vacuum via mechanical exfoliation. As a photon source, the HeI line was used. In Fig. 4.1(b) the band structure of a freshly cleaved surface is presented. This measurement and all subsequent ones on this system were performed at room temperature. The topological surface state in the bulk band gap is clearly visible. The Dirac point almost coincides with the top of the valence band at around $E_B = 0.2\,\text{eV}$. From the Fermi level down to this point we only see the Dirac cone and a very low background. There are only the topological states at the Fermi level and for them back scattering is forbidden. Hence, the bands are quite sharp and they are almost linear dispersing. We note that there is no sign of the conduction band visible at the Fermi level and that the resulting bulk band gap is quite big. All our experimental findings coincide with previous ARPES measurements [55].

4.2 Doping behavior

If the freshly cleaved sample is left in the UHV chamber for some time, a shift of the Dirac point to higher binding energies can be observed. This time-dependent doping effect can be explained by contamination of the surface from residual gas in UHV. The adsorbates give rise to a strong band bending of the bands near the surface. A similar effect was also observed for Bi_2Se_3 [127, 128]. In Fig. 4.2 the band structure measured at different delay times with respect to the cleavage procedure is shown.

The small black arrows indicate the position of the Dirac point, which shifts to higher

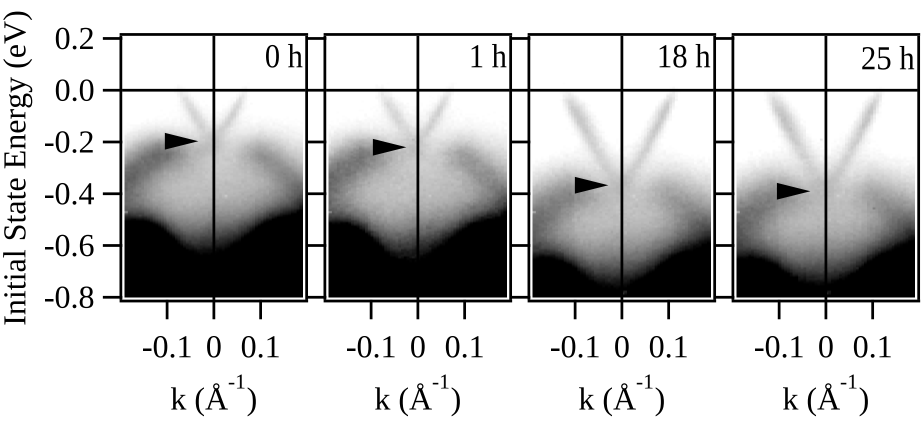

Figure 4.2: Time-dependent doping of the topological surface state at $\overline{\Gamma}$ in Bi_2Te_2Se while resting in vacuum. Dirac point shifts to higher binding energy over time as indicated by the black arrows. The duration between cleave and measurement is indicated in the upper right corner of the panels.

binding energy over time. After 25 hours the total shift of the Dirac point amounts 170 meV. Despite the large shift, we still do not see any indication from the conduction band at the Fermi level. Hence, we conclude that the gap is at least $\Delta = 0.37\,\text{eV}$. Due to the band bending, the charge carrier density n increases. We determined the Fermi wave vector k_F and extracted n. Both are graphically shown in Fig. 4.3.

Both k_F and the corresponding n increase over time. Since we have only four data points we can just surmise that in the beginning the band bending goes almost linearly whereas it starts to saturate after 18 hours. During roughly one day in UHV the charge carrier density increases by the factor of 2.8 due to adsorption of residual gas molecules. This gives us the opportunity to study the effect of different charge carrier densities on the strength of many-body interactions in TIs.

4.3 Coulomb interaction at low charge carrier densities

The images in Fig. 4.2 show clearly the shift of the surface states to higher binding energies (as indicated by the small arrows) and the increase of the Fermi wave vector k_F over time. To evaluate the many-body physics in the system we had a closer look at the linewidth, since it is proportional to the imaginary part of the self-energy. In the following analysis we stick to the extreme cases - the freshly cleaved, clean sample and the one that remained for 25 hours in vacuum (now called the 'aged sample'). We took the single MDCs and

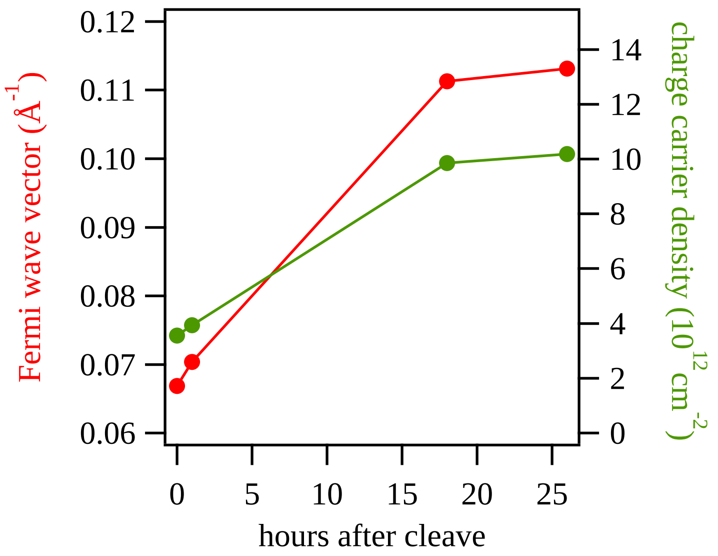

Figure 4.3: Time-dependent increase of the Fermi wave vector k_F as well as the charge carrier density n in Bi_2Te_2Se.

fitted them as exemplarily shown in Fig. 4.4(a). Presumably, an imperfect alignment of the sample leads to a difference in linewidth of the left and the right branch and we determined them separately. The extracted linewidth from every single peak of the left branch as a function of binding energy for the clean and the aged sample is plotted in Fig. 4.4(b).

For both the clean and the aged sample the linewidth has a minimal value at the Fermi level and increases with increasing binding energy. We also notice that the absolute value of the linewidth at the Fermi level is larger for the aged sample. This can be explained by the adsorbed gas molecules, which induce disorder at the surface leading to a constant offset in the linewidth. In fact, the linewidth for the aged sample is larger at the Fermi level, but the increase of the linewidth is smaller.

As introduced in Sec. 3.1.2 there are two energy dependent scattering mechanisms that can contribute to broadening of the linewidth; electron-electron and electron-phonon interaction. The Debye temperature T_D in Bi_2Te_2Se is assumed to be comparable to the one in Bi_2Se_3, which is $T_D = 182\,\mathrm{K}$ ($\sim 16\,\mathrm{meV}$) [129]. Since our measurements were performed at room temperature the thermal energy is above T_D and we do not expect an energy dependent contribution due to interaction with phonons. Therefore, we instead attribute the energy dependent increase of the linewidth to electron-electron interactions. The difference in the increase of the linewidth can be explained by varying screening

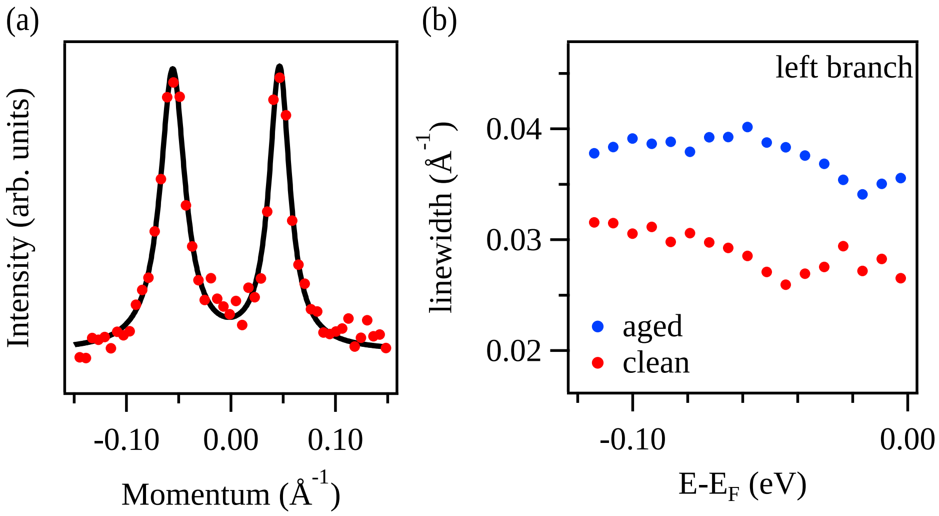

Figure 4.4: (a) Exemplary fit of two Lorentzian to a MDC cut through the topological surface state. (b) Increase of the linewidth as a function of energy for two different doping levels.

strength due to the difference in the total number of charge carriers. The only difference between the two samples is the charge carrier concentration at the Fermi level. Due to doping, i.e. the shift to higher binding energies, and the linear dispersion the Fermi surface volume increases over time, which results in a higher charge carrier density at zero binding energy. The more electrons are available, the higher the screening of the interaction. If the interaction is efficiently screened the linewidth broadening due to electron-electron interactions is reduced.

In addition to the change in linewidth, we observe a change of the Fermi velocity, i.e. the slope of the bands at the Fermi level, over time [see Fig. 4.5]. We noticed that the band velocity at the Fermi level is bigger for the aged sample. This can be explained by a renormalization of the Fermi velocity due to the electron-electron interaction, which results in a band that disperses less steep compared to the non-interacting case. Since the number of charge carriers increases by going from the clean to the aged sample, the efficiency of the screening rises and hence, the band velocity increases over time.

For more quantitative statements about linewidth and band velocity, we compare the results of the MDC fits to a theoretical model. With data sets at different doping levels and by considering self-consistency we are able to determine the parameters for the complex self-energy and the bare band dispersion. We performed model calculations in 2D for the

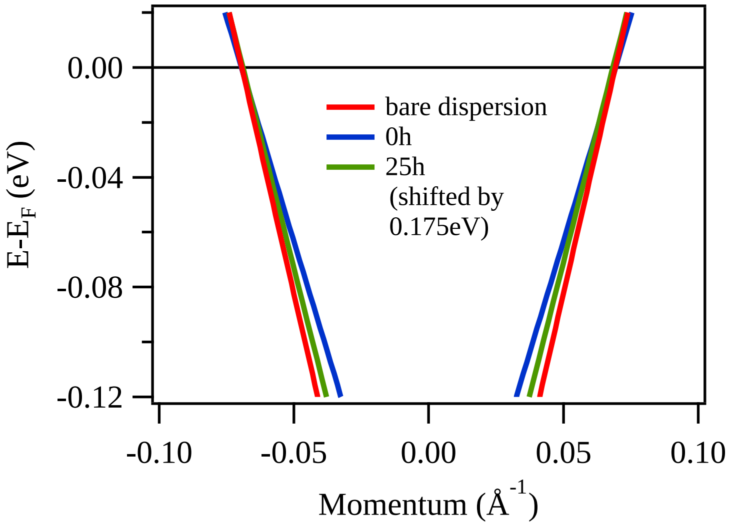

Figure 4.5: Comparison of the band dispersion close to the Fermi energy. To be able to compare the slopes, the band structure of the aged sample was shifted by 0.175 eV to smaller binding energies. For the freshly cleaved sample we observe the smallest slope, since screening is not sufficient due to the small number of charge carriers.

spectral function [see Eq. 3.3] by assuming a bare band dispersion of the form

$$E^0_{\vec{k}} = v_F|\vec{k}| + \epsilon_0 \tag{4.1}$$

Since we attribute the increase of the linewidth and the Fermi velocity to electron-electron interactions we assume a quadratic energy dependence ($\mathrm{Im}\Sigma(\omega) \propto \omega^2$, see Eq. 3.4) for the imaginary part of the self-energy [130]. The imaginary and the real part of the complex self-energy are connected via a Hilbert transformation $\mathcal{H}$: $\mathrm{Re}\Sigma = \mathcal{H}(\mathrm{Im}\Sigma)$. Therefore, we choose for the self-energy the following ansatz:

$$\Sigma(\omega) = i(\beta_1\omega^2 + \alpha) - \beta_2\omega \tag{4.2}$$

The parameter α serves as a constant offset in the linewidth, while β_1 forms the real part and β_2 is the coupling constant for electron-electron interaction. For reasons of self-consistency, the ratio between the coefficients will be held constant $\beta_1/\beta_2 = const.$ for all doping levels. In our case the ratio was found to be $\beta_1/\beta_2 = 2$. We note that the band velocity of the bare dispersion is also fixed for all doping levels. We calculated the spectral function [Eq. 3.3] using the bare dispersion in Eq. 4.1 and the self-energy from Eq. 4.2. After a convolution of the band structure with a Gaussian to account for the experimental momentum and energy resolution the calculated MCDs were fitted with two peaks of Lorentzian shape. We compared the calculated values for peak position and linewidth to the experimental ones by applying a χ^2-test. The smallest value for χ^2 tells us the best fitting values for the three parameters. With this procedure we are able to handle both data sets at different doping levels at the same time. We found a set of parameters that matches the position and hence the slope of the bands as well as the linewidth of the peaks for the clean as well as for the aged sample. The fit results for the experimental and the theoretical peak positions are presented in Fig. 4.6(a). The calculated linewidths are shown together with the experimental ones in Fig. 4.6(b). For the model calculations we also treated the two branches separately. All important fit parameters are collected in Table 4.1.

	ϵ_0 (eV)	v_F (eVÅ)	β_1 (1/eV)	β_2	n (10^{12} cm^{-2})
clean (0h)	-0.3	4.5	0.62	0.31	3.5
aged (25h)	-0.51	4.5	0.18	0.09	10.2

Table 4.1: Results of the χ^2-test for the parameters of the bare band dispersion [Eq. 4.1] and the complex self-energy Σ [Eq. 4.2]: energy offset of the Dirac point ϵ_0, Fermi velocity in the bare band dispersion v_F, electron-electron interaction constant β_1, the parameter for the real part of Σ β_2; for comparison: charge carrier density n.

In addition, our model combined with data sets at different doping levels and the χ^2-test allows us to extract the band velocity of the bare dispersion. With ARPES we measure the real band structure, which is the result of the combination of the non-interacting system plus interactions. Solely because we have two data sets which we can compare and handle self-consistently we are able to determine the band dispersion without interaction. We found a bare band velocity of 4.5 eVÅ. In order to compare it to the renormalized bands we plotted it in Fig. 4.5.

4.4 Discussion

Looking at the fit results we see, that the first value, which we determined, is the energy shift of the band structure ϵ_0. As we see in Fig. 4.2 the cone shifts to higher binding energy over time and we expect a larger shift for the aged sample. Indeed we find a ϵ_0 whose absolute value is larger for the aged sample. The difference between clean and aged sample is 210 meV which is in the order of the experimental observed shift of 170 meV. The deviation of 40 meV can be explained by the band renormalization. For the coupling

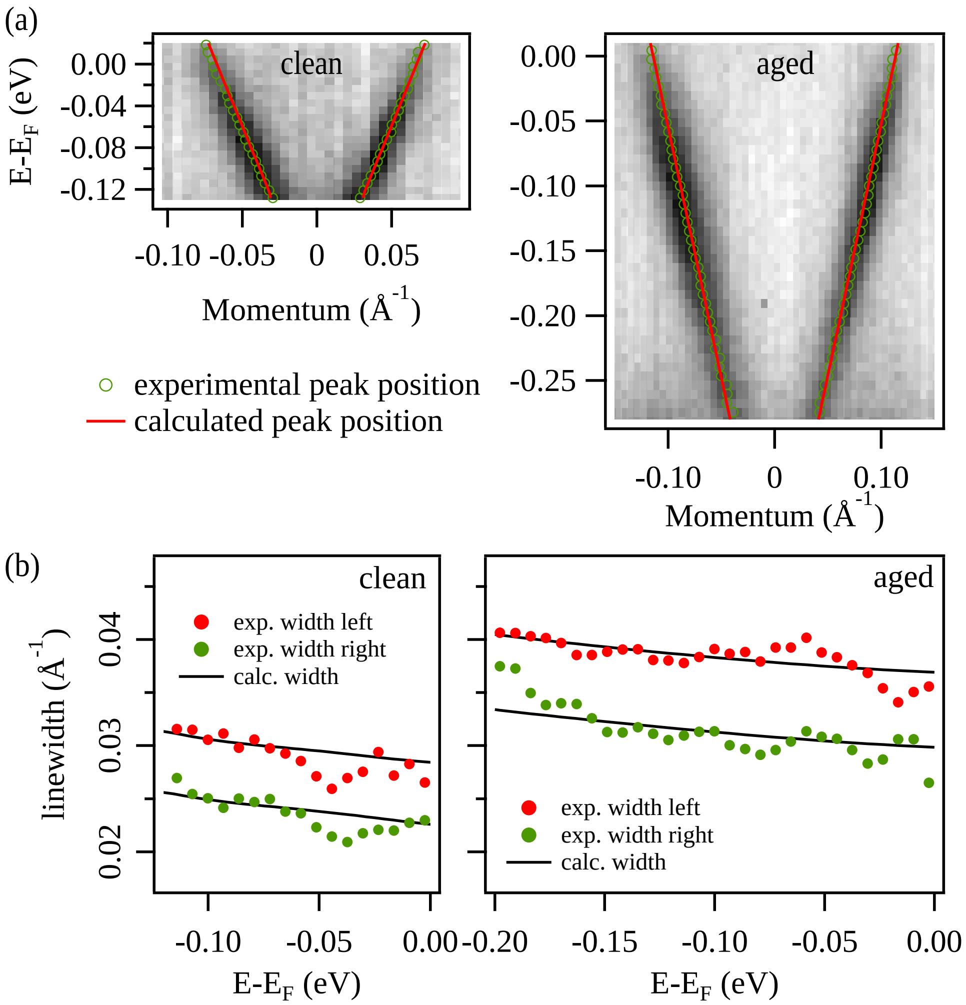

Figure 4.6: Comparison of experimental and calculated peak positions as well as linewidths for the topological surface state in Bi_2Te_2Se. The experimental values were found by fitting two Lorentzians to every MDC. The theoretical values were determined by calculating the spectral function with the complex self-energy from Eq. 4.2 and performing the same fit procedure as for the data. Note that left and right bands are treated separately.

constant β_1 — and since the ratio is constant also for β_2 — we find that it is a factor of 3 larger for the clean sample. By keeping the sample one day in vacuum the electron-electron interaction diminishes to 30% of the starting value. This tells us that the interaction in the freshly cleaved sample is much higher than in the aged one. If we compare the charge carrier densities of the two samples which can be found in the last column of Table 4.1 we also find roughly a ratio of 3 for clean and aged sample. This fact supports our assumption that the electron-electron interaction increases if n is getting smaller and leads us to the conclusion that β_1 is inverse proportional to n. Beside n, the dielectric constant ϵ determines the strength of the screening. Since we measured all data on the same sample we assume the same ϵ.

A much smaller value for ϵ applies for graphene. This is the reason, why the quasiparticle dynamics was studied intensively for graphene. The dielectric constant in graphene is about 10 times smaller than of TIs. For small values of ϵ, screening is not sufficient and the Coulomb interaction is stronger. The effect of the charge carrier density on the other hand is negligible in graphene. The charge carrier densities which we observe usually in our graphene samples [see Chap. 6] are comparable to the ones in the aged Bi_2Te_2Se sample. There should be enough charge carriers available to screen the electron-electron interaction. Nevertheless, the small ϵ in graphene leads to a substantial renormalization of the band structure.

For a more quantitative conclusion in the case of Bi_2Te_2Se it would be desirable to find a way to connect the parameters β_1 and β_2 or their ratio to the strength of the screening. We would expect that the parameter β_1 shows the following dependency: $\beta_1 \sim 1/(\epsilon n)$. Therefore, more detailed measurements and theoretical considerations are necessary.

Our analysis procedure in this chapter can be transferred to many other studies of many-body physics with ARPES. We have shown how to handle electron-electron interaction but one could think of applying our analysis procedure also on electron-phonon interaction. The ingredients for a detailed analysis are a formula for the self-energy and a proper ansatz for the bare band dispersion. As long as only one data set is available the model is able to find the parameters for Σ. Self-consistency helps to determine both the real part as well as the imaginary part [131]. But for an advantageous situation like ours when there are measurements done at different n the model allows even for a determination of the bare band dispersion. In a more general sense we have used the measured and the calculated spectral function to find the complex self-energy in Bi_2Te_2Se.

In summary, electron-electron interactions are usually neglected in TIs since the dielectric constant ϵ is quite large. However, we observe a substantial band renormalization of the surface states in Bi_2Te_2Se dependent on the charge carrier density and on the binding energy. Due to time dependent doping caused by the adsorbed molecules from the residual gas in UHV we are able to investigate the band renormalization for different doping levels. Combining the data sets allows us to determine the parameters for the complex self-energy self-consistently and to extract the contribution from electron-electron interactions to the linewidth broadening. Additionally, we found also a value for the band velocity without interactions. We confirm that electron-electron interactions or more general, many-body physics is necessary to describe all the properties of topological surface states.

Chapter 5

Surface band structure of $TiTe_{1.5}Se_{0.5}$

In addition to the careful investigation of the already known TIs, it is also very important to look for new materials with topological states and peculiar properties. The first experimentally confirmed TIs — HgTe [42] thin films and $Bi_{1-x}Sb_x$ [38]— are quite difficult to fabricate and show a complex surface band structure, respectively. However, with the discovery of bismuth compounds with topological properties, it was shown that topological surface states can also be found on inexpensive and readily available materials. This opened the door for a very intensive research field in which scientists are looking for new topological materials [132].

5.1 Search for new topological materials

The motivation for finding new topological materials is twofold; on one side it is interesting for fundamental research and on the other side it is very important for the development of electronic devices containing TIs. In the first case, the driving force is to discover and study new physical phenomena. One goal is to achieve a better understanding about what turns a material into a TI. For applications of TIs, scientists are also interested in finding new topological materials that have some practical advantages compared to the known ones. They are looking for TIs that are, for example, easier to fabricate, which have higher bulk resistivity or TIs in which the charge carrier density can be easily tuned. Several families of 2D and 3D TIs have been proposed theoretically and have been, in part, confirmed experimentally [see Sec. 2.2.2].

For a systematic approach for finding new ones, we have to combine all the experimental results with the established theoretical knowledge and attempt to make strong predictions.

In particular, it is important to consider the band structure considering its crucial role. For example, *ab initio* calculations can help to establish a topological phase diagram and to search for non-trivial surface states [133]. For example, in $TiS_{2-2x}Te_{2x}$ a topological non-trivial phase was predicted for $0.48 < x < 0.80$ in 2D as well as in 3D.

Since SOC is often responsible for the required band inversion of the topological state a promising approach is to look for systems with narrow band gaps and heavy atoms. Many new topological materials consist of elements from the lower right corner of the periodic table. Examples are Bi [39], Pb [134] and Tl [49] based chalcogenides. In addition, mixing of element compositions has proven successful. With these points in mind, titanium dichalcogenides are also promising candidates.

5.2 Crystal structure

In general, transition metal dichalcogenides (TMDCs) have been attracting attention for more than 40 years due to their diverse properties [135, 136]. For example, electrically they cover the whole spectrum from insulators (HfS_2) through semiconductors like MoS_2, to semimetals (WTe_2) and true metals like NbS_2. The properties of some of the TMDCs can be tune via a structural distortion. Even superconductivity, charge density waves and antiferromagnetism were observed in TMDCs [135, 137].

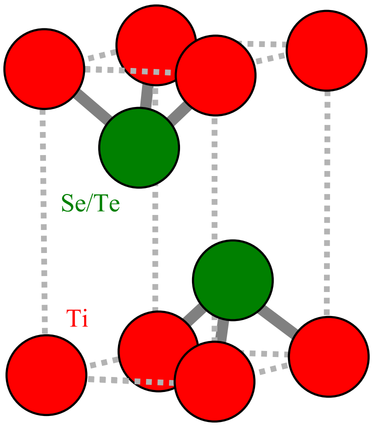

Figure 5.1: Crystal structure of TiX_2. Every chalcogenide (green) atom is bound to three titanium (red) atoms. The van der Waals gap lies inbetween the chalcogenide layers. The depicted cube illustrates the unit cell of the structure.

Like all TMDCs, the ones with Ti consist of X-Ti-X (X= S, Se, Te) composite layers. They are stacked like the layers in graphite and bound by weak van der Waals interactions acting perpendicular to the sheets. Those compounds crystallize in the $1T$-CdI_2 prototype structure [138]. Such layered structures show typical quasi-2D behavior. The unit cell is depicted in Fig. 5.1. If the chalcogenides are exchanged or mixed, no structural phase transition is expected as the lattice parameters are adapted. The lattice constants for $TiSe_2$ are $a = 3.540$ Å and $c = 6.008$ Å, for $TiTe_2$ they are $a = 3.777$ Å and $c = 6.498$ Å and for the mixture TiTeSe $a = 3.651$ Å and $c = 6.317$ Å were found [138].

$TiSe_2$ was intensively studied because of the occurring charge density wave at low temperatures. On the other hand, those materials are known for their intercalated derivatives like in the case of TiS_2. Foreign atoms can easily be introduced into TMDCs at the van der Waals gap and can modify the properties of the compound radically. Those intercalated compounds have been employed as a cathode material in rechargeable batteries, but they can also be used as strongly anisotropic conductors and ordered magnetic systems [139].

5.3 Electronic structure

The electronic band structure of monolayer TiS_2 and $TiTe_2$ in the presence of SOC was calculated in [133] and is shown in Fig. 5.2. The authors predict a topological nontrivial state for $TiS_{2-2x}Te_{2x}$ from $0.48 < x < 0.80$.

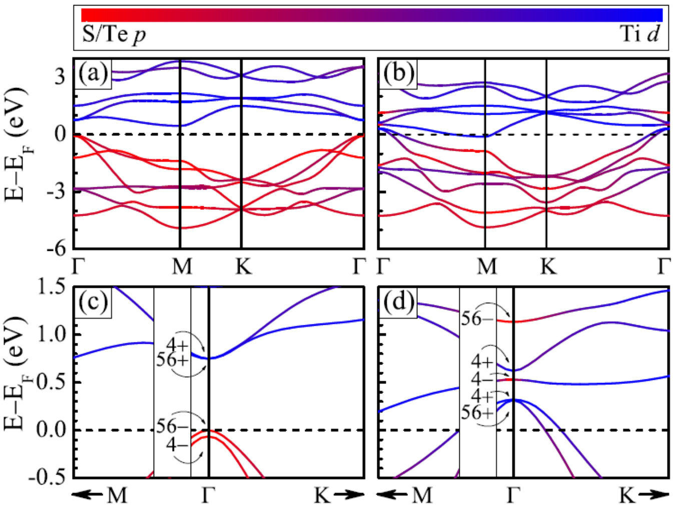

Figure 5.2: Electronic band structures of monolayer (a) TiS_2 and (b) $TiTe_2$, in the presence of SOC. The different colors indicate the band characters as the bar on top shows. (c) and (d) show a zoom-in at the $\overline{\Gamma}$-point and the band hierarchy. Symmetry is labeled, and even/odd parity is indicated by +/- (taken from [133])

In this case we can exemplarily follow the band inversion by going from TiS_2 to $TiTe_2$. For both materials, the bands with S/Te p character are filled whereas the Ti d bands are almost empty. In the lower panels of Fig. 5.2 the parity of the states is indicated. In TiS_2 the odd parity states are separated from the even parity states by E_F and the material turns out to be an indirect band gap semiconductor. The valence band maximum is located at the $\overline{\Gamma}$-point and the conduction band minimum at the $\overline{\text{M}}$-point for both materials. However, in the case of $TiTe_2$ the states are entangled and the energy band gap is lost. At the $\overline{\Gamma}$-point the bands are inverted but the material is still topologically trivial. However, by mixing S and Te the material can be turned into a TI.

Since all the chalcogen atoms are isoelectronic, Se has the same number of electrons in the outer shell but one shell more than S and one shell less compared to Te. By replacing S with Se, SOC is slightly increased. Accordingly, the surface band structure of the mixture, $TiTe_{2x}Se_{2-2x}$, should be comparable to the one of $TiTe_2$. To check if these assumptions are true we performed ARPES measurements of $TiTe_{1.5}Se_{0.5}$ crystals where $x = 0.75$.

The crystals were grown in the group of Prof. Lotsch at the MPI-FKF in Stuttgart. After inserting them into the UHV chamber they were mechanically cleaved *in situ*. Before the ARPES measurements we checked the properties of the surface. The XPS overview spectrum in Fig. 5.3 shows several peaks that we identified through comparison to literature [113].

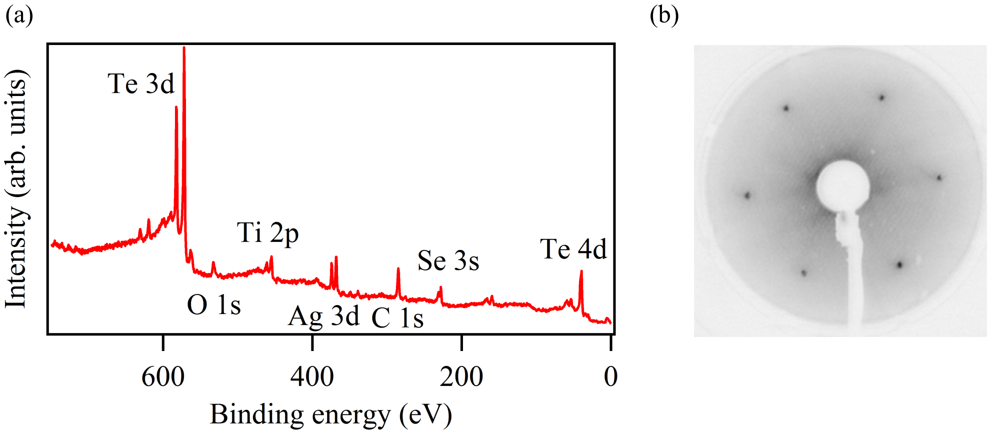

Figure 5.3: Surface analysis of $TiTe_{1.5}Se_{0.5}$: (a) XPS and (b) LEED at E=51 eV.

In addition to all expected elements (Ti, Te, Se) we found peaks for Ag, O and C. The small Ag peaks originate from the glue used to fix the sample on the sample holder. Since the crystals are very small it was impossible to eliminate the Ag peaks. Appearance of oxygen and carbon can be explained by the growing process and transportation through air before inserting into UHV. However, the intensity of the C and O peaks is quite small and thus they can be neglected. Overall, XPS confirms that the crystal surface is clean enough for ARPES measurements. To check the structural properties of the surface we did also LEED measurements at 51 eV and observed a clear hexagonal structure [inset in Fig. 5.3].

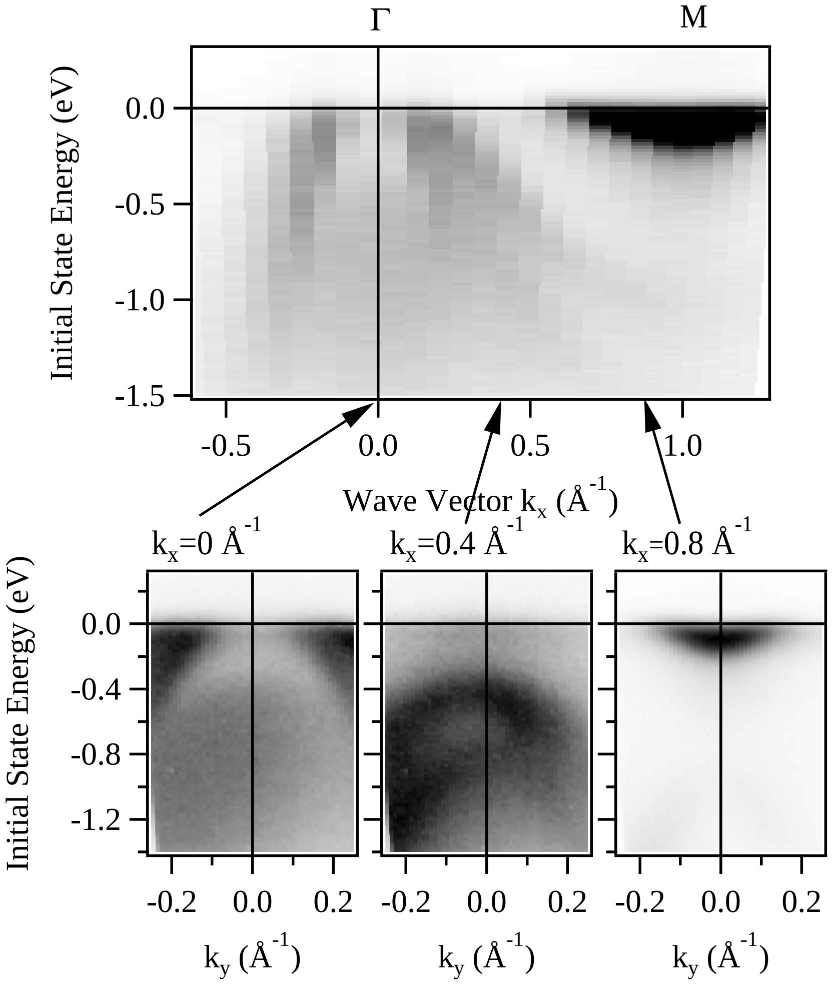

Figure 5.4: Surface band structure of $TiTe_{1.5}Se_{0.5}$ in $\overline{\Gamma M}$ direction. In the lower panels cuts perpendicular to $\overline{\Gamma M}$ at indicated positions are shown.

In Fig. 5.4 the measured surface band structure of $TiTe_{1.5}Se_{0.5}$ at room temperature is shown. We compare our experimental results to the calculated band structure of $TiTe_2$ and observe many similar structures. There are two bands above the Fermi level that build a hole pocket at the $\overline{\Gamma}$-point [see lower left panel of Fig. 5.4]. In $\overline{\Gamma M}$-direction they disperse downwards and cut the Fermi level at about $k_x = 0.12$Å $^{-1}$. At $k_x = 0.4$Å $^{-1}$ we can clearly distinguish two bands in the panel in the middle. The second clear feature is a small electron pocket at the $\overline{\mathrm{M}}$-point with the band minimum at $E = 0.3\,\mathrm{eV}$. In the lower right panel of Fig. 5.4 the electron pocket at $k = 0.8\,\text{Å}^{-1}$ perpendicular to the $\overline{\Gamma\mathrm{M}}$-direction is shown.

To judge whether $TiTe_{1.5}Se_{0.5}$ is a topological nontrivial material we would need to see the inverted band gap and to measure a topological surface state. However, it was so far impossible to observe the band gap because it lies in the unoccupied states at the $\overline{\Gamma}$-point as can be assumed by looking at Fig. 5.2(d). With ARPES we are able to study only the occupied states. For the observation of a possible topologically protected surface state sufficient electron doping would be needed to shift the band gap below the Fermi level.

5.4 Discussion

Our experiments are just the first step of identifying $TiTe_{1.5}Se_{0.5}$ as a TI. So far, it appears to be a promising candidate and further investigations are desirable. There are also many other proposals for TMDCs as 2D quantum spin Hall insulators. Especially for MX_2 with M=(Mo, W) and X = (S, Se, Te) a lot of theoretical studies are done and unique properties are predicted [140, 141]. Those 2D materials are fascinating because of their similarity to graphene and the possibility to build 2D heterostructures by stacking different 2D sheets on top of each another [142]. So far, those van der Waals-heterostructures have not been considered for topological phases of matter [132, 143]. Therefore, we see a new research field developing and expanding in the near future.

In addition to their topological properties, TMDC nanostructures have attracted increasing attention because of their versatile chemical properties in contrast to graphene. Monolayers of TMDCs are usually semiconductors with varying band gaps and variable charge carriers (n- or p-type). By changing their composition, their structure or their dimensionality, these materials can be very attractive for a variety of applications [144–146]. For example, many of the TMDCs show layer dependent behavior. For example, several semiconducting TMDCs undergo a transition from an indirect gap in the bulk to a direct bandgap for a monolayer [147]. The direct bandgap in the monolayer is usually larger than in the bulk and opens the possibility of many optoelectronic applications [146].

TMDCs are also very promising candidates for photo-catalytic water splitting. In particular, monolayers of metal disulfides show very good catalytic performance in water splitting [148]. The electrolysis of water driven by catalysts is considered as the 'cleanest' way for hydrogen production. One major goal in the research field of hydrogen production is to find cheap and abundant catalysts that are suitable for large-scale implementation in technology. Other interesting applications are in the field of energy storage as electrodes in Li-ion batteries or as photovoltaics [149].

Due to the lack of an inversion center in the crystal structure of TMDC monolayers a new degree of freedom of the charge carriers is accessible: the valley index. Taking advantage of this fact is the main goal of valleytronics, a new field of physics [150, 151].

Chapter 6

Scattering mechanisms in thallium doped epitaxial graphene

Due to its unique and very interesting properties graphene is a promising candidate for future generations of extraordinarily fast electronic devices. The electron mobility at room temperature, which is higher than in any other known material, results from the fundamental symmetry and the strict two-dimensionality of the graphene honeycomb lattice. If the perfect symmetry is broken by either a defect or an impurity the electrical properties can be changed substantially. In many cases, this can be actually advantageous and some properties can be even improved by the appropriate introduction of impurities. Examples are charge-transfer doping through adatoms or molecules to tune the position of the Dirac point with respect to the Fermi level [152–156], and also different interactions (electron-electron or electron-phonon) [98, 157, 158], metal-insulator transitions [159, 160] and — so far only at the level of theoretical prediction — the emergence of superconductivity [161] or of topologically insulating behavior [162].

On the other hand, defects or impurities in the graphene lattice can also disturb or damage the electronic properties. Every time impurities are introduced they give rise to unavoidable mobility-limiting disorder and enhanced scattering [163]. Efficient doping by molecules even necessitates the presence of defects in the graphene layer [164]. In most cases, adatoms reduce the quasiparticle lifetime by introducing long-range (Coulomb) scattering and/or short-range (δ-potential) scattering. The latter has been proposed to be largely responsible for graphene's residual conductivity [163]. In order to gain more insight into the electronic properties of graphene, it is important to analyze and understand how impurities affect them.[1]

6.1 Impurities on graphene

There are several different ways for an impurity to connect itself to graphene. This ranges from weakly-attached physisorption [165] to the formation of a covalent bond as in the example of hydrogen, which sp^3-hybridizes the carbon bond [159]. The impurity can also donate charge to the graphene layer and act as a charged impurity. In any case, graphene's electronic structure will be affected somehow.

In general, the charge carrier mobility μ is inversely proportional to the density of charged impurities n_{imp}. This translates into an increase of the scattering rate upon doping. There are also other reports that claim an increase of the quasiparticle lifetime upon doping with charged impurities [166]. Such behavior critically depends on screening, which is determined through the dielectric constant ϵ of the system. Depending on ϵ, different scattering mechanisms can become more pronounced or suppressed. Coulomb scattering is often assumed to be the dominant scattering mechanism in graphene, but short-range scattering can become appreciable if dielectric screening is highly effective in reducing Coulomb scattering.

Impurities with states close to the Fermi level also give rise to a particularly strong scattering potential [167]. In this sense, short-range scattering can also be present for non-covalently bonded impurities. Therefore, in real systems, it is not necessarily *a priori* clear which scattering mechanism is dominant. With ARPES measurements it is possible to observe the scattering behavior induced by Tl adatoms on graphene and disentangle long-range from short-range scattering contributions.

Tl atoms on graphene is a particularly interesting model system as it nicely demonstrates the difficulty in predicting the scattering behavior beforehand. We show that it features a sizeable short-range scattering contribution even though its adsorption behavior is similar to potassium; it is extremely weakly bonded to graphene and highly mobile at temperatures above 15K. Only by employing the electronic structure of the unperturbed Tl atom, we are able to theoretically predict the scattering behavior. In addition, Tl has been proposed as one of the most promising candidates to open a SOC related gap at the Dirac point turning graphene into a TI [162].

Epitaxial graphene monolayers with a buffer layer were grown under Ar atmosphere on

---

[1] The present chapter is based on publication 3 from the list attached at the end of this thesis.

hydrogen etched 6H-SiC(0001) at the MPI-FKF in Stuttgart. To remove the adsorbed gas molecules from air, the graphene samples were post-annealed at 700°C after insertion into UHV in the ARPES chamber in Vancouver. It has been calculated that Tl is one of the most mobile atoms on the graphene surface [168]. Therefore, Tl atoms were evaporated from an electron beam evaporator on a cold sample at 8 K to avoid surface diffusion and clustering. All subsequent measurements were done at similar temperatures.

6.2 Doping effect of Tl adatoms

Fig. 6.1 shows the experimentally determined band structure of an epitaxial graphene monolayer near the $\overline{\mathrm{K}}$-point as a function of Tl coverage.

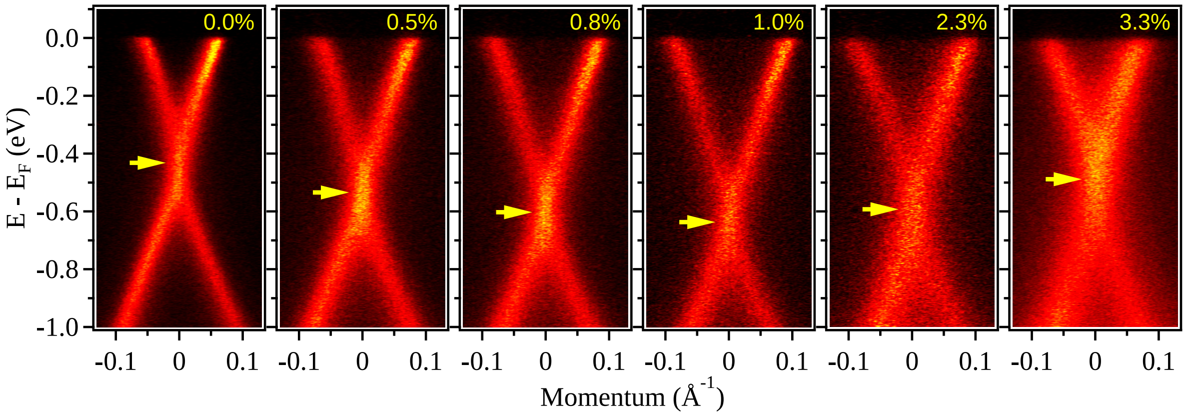

Figure 6.1: Monolayer graphene decorated with small amounts of Tl atoms. Experimental band structure near the $\overline{\mathrm{K}}$-point for increasing Tl concentration x measured at 8 K with a photon energy of 40.8 eV.

The concentration x of Tl atoms on the surface is given in percent of a graphene monolayer, i. e. the number of Tl atoms per carbon atom. The left-hand side data set is from the pristine graphene monolayer, exhibiting an initial n-type doping due to the intrinsic charge transfer from the SiC substrate. Upon Tl deposition, electron doping increases so that the Dirac point shifts to higher binding energies, away from the Fermi level. We attribute this to charge transfer from the Tl atoms to the graphene. The largest energy shift we observed was $\Delta E \approx 0.2\,\mathrm{eV}$. For concentrations higher than 1%, the trend is reversed, and the Dirac point shifts back towards the Fermi level. We ascribe this to the statistical effect that for concentrations higher than about 1% pairing and clustering of atoms become non-negligible, which reduces the efficiency of charge transfer doping [169].

This statement is confirmed by temperature dependent measurements, where we observe and confirm that Tl atoms are extremely mobile on the graphene surface at higher temperatures (cf. [168]). This is illustrated in the temperature dependence of the relative energy shift of the Dirac point in Fig. 6.2(a) for a Tl coverage of 0.5%. Above 15K, a rapid decrease in doping efficiency can be observed, which we attribute to clustering of Tl atoms. We conclude that Tl is only very weakly and not covalently bonded to the graphene and thus migration barriers are very small. For this reason in the following we will concentrate on the dilute limit below 1% and investigate it at low temperatures, where clustering effects can be neglected.

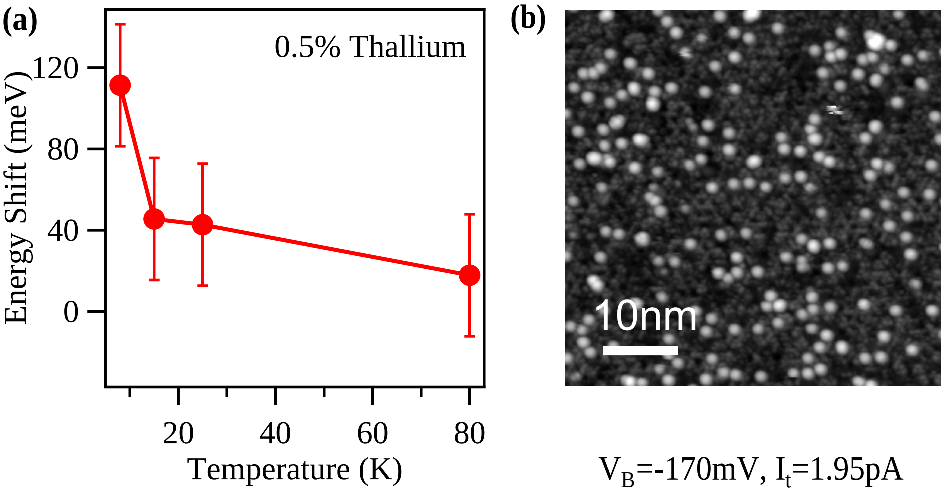

Figure 6.2: Coverage calibration and temperature dependency. (a) Temperature dependence of the doping efficiency. The energy axis shows the energy shift of the Dirac point relative to the clean graphene sample. (b) Topographic STM image of a Tl covered graphene surface ($x = 0.2\%$) at a temperature of 4.5 K. The Tl atoms appear as large protrusions with diameter of about 2 nm.

To support the assumption that we are dealing with isolated Tl atoms on the surface, STM measurements were performed at very low temperatures in Vancouver. The measurements performed at 4.5 K demonstrate that at very low concentrations Tl atoms are present as immobile monomers on the surface [see Fig. 6.2(b)]. The topographic image shows a Tl covered graphene monolayer. Even at a coverage of 0.2%, a small fraction of adsorbed Tl appears to be in dimer or trimer form, however the vast majority appear to be Tl monomers. Although the large size of the Tl adatoms and graphene's inherent electronic inhomogeneity make an identification of the adsorption site difficult, Tl atoms on more uniform graphene patches appear to sit on the hollow site, in agreement with density functional theory (DFT) calculations [162]. As the precise coverage is important for the subsequent quantitative analysis of the ARPES data, the STM results were also used for the precise flux calibration of the Tl evaporator.

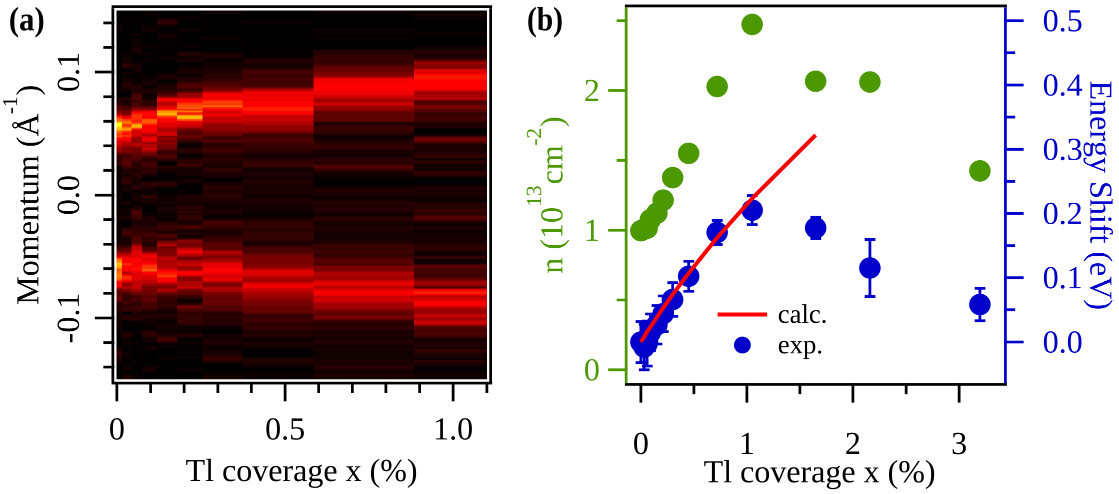

Figure 6.3: Doping effect: (a) Evolution of the Fermi wave vector k_F at $\overline{\mathrm{K}}$ for increasing Tl coverage x. (d) Charge carrier density, and experimental as well as calculated energy shift of the Dirac point as a function of Tl coverage x.

The shift of the Dirac point to higher binding energies upon Tl deposition illustrated in Fig. 6.1 corresponds to an increase of the Fermi surface volume. The corresponding evolution of Fermi wave vector k_F, as well as the charge carrier density n and the energy shift, are shown in Fig. 6.3(a) and (b), respectively. Below a coverage of 1%, all three parameters increase monotonically. The energy shift reflects the increase in occupation due to the donation of electrons by the Tl atoms. A simple model employing graphene's linear density of states serves to estimate the number of electrons donated per Tl atom η via

$$x\,\eta = \int_{E_F^0}^{E_F^x} n(\epsilon)d\epsilon, \quad \Delta E = E_F^x - E_F^0$$

The Fermi level before and after the deposition is determined experimentally and the coverage is known as well. The only free parameter is η. The best fit for low coverages is found for $\eta = 1.0$ electrons donated by a Tl atom to the graphene layer. This is also in excellent agreement with recent DFT calculations for Tl adatoms on graphene [162].

6.3 Linewidth analysis and theoretical description

In a Fermi liquid, linewidth broadening at the Fermi level due to interactions vanishes proportional to T^2 when the temperature goes to zero. Consequently, at a constant low temperature, linewidth broadening at the Fermi level from electron-electron, electron-phonon or electron-plasmon interactions can be regarded as a small, constant contribution. Other contributions are predominantly due to scattering from disorder such as impurities and defects. To extract the scattering information we analyze the linewidth of the measured spectra. The linewidths are taken from the FWHM of the MDCs at the Fermi level. We fitted the MDCs with a Voigt function and extracted the linewidths as a function of Tl coverage as shown in Fig. 6.4(a). The width of the Gaussian resolution function was set to match the experimental momentum resolution $0.016\,\text{Å}^{-1}$, while the linewidth, presented in Fig. 6.4(b) corresponds to the FWHM of the Lorentzian lineshape.

Upon increasing Tl coverage, the linewidth increases monotonically. This is due to scattering from the randomly adsorbed Tl atoms. We assume that the linewidth that we measure for the clean sample comes from initial disorder, defects and residual interactions, and enters as a constant offset in every measurement. This assumption is justified as long as we stay at a constant low temperature, which results in small contributions from interactions. In order to unravel the contributions from the Tl-induced linewidth broadening and thus the corresponding contribution to graphene's electrodynamics, we discuss two scattering mechanisms in more detail.

6.3.1 Long-range scattering

Since Tl donates one electron per atom to the graphene sheet the atoms stay as charged impurities on top. The first mechanism that takes effect is scattering from charged impurities. Due to the screened Coulomb potential the Tl atoms show a long-range effect and can be treated as long-range Coulomb scatterers. As described in Sec. 3.1.2, the linewidth is proportional to the imaginary part of the self-energy. Therefore, the linewidth broadening can be directly expressed via the imaginary part of the self-energy for long-range scattering [170]:

$$\mathrm{Im}\Sigma_{\mathrm{long}} = \alpha^2 n_{\mathrm{imp}} v_F \pi I(2\alpha)/k_F \tag{6.1}$$

where α is the effective fine-structure constant, $I(2\alpha)$ is a function defined in [171], v_F is the Fermi velocity, n_{imp} is the impurity density (which relates to the Tl concentration x via $n_{\mathrm{imp}} = 2\,x/A$ where A is the area of the graphene unit cell), and $k_F = \sqrt{\pi(\eta n_{\mathrm{imp}} + \eta_0)}$

is the Fermi momentum with η being the number of electrons donated per impurity atom, and η_0 the charge density in graphene before Tl deposition.

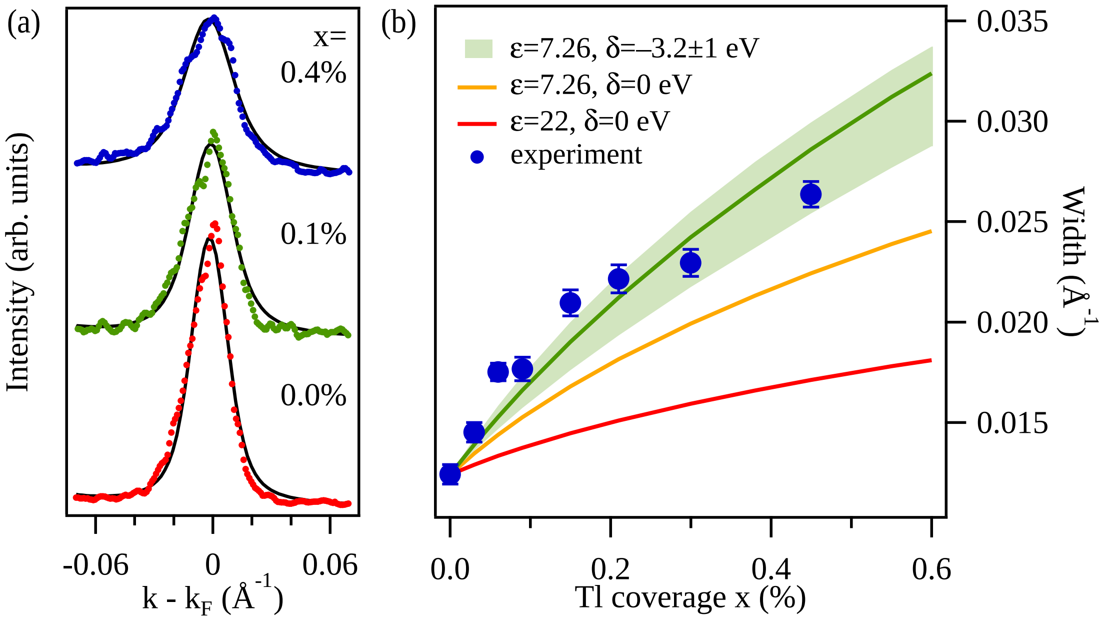

Figure 6.4: Analysis of the experimental linewidth at the Fermi level. (a) Momentum distribution curves (MDCs) at the Fermi level for different Tl coverages x with the corresponding fitted Voigt functions. (b) Increase of the linewidth as a function of Tl coverage x and the results of the model calculations using different parameters. Due to the strongly non-linear behavior of the function the shaded green region is not symmetric around the green line.

The only free parameter in Eq. 6.1 is the effective fine-structure constant of graphene; all other parameters can be determined from the experiment. The effective fine structure constant depends on the dielectric constant ϵ through $\alpha = 2.2/\epsilon$. The dielectric constant in turn is determined by the underlying substrate; the smaller its value, the stronger the long-range scattering contribution to the linewidth broadening. From the analysis of plasmaron signatures in epitaxial graphene on a buffer layer on SiC(0001) [172], the dielectric constant has been determined to be $\epsilon = 22 \pm 8$. Using this value of ϵ in Eq. 6.1, we calculated the linewidth for long-range scattering. Starting with graphene's single particle Green's function [173] we derived a theoretical spectral function by taking into account the self-energy [Eq. 6.1] and a constant offset for residual broadening. To be able to compare the theoretical spectrum to the measured data we performed an analogous Lorentzian MDC fit procedure and determined the theoretical linewidth at the appropriate binding energy, corresponding to the position of the Fermi level in the experiment. The resulting values are shown in Fig. 6.4(b) in red, and clearly do not fit the measured linewidth evolution with Tl coverage.

Recent calculations, however, point towards an overestimation of the dielectric constant [174], suggesting that the actual value is likely smaller. Indeed, by analyzing the band velocity renormalization in epitaxial graphene, a reduced value $\epsilon = 7.26 \pm 0.02$ was found [175]. The linewidth broadening from long-range scattering for this value of the dielectric constant is shown as a yellow line in Fig. 6.4(b). However, also this value of ϵ only accounts for part of the experimental linewidth broadening. It is impossible to describe the data in Fig. 6.4(b) without going to physically unreasonable values of ϵ. Therefore, another mechanism is likely to contribute to the experimental linewidth.

6.3.2 Short-range scattering

A second prominent scattering mechanism that arises in the presence of disorder is short-range scattering from an effective δ-potential. Short-range scattering is appreciable when adatoms have states close to the Fermi level, thereby inducing a sizeable scattering potential [167,176]. Its effect on the linewidth broadening can be modeled by the self-energy within the Wolff-Clogston-model [177,178]. This approach does not distinguish between inter- and intravalley scattering in graphene, but it gives a general trend about the strength of short-range scattering. We adopt a self-consistent implementation in the dilute limit within the coherent potential approximation [179]

$$\mathrm{Im}\Sigma_{\mathrm{short}}(\omega) = x\,\delta\,\mathrm{Im}\left(1 + \frac{\delta G^0(\omega - \Sigma(\omega))}{1 - \delta G^0(\omega - \Sigma(\omega))}\right)$$

where $G^0(\omega)$ is the lattice Green's function of the unperturbed graphene lattice [173] and δ is the scattering potential. As Tl concentration x as well as the lattice Green's function are known [the latter is displayed in Fig. 6.5(a)], the only free parameter in the short-range scattering model is the scattering potential parameter δ.

To evaluate the combined effect of both scattering processes, we add the self-energies for long-range and short-range scattering, and calculate the theoretical linewidth like described in Sec. 6.3.1. To this end, we note that ϵ and δ cannot be found simultaneously based on our scattering analysis; however, using the experimentally determined value of ϵ from Ref. [175], δ remains as the only unknown parameter and can thus be determined directly from the observed linewidth evolution versus Tl concentration. We find good agreement with the experimental data for $\epsilon = 7.26$ and $\delta = -3,2 \pm 1\,\mathrm{eV}$ [see shaded green area in

Fig. 6.4(b)]. As it turns out, the contributions from short-range and long-range scattering have comparable magnitudes.

The overall behavior of the imaginary part of the short-range scattering self-energy for graphene is shown in Fig. 6.5(b). Its rather strong energy dependence is due to the special energy dependence of the graphene lattice Green's function in conjunction with that of the scattering potential itself [Fig. 6.5(a)]. The dependence on the scattering potential δ at the energy $\omega = 0.5\,\mathrm{eV}$, thus in the vicinity of the experimentally relevant energies, is shown in Fig. 6.5(c). For $\delta \to \pm\infty$, which can be interpreted as a missing atom in the lattice, the imaginary part approaches the same finite value. For small values of δ, we see that the imaginary part of the self-energy varies more rapidly, although it remains bounded. Therefore, the contribution from short-range scattering to linewidth broadening is limited for $\omega \gtrsim 0.5\,\mathrm{eV}$, but not necessarily negligible, and exhibits a maximum value for $\delta \approx -5\,\mathrm{eV}$.

When comparing the value obtained here for δ with available calculations in the literature [162], we have to keep in mind that our short-range scattering model does not distinguish between different angular momentum channels, but rather attributes equal scattering amplitude to all scattering channels. Nevertheless, we can estimate a value for δ from the formula $\delta = t_{\mathrm{ad}}^2/|\Delta E|$, where t_{ad} is the hopping onto the Tl adatom and ΔE is the energy difference between the unperturbed and free Tl adatom states and the Fermi level [167, 176]. From the parameters reported in Ref. [162], we can estimate a theoretical value δ_{th} ranging between -1 to $-4\,\mathrm{eV}$. Therefore, our results suggest that short range scattering in this system lies on the larger side of the theoretically predicted range. Since the resulting value for δ is close to the minimum of the imaginary part of the self-energy [see Fig. 6.5(c)], we expect a sizeable contribution of the short-range scattering potential to the linewidth broadening.

6.4 Graphene as topological insulator

Graphene was the first material predicted to be a 2D TI, in which the SOC opens a band gap at the Dirac point [31]. However, the SOC is very weak in carbon atoms and the gap is unobservably small ($\sim 10^{-3}\,\mathrm{meV}$). Further theoretical studies suggest that the gap can be substantially enhanced by small amounts of adatoms on top of a graphene sheet. As mentioned in Sec. 6.1, Tl was proposed to be the perfect candidate to increase the SOC strength in graphene and induce a energy gap at the Dirac point [162]. By using symmetry arguments, density functional theory (DFT), and tight-binding simulations the

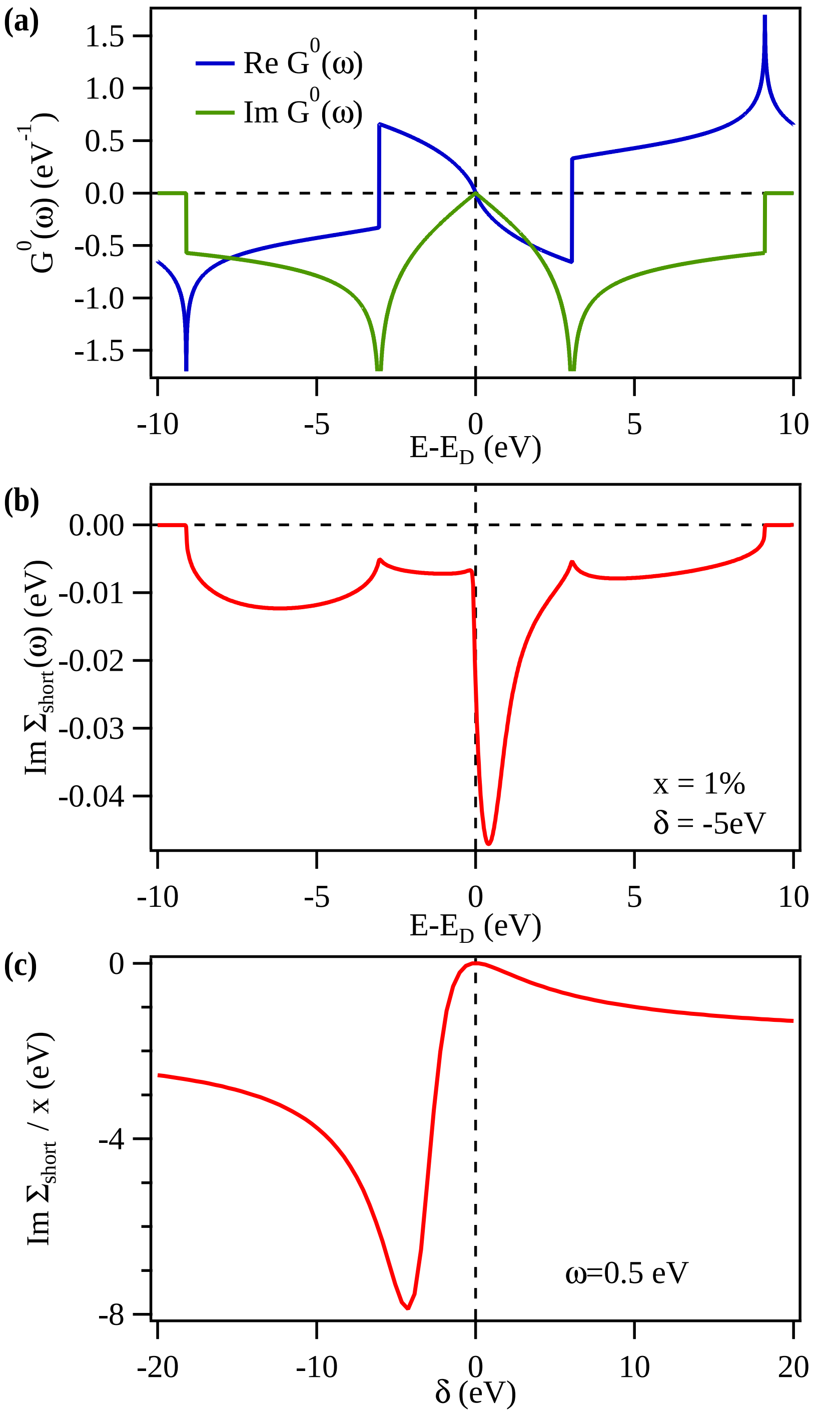

Figure 6.5: Short-range scattering model. (a) Real and imaginary part of the lattice Green's function for graphene. (b) Imaginary part of the self-energy for the short range scattering. (c) Self-energy as a function of scattering potential δ at constant energy and normalized with respect to the Tl coverage.

authors predicted that Tl and In should be able to produce a substantial band gap on the order of 21 meV and 8 meV, respectively, already at low coverages. However, there is no experimental proof of that proposal so far. In contrast, our ARPES and some transport measurements in Ref. [180] did not find any indication for a gap at the Dirac point nor a topological state. A robust topological phase in graphene would pave the way for a new generation of spintronics devices and quantum information processing. However, our ARPES and the transport measurements in Ref. [180] could not find any indication for a gap at the Dirac point nor a topological state.

6.5 Discussion

We have elucidated two different scattering mechanisms in Tl doped epitaxial graphene on SiC(0001). Similar effects of enhanced scattering due to impurities have been observed in a number of transport experiments [163, 181, 182], in agreement with our findings. There, the main scattering indicator is the carrier mobility, which decreases linearly with increasing impurity density. In contrast, a decreasing photoemission linewidth upon potassium doping has been reported by Siegel *et al.* [157]. We attribute this variance to the different doping regime, and correspondingly different intrinsic screening, that were probed in the experiments. Carrier scattering mechanisms in graphene (including charge impurities, resonant scatterers, and ripples) have been strongly debated [163, 183], and predominance of one or the other mechanism is largely sample dependent. For graphene subjected to charged impurities, e.g. alkali adatoms, long-range scattering is typically expected to be much more effective in charge carrier scattering than short range scattering [181, 184, 185]. Tl adatoms on graphene, having an impurity charge of $+1$, might be expected to behave in a similar fashion. We showed, however, that this is a system where both mechanisms have nearly equal contributions due to the proximity of Tl states to the Fermi level. More generally, this implies that it cannot be *a priori* assumed what scattering mechanism will dominate in any given impurity-graphene system.

In summary, we used the experimental spectral function measured by ARPES on Tl-doped epitaxial graphene to observe the scattering behavior induced by the Tl adatoms, and disentangle Coulomb (long-range) from δ-like (short-range) scattering contributions. Exploiting the fact that correlation effects are suppressed at the Fermi level (Luttinger's theorem), at low temperature the spectral linewidth at the Fermi level reflects predominantly defect and disorder contributions. Both long-range and short-range scattering mechanisms can be described by an analytic expression for the self-energy in the dilute limit. Fitting the self-energy to the experimental data allowed us to extract the fundamental parameters of the scattering mechanisms at play in the graphene layers.

Chapter 7

Circular dichroism in the band structure of surface alloys

Changing the photon source from non-polarized light to linearly or circularly polarized light in an ARPES experiment affects the measured photocurrent considerably. For different polarizations dipole selection rules lead to different cross sections for the interaction between polarized light and matter. Recently, ARPES setups combined with a circularly polarized light source are seen to be a perfect tool to measure the chiral spin structure of surface states [186–189]. Our CD measurements on surface alloys on Ag(111), however, show that CD is strongly dependent on the photon-energy and contains only indirect information about the spin structure. Instead of following the spin direction, CD is dominated (i) by the geometry of the experimental setup, (ii) by the dipole selection rules and hence by the OAM and (iii) by the final state. In TIs for example the spin is aligned with the OAM due to the very strong SOC [190–192]. As long as final state effects do not enter, the CD signal shows twofold symmetric structures that can be mistaken for the z-component of the spin.

In the following section, we will introduce the concept of CD. After the presentation of our results from the measurements on the surface alloys we will discuss possible interpretations. At the end, we address the question of whether there is a chance to obtain access to the spin polarization of surface states via CD measurements.

7.1 Circular dichroism in the angular distribution of photoelectrons

In general, CD is the difference in the absorption of left-handed circularly polarized light (LCP) and right-handed circularly polarized light (RCP). It is known from chiral molecules that they show selective absorption of RCP and LCP. Dichroic signals are also used in X-ray magnetic circular dichorism (XMCD) experiments, where the difference spectrum of two x-ray absorption spectra is taken in a magnetic field. This technique gives access to the magnetic properties of an atom or a molecule. Information about spin and orbital magnetic moment can be obtained. But even if magnetic field and chiral sample are absent, dichroism effects can still be observed. For ARPES measurements the difference of the photoemission spectra for both polarizations is taken and the measured signal is called 'circular dichroism in the angular distribution of the photoelectrons'. The most important requirement for a dichroic signal is a definite handedness of the combined system of photons and reaction partner. If the sample itself is non-chiral, the experimental geometry can still induce chirality. In principle every crystal shows CD effects if the direction of photon impact $\vec{q}$, photoelectron momentum $\vec{k}$ and surface normal $\vec{n}$ are non-coplanar [193].

To gain information about the spin of a system with ARPES, the interaction between light and matter in the experiment has to be spin-dependent. Using circularly polarized light and changing the polarization provides the possibility to induce a spin dependency. There are two proposals for spin-dependent interaction Hamiltonians, where the authors claim to measure the spin signal of the surface states ([186] and [187]). However, in both models assumptions about the geometry of the sample or about the spin polarization of the bands are necessary.

For the interpretation of CD data, it is important to understand its origin. Presumably SOC plays an important role. However, it is definitively not the only ingredient because also very light atoms show a strong CD effect e.g. graphene [194]. There are also other factors that have an influence on the CD signal, like the geometrical setup [193] and the photon energy [195], which were so far mainly ignored by the community. Recently, it was proposed that the CD signal is proportional to the OAM [196]. Based on this fact the question arises whether it is actually possible to probe the spin of the initial state with CD-ARPES.

7.2 Photoemission experiments

We performed ARPES experiments with circularly polarized light on Bi/Ag(111) and Sb/Ag(111) surface alloys. The measurements were performed at the Synchrotron Radiation Center (SRC) in Stoughton, Wisconsin [for details see Sec. 3.2]. A sketch of the experimental setup is displayed in Fig. 7.1.

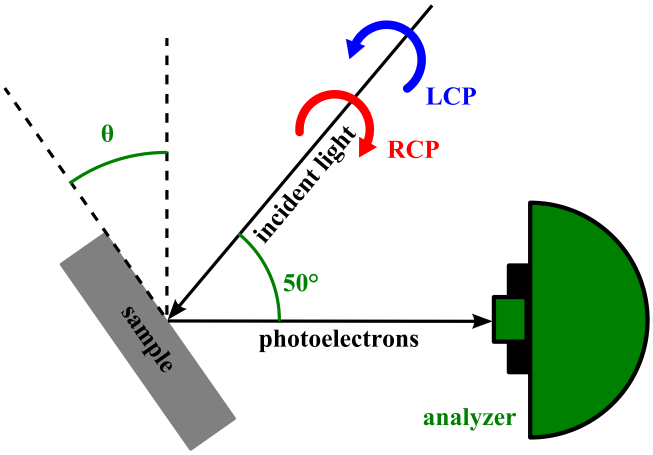

Figure 7.1: Sketch of the experimental setup for CD measurements.

For RCP (LCP) light the electric field vector rotates anticlockwise (clockwise) around the direction of light propagation. In order to measure the photoemission current as a function of k_y the sample was rotated by an angle θ [see Fig. 7.1]. k_x (direction perpendicular to the paper plane in Fig. 7.1) corresponds to the angular dispersion direction in the 2D detector.

To prepare the surface alloys the Ag(111) substrate has to be cleaned by several sputtering/annealing cycles. We sputtered the surface with Ar ions with an energy of 1 keV and at an Ar pressure of $1 \cdot 10^{-6}$ mbar and subsequently annealed the sample at 530°C. Cleanliness of the substrate was controlled by monitoring the surface state of Ag(111) with ARPES. On the clean Ag(111) surface one third of a monolayer of Bi or Sb is deposited using a commercial electron beam evaporator. The Ag crystal was kept at 420°C and 250°C for Bi and Sb deposition, respectively. For the measurements, the sample temperature was ~50 K.

In Fig. 7.2 the results of the ARPES measurements are shown for RCP and LCP light as well as the difference (CD) in $\overline{\Gamma \mathrm{M}}$ direction of the Bi/Ag(111) surface alloy measured with a photon energy of $h\nu = 29$ eV.

The 2D band structure in surface alloys on Ag(111) consists of three sets of spin-split

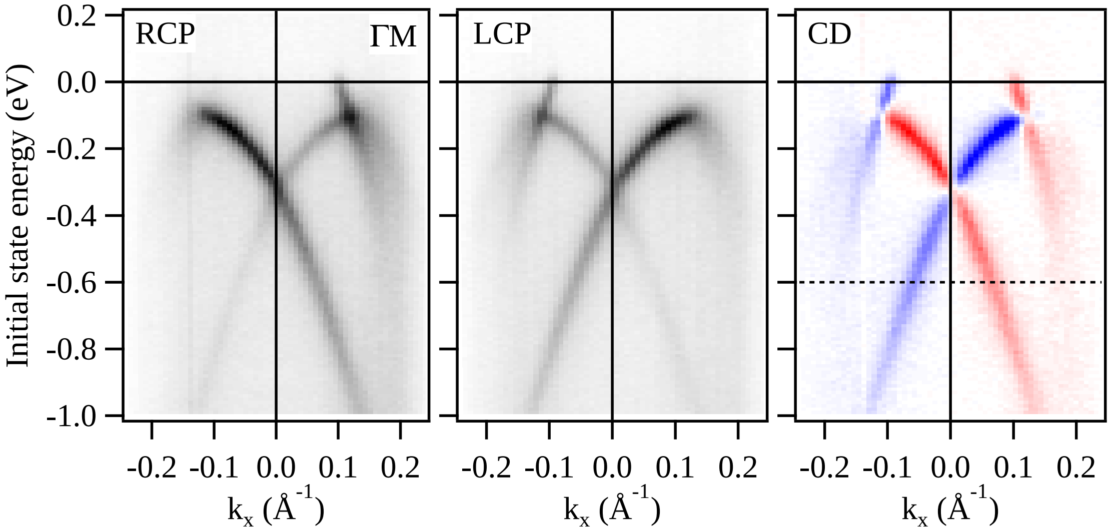

Figure 7.2: Band structure of Bi/Ag(111): The spectra are measured in $\overline{\Gamma \mathrm{M}}$ direction at a photon energy of hν = 29 eV for RCP and LCP, on the left and in the middle, respectively. The right panel show the intensity difference (CD= $I_{RCP} - I_{LCP}$). Red (blue) corresponds to positive (negative) values, white corresponds to zero.

bands; one at lower binding energy with mainly sp_z character, two at higher binding energy with mainly p_{xy} character and $m_j = 1/2; 3/2$ [66]. The measurements of Bi/Ag(111) show the known, large spin splitting of the lowest band [63]. The intensity of the parabolas varies strongly with the polarity of the light. Parts of the band structure are only visible for RCP and others only for LCP light. By taking the difference one gets the CD image, in which each parabola of the sp_z spin-polarized band has its own color. Red (blue) means the intensity for RCP (LCP) light was higher and white means that the intensity was the same for both polarizations. Close to the Fermi energy we see that also the p_{xy} bands show a CD signal.

Fig. 7.3 shows ARPES results for the same measurements conditions but for Sb/Ag(111). The atomic SOC in Sb is much weaker. Therefore, the spin splitting is much smaller and we do not resolve it in the sp_z band, but we see just one parabola. Nevertheless, we observe a clear dichotomy in the CD signal. Despite the fact that the band is spin degenerate it is bicolored in the CD image and gives us direct proof that CD cannot be an independent, direct measure for the spin structure.

Measured constant energy planes for both alloys at $E_B = 0.6$ eV are displayed in Fig. 7.4. The measurements show that CD vanishes in $\overline{\Gamma \mathrm{K}}$ direction. For Bi/Ag(111) only the inner band is visible at this energy and shows a twofold symmetry. In the case of Sb both

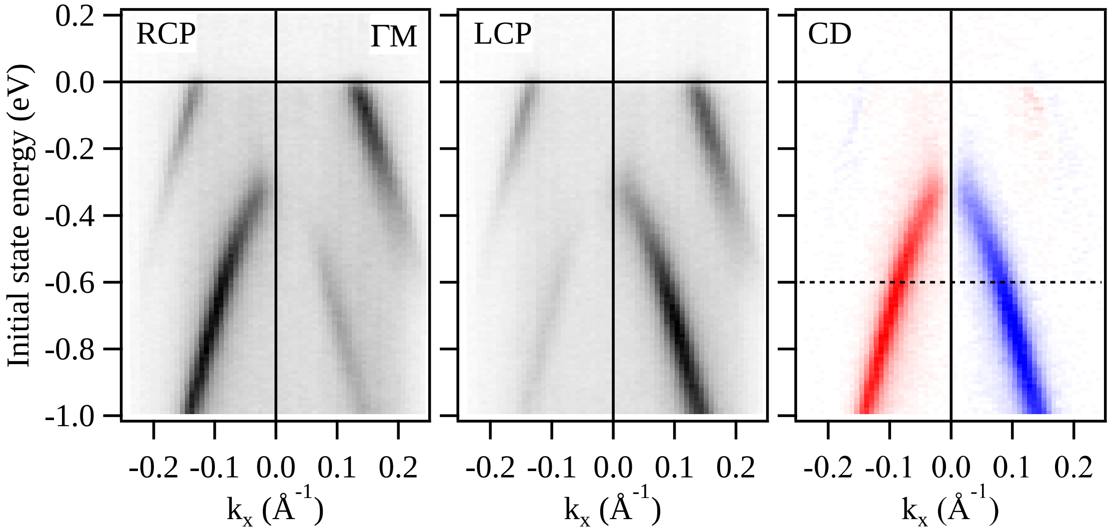

Figure 7.3: Band structure of Sb/Ag(111): The spectra are measured in $\overline{\Gamma \mathrm{M}}$ direction at a photon energy of hν = 29 eV for RCP and LCP, on the left and in the middle, respectively. The right panel show the intensity difference (CD= $I_{RCP} - I_{LCP}$). Red (blue) corresponds to positive (negative) values and white to zero.

bands are visible. For the inner band the dichotomy is clearly confirmed, but the CD signal of the outer band changes sign four times on a circle around $\overline{\Gamma}$. The difference between both bands is the orbital character. We observe that different initial states give rise to CD signals with different symmetries.

7.3 Theoretical description

In order to explore the origin of CD and explain our observations, we take a very simple approach, i.e. the model for CD of Schönhense [193]. This model states, that in principle, every crystal shows CD if the criterion for the appearance of CD effects is fulfilled; the direction of photon impact $\vec{q}$, photoelectron momentum $\vec{k}$ and surface normal $\vec{n}$ must be non-coplanar. For the calculation of the transition matrix element the electric dipole operator for RCP and LCP and the corresponding selection rules are taken. The final state is expressed as a partial wave expansion and can be written as $\Psi_f = 4\pi \sum_{l'm'} F_{El'}(r)(i)^{l'} e^{-i\delta_{l'}} Y^*_{l'm'}(\hat{k}) Y_{l'm'}(\hat{r})$. Here, l' gives the orbital of the final state, $F_{El'}$ stands for the radial wave functions, $\delta_{l'}$ represents the phase shifts experienced by the outgoing partial waves, and $\hat{k}$ and $\hat{r}$ specify the photoelectron emission direction and the

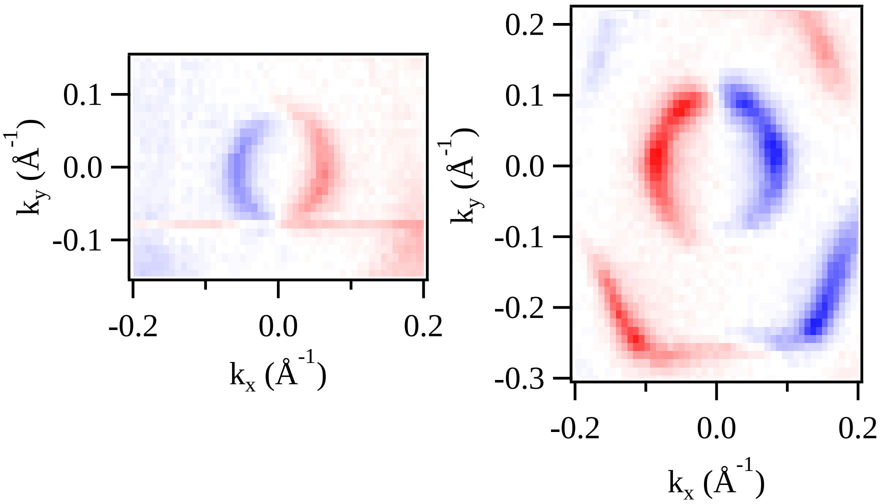

Figure 7.4: Measured constant energy planes cut through the band structure of Bi/Ag(111) (left) and Sb/Ag(111) (right) at $E_B = 0.6\,\mathrm{eV}$ as indicated in the CD images in Fig. 7.2 and Fig. 7.3.

direction of the position vector, respectively. S-orbitals do not give any contribution to the CD signal because of their spherical symmetry that cancels out all CD effects. If we consider the geometry of our experimental setup, including the direction of light incidence $(50^\circ - \theta)$ and of electron detection $(\theta;\phi)$, we find the following CD signal depending on the initial state [193, 197]:

$$\begin{aligned}
CD(p_x) &\propto -\frac{R_sR_d}{2\pi}\sin(\delta_s-\delta_d)\sin^2(\theta)\sin(2\phi)\cos(50^\circ-\theta)\\
CD(p_y) &\propto +\frac{R_sR_d}{\pi}\sin(\delta_s-\delta_d)\sin(\theta)\sin(\phi)\times\\
&\qquad(\sin(\theta)\cos(\phi)\cos(50^\circ-\theta)+\cos(\theta)sin(50^\circ-\theta))\\
CD(p_z) &\propto -\frac{R_sR_d}{2\pi}\sin(\delta_s-\delta_d)\sin(2\theta)\sin(\phi)\sin(50^\circ-\theta)
\end{aligned}$$

with the radial part of the matrix elements R_s and R_d. These equations are plotted in Fig. 7.5.

Like in our experimental data, the simple model calculations show also that in $\overline{\Gamma\mathrm{K}}$ direction there is no CD signal. The reason for no signal at $k_x = 0$ is the symmetry of the orbitals and the experiment. Symmetry also requires that the sum over all p-orbitals gives zero. The calculations confirm that different initial states lead to different symmetries in the CD signals: CD of the p_z and p_y orbital is at first sight twofold symmetric whereas

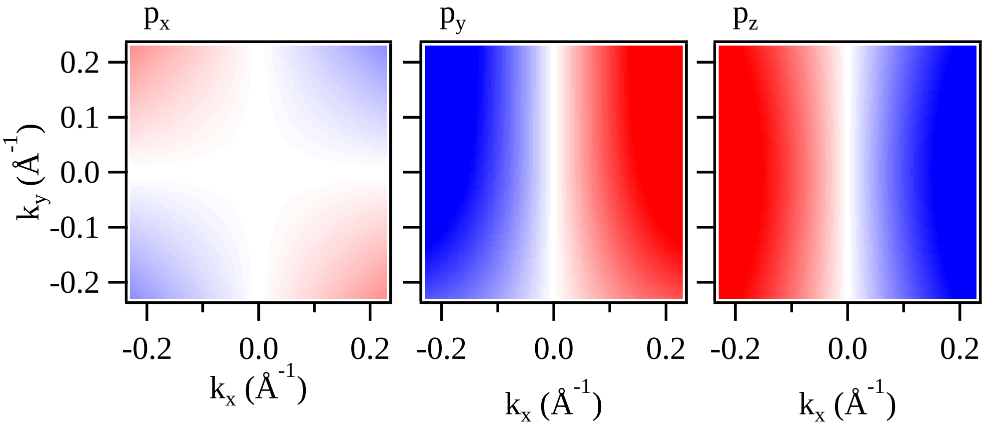

Figure 7.5: Results of the model calculations using Schönhenses model combined with the geometry of the experimental setup for a p_x, p_y or p_z orbital as initial state from left to right, respectively.

the p_x shows a fourfold symmetry. This agrees very much with our measurements where the sp_z band changes sign two times and the p_{xy} band four times on a circle around $\overline{\Gamma}$. Overall, the simple theoretical findings are in very good agreement with our experimental observations.

7.4 Orbital angular momentum in surface alloys

So far, our observations fit also very well to those of Kim et al. [198] and of Park et al. [191]. They performed DFT and first-principles calculations and showed that CD follows the OAM. The OAM, in combination with the electron momentum $\vec{k}$, leads to small electric dipoles (asymmetric charge distribution) that have opposite orientation for opposite OAM directions. The surface electric field aligns the electric dipoles and splits the states through the electric dipole interaction.

The alignment of the spin angular momentum (SAM) is a consequence of strong SOC and the chiral OAM structure: For small SOC the spin moment is either parallel or anti-parallel to the OAM. For strong atomic SOC, however, the OAM is always pointing in the opposite direction of the SAM and the bands show a significant spin splitting. Exactly this has been observed in our measurements; in Sb/Ag(111) the OAM is parallel for both bands (spin splitting is not resolved in our experiments) because the SOC is too weak to align the SAM and OAM. The situation in Bi is different; there, SOC is strong enough to align SAM and OAM. The spin is pointing anti-parallel for the inner and the outer band and the

OAM follows this structure with the opposite sign. For the inner band we observe a CD signal where the intensity varies proportional to a sinusoidal curve on a circle around $\overline{\Gamma}$. This is shown for the case of Bi/Ag(111) and $h\nu = 25\,\mathrm{eV}$ in Fig. 7.6. Due to the similarity, such a signal is often misinterpreted as proof of the chiral structure in the SAM [27].

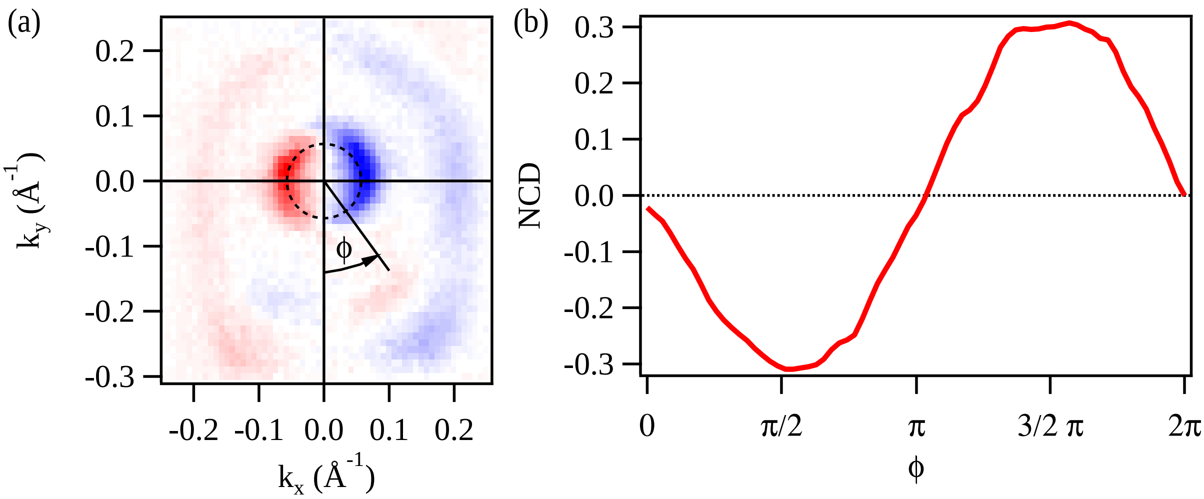

Figure 7.6: Normalized CD signal on a circle around $\overline{\Gamma}$ (a) Measured constant energy plane cut through the band structure of Bi/Ag(111) at $E_B = 0.6\,\mathrm{eV}$ with $h\nu = 25\,\mathrm{eV}$ (b) Absolute values of the normalized CD signal on a circle indicated in (a) around $\overline{\Gamma}$.

7.5 Photon-energy dependence

We have seen that SOC plays a crucial role for CD measurements and that the CD signal follows mainly the OAM. Additionally, the experimental setup is just as important as the last ingredient; the photon energy. The choice of the photon energy determines the final state in which the excited electron goes. According to the dipole selection rules combined with circularly polarized light only certain transitions are allowed. Depending on the energy, different final states are available and the corresponding CD signal can change completely. It can vanish or even reverse its sign. Fig. 7.7 shows the CD signal for different photon energies (25 eV, 45 eV and 90 eV) of Bi/Ag(111).

The data show the normalized CD signal $\mathrm{NCD} = (I_{RCP} - I_{LCP})/(I_{RCP} + I_{LCP})$, which is the difference of the measured spectra divided by the sum. The sign of NCD in the sp_z band changes for different photon energies. At $h\nu = 25\,\mathrm{eV}$ and a binding energy of $E_B = 0.6\,\mathrm{eV}$ the left branch is red, i.e. the intensity for RCP light was higher. For 45 eV and 90 eV it

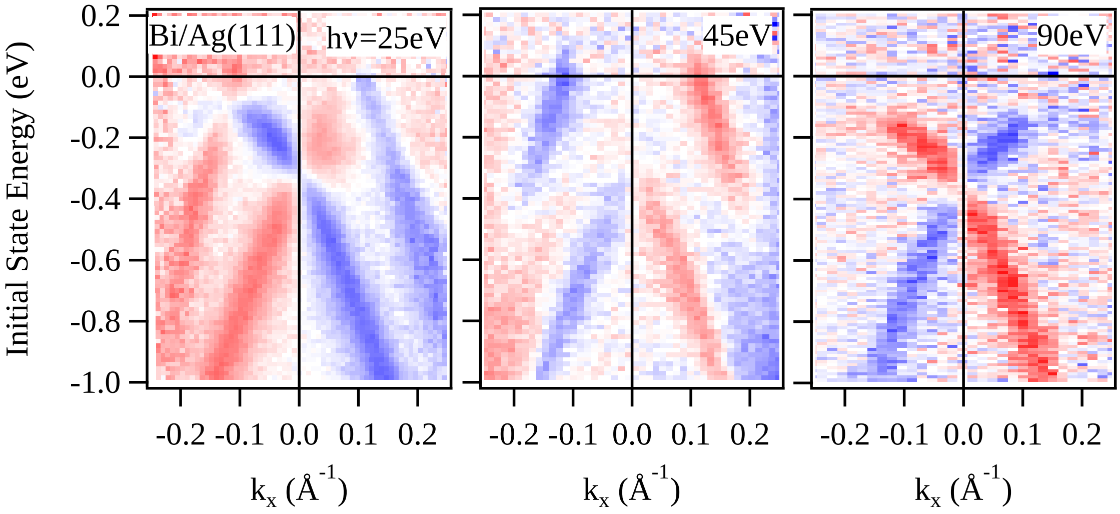

Figure 7.7: CD signal of the band structure in Bi/Ag(111) for different photon energies. Changing the energy results in a change of the final state symmetry and thus in a change of the sign of the CD signal. Matrix elements effects lead to different intensity patterns. The color code goes from blue (-0.6) to red (0.6).

is blue and the intensity for LCP was higher. In order to evaluate this quantitatively we extracted the maximum value of the normalized CD at an MDC at $E_B = 0.6\,\mathrm{eV}$ for both branches. The result is presented in Fig. 7.8.

From this plot it can be easily seen that final state effects play the most important role in CD measurements and in the data interpretation [195]. In the energy window from 25 eV to 90 eV, the CD changes sign several times. For some energies CD even vanishes (see the sp_z band at 45 eV above the crossing point). Despite this strong influence, final state effects and the resulting photon energy dependence have rarely been discussed by the community to date. The usual approach was always to explain CD by various initial-state models favoring the spin or OAM as origin for CD. However, none of these can describe all the experimental observations and final state effects have to be considered [195].

Even in the simple model of Schönhense, the sign change due to the final state is included via the factor $sin(\delta_s - \delta_d)$. In our experiments we found even a case where the CD signal changes sign within one branch for the same photon energy. For example, for Sb/Ag(111) at $h\nu = 55\,\mathrm{eV}$ [see Fig. 7.9]. Such a sign change was also observed in Ref. [190] and calculated in Ref. [192]. Also this phenomenon can only be explained by a transition into a new final state.

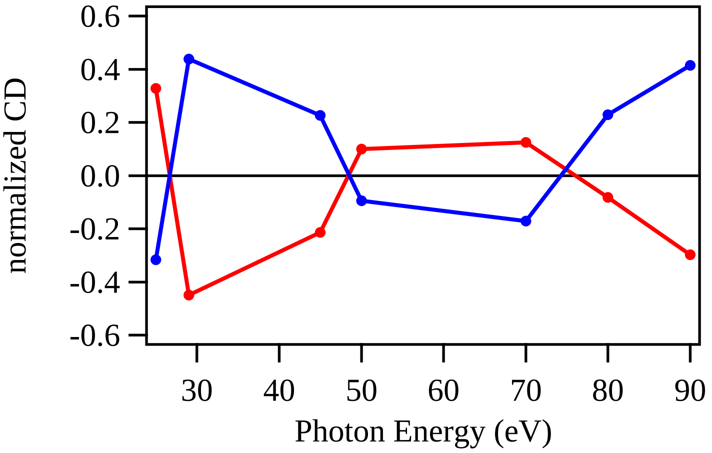

Figure 7.8: Photon energy dependence of the band structure in Bi/Ag(111). The maximum value of the normalized CD in both branches of the sp_z band at $E_B = 0.6\,\mathrm{eV}$ is shown. The normalized CD changes sign at several photon energies.

7.6 Discussion

The presented ARPES study with circularly polarized light shows that the photon energy plays a very important role for the interpretation of CD data. To describe the experimental data the model of Schönhense [193] is very useful. In this model CD is a consequence of the interaction of circularly polarized light and the electrons in the surface. The measured CD signal is a combination of the OAM superposed with geometrical and final state effects. If we know the final state and consider carefully the geometrical setup of the experiment, we are able to measure the OAM with an ARPES setup combined with a circularly polarized photon source. In case of strong SOC we can even obtain information about the SAM, because high SOC leads to aligned SAM and OAM. However, there are also examples for spin resolved ARPES measurements where final state effects perturb the experiment [199].

In order to improve the quantitative explanation of the measured CD signal several possibilities are discussed in literature. It was claimed [186] that the experimental geometry induced matrix element effects can be eliminated by using a time-of-flight detector and measuring the whole band structure simultaneously without turning the sample. This is only true under certain circumstances because even in this setup the CD signal is affected by geometry since the direction of photon impact $\vec{q}$, photoelectron momentum $\vec{k}$ and sample normal $\vec{n}$ are still non-coplanar for most values of $\vec{k}$. The only way remove of the geometric contribution to the CD signal is to apply symmetry properties and taking the difference between CD signals measured $\Delta\phi = 60°\mathrm{C}$ apart [186]. This procedure might even allow for

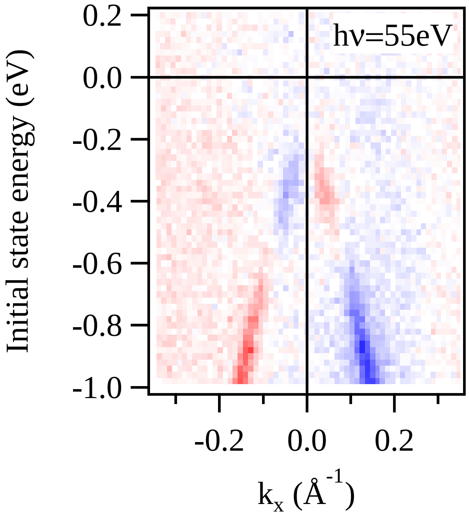

Figure 7.9: Band structure of Sb/Ag(111) at hν = 55 eV at $\overline{\Gamma}$. CD signal changes its sign within the band.

a determination of the 3D spin polarization vector. But this effect has not been investigated as a function of photon energy so far. The simple Schoönhense model has both effects included: geometry and final states. But the biggest problem is the initial state. Since the different bands are not purely s or p bands but have different orbital character it is difficult to find a description for a realistic initial state. We claim that the model would probably give a more sophisticated result for the CD signal if a more realistic initial and final state wave function is inserted.

In conclusion, we can state that analysis and interpretation of CD data has to be attempted with caution. They do not give direct access to the spin structure of surface states. What CD-ARPES experiments rather measure seems to be the OAM, but superposed with geometrical and final state effects. In the presence of high SOC the spin aligns with the OAM (either parallel or anti-parallel) and one might say that CD burrows the electron spin but it does not give direct access to it.

Chapter 8

Summary and Outlook

8.1 Summary

In this work, we have investigated several 2DESs and studied in particular the electronic properties at the surface of $TiTe_{1.5}Se_{0.5}$ and signatures of many-body physics in Bi_2Te_2Se and graphene. We showed that interactions play an important role, not only for the Dirac electrons in graphene but also for the spin-polarized surface states of 3D TIs. In addition, we also evaluated CD-ARPES as a technique to measure spin-split surface states and in order to get information about the initial state properties.

In the first part we focused on topological non-trivial surface states and their characteristics. We measured the surface band structure of Bi_2Te_2Se and observed a time-dependent doping behavior due to adsorption of residual gas molecules. By a careful analysis of the position and the linewidth of the peaks in the measured spectra we found that the band structure is strongly renormalized while the charge carrier density n is changing. The linewidth is increasing with increasing binding energy and the band velocity is smaller for low n. These observations can be explained by the strong Coulomb interaction among the electrons, since at very small n screening effects are not efficient.

We did not just investigate known TIs but have also looked for new topological materials. Therefore, we had a look at a system that is expected to exhibit a topological surface state. We measured the surface band structure on mechanically cleaved single crystals of $TiTe_{1.5}Se_{0.5}$ and could present the band dispersion for the first time. The bands disperse as expected and the inverted band gap lies above the Fermi. Since ARPES is only sensitive to the occupied states we were not able to measure any topological surface state, but the material looks like a promising TI candidate.

In the second part we studied scattering mechanisms in a doped monolayer of epitaxial graphene grown on a buffer layer on SiC(0001) by depositing Tl adatoms. To overcome the high mobility of Tl adatoms, we deposited them and performed the measurements at very low temperatures. We have quantitatively shown that Tl adatoms not only show electron doping up to a certain coverage, but also have a large effect on the quasiparticle scattering rate. The Tl adatoms introduce disorder and act on the graphene electronic structure both as Coulomb long-range scatterers as well as short-range scatterers with a δ-like potential. By modeling the self-energy for both scattering mechanisms, we are able to extract a strong short-range scattering potential $\delta = -3.2 \pm 1\,\mathrm{eV}$. Thus, short-range scattering can contribute to a sizeable increase of the scattering rate, even in the case of charged impurities where long-range Coulomb scattering is usually expected to dominate. These findings, and the ability to predict and/or account for conflating scattering mechanisms, will have important implications in the development of novel impurity-graphene-based electronics.

At last we had a closer look at ARPES measurements with circularly polarized light. By investigating two systems with different SOC strengths — Bi/Ag(111) and Sb/Ag(111) surface alloys — we were able to gain a deeper insight into the details and the challenges of CD-ARPES. We observed that CD follows not the SAM but more the OAM. A quite simple model based on the geometry and the selection rules describes the basic effects very well [27, 193]. However, we also found that the photon energy has a big impact on the measurements. For a proper interpretation of CD signals one has to consider not only the OAM of the initial state, but also the geometry of the experimental setup as well as the photon energy and thus final state effects. It is impossible to draw reliable general conclusions about the spin texture from CD measurements.

8.2 Outlook

In this section, some possible follow-up experiments and ideas for proceeding are given. Further, we will present some potential applications of the investigated materials.

Much of the theoretical research on Dirac electrons has focused on the single-particle picture since the basic physical phenomena can be calculated and explained very well both in the spin-degenerate case — graphene — as well as in the spin-polarized surface states of TIs. For example, the band structure [39], the integer quantum Hall effect [200], localization [201], and topological classification [202] are very well described in theory without interactions. However in the case of graphene, ARPES experiments [101, 157, 172, 203] have directly shown the existence of many-body quasiparticle spectra near the Dirac point, manifesting electron-electron, electron-phonon, and electron-plasmon interactions. It was proven that interactions under certain circumstances play an important role and can change the physical picture drastically.

8.2.1 Topological insulators

Recently, some experimental work on many-body interactions in TIs has also been performed. For example, Park *et al.* [204] investigated the electron-electron interaction and defect scattering in Bi_2Se_3 and claimed that topological states could be indeed protected against weak perturbations. They showed that topological metallic states are very much unaffected by the potentials created by adsorbed atoms or molecules. Transport measurements on TI thin films could demonstrate that the interplay between topological delocalization, electron interaction, and broken time-reversal symmetry play a crucial role in determining the transport properties of the TI thin films [205]. The authors addressed the question whether topological surface states are topologically protected from localization and remain metallic down to zero temperature. Up to a thickness of 6 quintuple layers, they observed an insulating ground state due to electron-electron interactions, which is enhanced by the diffusive nature of electron motion in disordered thin films.

It was also shown that electron-electron interactions lead to localization of the electrons [206] and can even destroy the topological character [6]. In particular, for very low charge carrier densities and low dielectric constants, electron-electron interactions in TIs are not negligible [59], as was also shown in this work. Interactions lead to a more complex physical picture and make the description often difficult, but usually they also introduce new possibilities. For example, superconductivity was predicted in Bi_2Se_3 due to electron-phonon interactions with a critical temperature of $T_C = 1\,\mathrm{K}$. Including quasiparticle dynamics in Dirac electrons of TIs will be one important subject for upcoming experiments and theoretical studies in the field of TIs. The motivation is still to understand what turns a material into a TI and to find new topological materials with intriguing properties that are suitable for potential applications. In particular, the electronic properties of TIs hold a great potential for spintronics applications and quantum information processing [207].

For our studies, first of all it would be desirable to confirm our findings by a theoretical description that relates the electron-electron interaction constant β and the determined ratio β_1/β_2 to the dielectric constant ϵ and the charge carrier density n. Therefore, it is necessary to repeat the measurements at low temperature, which allows one to also estimate the contribution from electron-phonon interaction. Furthermore, the transfer of this method to other topological materials that have only surface states at the Fermi level is planned. For the promising TI candidate $\mathrm{TiTe_{1.5}Se_{0.5}}$, the next step would be to dope the system with some electrons in order to shift the inverted band gap into the occupied states. For example, Na could be a possible electron donor since it donates quite easily electrons without disturbing the electronic properties [166]. Furthermore, it was shown that Na can lead to energy shifts of about 0.5 eV. In addition, another possible experiment would be to measure also CD-ARPES on both topological materials.

8.2.2 Circular dichorism measurements

The determination of the spin texture of TIs is still of paramount importance for both fundamental understanding of its topological order and future spin-based applications. In this context, much experimental work on TIs was performed with spin-resolved ARPES and CD-ARPES. There are numerous proposals to use circularly polarized light to selectively couple to the surface states to generate surface spin waves [208] or spin-polarized currents [209]. By tuning the light polarization it was claimed that TIs may serve as spin-polarized electron sources [210]. As a consequence of the large OAM very strong spin-polarized currents in surface states can be induced by light. Following the dipole selection rule, an electron with s-orbital character can be excited by a photon to the p-orbitals in the surface states. Using circularly polarized photons allows one to excite electrons only in a certain part of the Brillouin zone with the proper OAM. Since the surface states are spin-polarized, selective excitation of electrons should result in spin-polarized current [191].

In particular, for the surface alloys on Ag(111) it would be desirable to observe the transition of parallel to antiparallel OAM in the surface states. It was shown that mixing of the alloy atoms allows tuning of the Fermi level and of the SOC strength [211]. With the proper ratio of Bi and Sb atoms one should be able to reach the point where the OAM is reversed for one of the bands. This would serve as perfect proof that CD-ARPES probes in principle the OAM.

8.2.3 Graphene

The knowledge we gained in our experiments with graphene is very exciting from a fundamental point of view. With our technique we are able to determine the scattering potential of short-range scattering centers. It would be interesting to investigate also other adatoms or adsorbates with regard to their scattering potential. One could also think of modifying the dielectric properties of graphene by intercalating elements and check the difference in the linewidth broadening for different dielectric constants ϵ.

The ultimate goal in the research field of graphene is still to use it in electronic devices one day. Since graphene is a semimetal, where the conduction and the valence band are touching at the $\overline{\mathrm{K}}$-points, it lacks a band gap which leads to comparatively low on-off ratios in graphene based field effect transistors. A lot of effort has been directed towards the opening of an energy gap at the Dirac point [75,102,212–215]. For example, such a band gap was realized in graphene nanoribbons due to quantum confinement of the electrons. Also, our experiments and some transport measurements [180] have aimed in this direction. Unfortunately, the theoretical predictions could not be proven, so far. However, there are already some new ideas about the gap-opening in graphene via SOC. In Ref. [216] the authors claim that a small amount of $5d$ transition metal atoms, in particular Osmium and Iridium, on top of graphene will open an even bigger gap at the Dirac point. They suggest to build a 2D TI by hybridizing graphene with impurity bands arising from heavy adatoms possessing partially filled d shells. By means of first-principles calculations they predict gaps of 0.2 eV and larger over a wide range of adatom coverage.

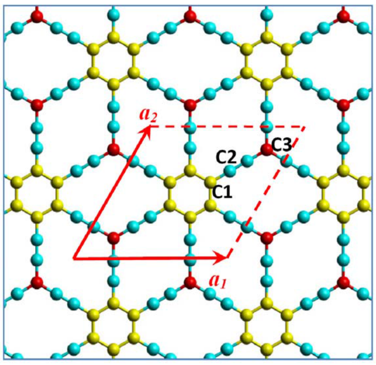

Figure 8.1: Schematic representation of δ-graphyne taken from [217]. The unit cell with the two basis vectors $\vec{a_1}$ and $\vec{a_2}$ are indicated by the red lines. According to the different chemical environments the carbon atoms are drawn in different colors.

Recently published theoretical work has proposed a new 2D TI made out of carbon [217]. The so-called graphynes, which are carbon allotropes built from triple- and double-bonded units of carbon atoms, were considerably investigated and show interesting properties. In particular, δ-graphyne [drawn in Fig. 8.1] was predicted to show a topologically nontrivial electronic structures. The energy band gap of δ-graphyne is still quite small (0.59 meV) but could be experimentally accessible at extremely low temperatures. This approach demonstrates promising possibilities for the search for new TIs in 2D carbon allotropes.

Realization of these proposals would open the door for realizing topological superconductivity, Majorana fermions, and related phenomena. It is worth mentioning, that one of the primary requirements for observing those effects is to induce superconductivity in graphene via the proximity effect, which has already been shown by several groups [218–220].

Bibliography

[1] M. Schroeder *Fractals, chaos and power laws*, W. H. Freeman and Company (1991)

[2] K. v. Klitzing, G. Dorda, and M. Pepper ‘New method for high-accuracy determination of the fine-structure constant based on quantized hall resistance’ *Phys. Rev. Lett.* **45**, 494 (1980)

[3] J. Sinova, D. Culcer, Q. Niu, N. A. Sinitsyn, T. Jungwirth, and A. H. MacDonald ‘Universal intrinsic spin Hall effect’ *Phys. Rev. Lett.* **92**, 126603 (2004)

[4] J. Wunderlich, B. Kaestner, J. Sinova, and T. Jungwirth ‘Experimental observation of the spin-Hall effect in a two-dimensional spin-orbit coupled semiconductor system’ *Phys. Rev. Lett.* **94**, 047204 (2005)

[5] Y. Ando ‘Topological insulator materials’, *J. Phys. Soc. Jpn.* **82**, 102001 (2013)

[6] M. Liu, C.-Z. Chang, Z. Zhang, Y. Zhang, W. Ruan, K. He, L.-l. Wang, X. Chen, J.-F. Jia, S.-C. Zhang, Q.-K. Xue, X. Ma, and Y. Wang ‘Electron interaction-driven insulating ground state in Bi_2Se_3 topological insulators in the two-dimensional limit’, *Phys. Rev. B* **83**, 165440 (2011)

[7] Y. A. Bychkov and E. I. Rashba ‘Properties of a 2D electron gas with lifted spectral degeneracy’, *JETP Lett.* **39**, 78 (1984)

[8] C. Kittel, *Einführung in die Festkörperphysik*, Oldenbourg Verlag (2002)

[9] I. Gierz, *Investigation of two-dimensional electron gases with angular resolved photoemission spectroscopy* Ph.D. thesis, Ecole Polytechnique Fédérale de Lausanne (2011).

[10] K. S. Novoselov, Z. Jiang, Y. Zhang, S. V. Morozov, H. L. Stormer, U. Zeitler, J. C. Maan, G. S. Boebinger, P. Kim, and A. K. Geim ‘Room-temperature quantum hall effect in graphene’, *Science* **315**, 1379 (2007)

[11] K. Oura, V. G. Lifshits, A. A. Saranin, A. V. Zotov, and M. Katayama *Surface Science An Introduction*, Springer Berlin (2003)

[12] W. Shockley 'On the surface states associated with a periodic potential', *Phys. Rev.* **56**, 317 (1939)

[13] I. Tamm 'Über eine mögliche Art der Elektronenbindung an Kristalloberflächen', *Zeitschrift für Physik* **76**, 849 (1932)

[14] H. Kramers 'General theory of the paramagnetic rotation in crystals', *Proceedings of the Section of sciences Koninklijke Nederlandse akademie van wetenschappen* **33**, 959 (1930)

[15] J. Nitta, T. Akazaki, H. Takayanagi, and T. Enoki 'Gate control of spin-orbit interaction in an inverted $\mathrm{In_{0.53}Ga_{0.47}As/In_{0.52}Al_{0.48}As}$ heterostructure', *Phys. Rev. Lett.* **78**, 1335 (1997)

[16] E. Frantzeskakis and M. Grioni 'Anisotropy effects on Rashba and topological insulator spin-polarized surface states: A unified phenomenological description', *Phys. Rev. B* **84**, 155453 (2011)

[17] U. Heinzmann and J. H. Dil 'Spin-orbit-induced photoelectron spin polarization in angle-resolved photoemission from both atomic and condensed matter targets', *Journal of Physics: Condensed Matter* **24**, 173001 (2012)

[18] G. Dresselhaus 'Spin-orbit coupling effects in zinc blende structures', *Phys. Rev.* **100**, 580 (1955)

[19] E. I. Rashba 'Properties of semiconductors with an extremum loop .1. cyclotron and combinational resonance in a magnetic field perpendicular to the plane of the loop', *Sov. Phys. Solid State* **2**, 1109 (1960)

[20] D. Di Sante, P. Barone, R. Bertacco, and S. Picozzi 'Electric control of the giant Rashba effect in bulk GeTe', *Advanced Materials* **25**, 509 (2013)

[21] Y. A. Bychkov and E. I. Rashba 'Oscillatory effects and the magnetic susceptibility of carriers in inversion layers', *J. Phys. C: Solid State Phys.* **17**, 6039 (1984)

[22] S. LaShell, B. A. McDougall, and E. Jensen 'Spin splitting of an Au(111) surface state band observed with angle resolved photoelectron spectroscopy', *Phys. Rev. Lett.* **77**, 3419 (1996)

[23] D. Popovic, F. Reinert, S. Hüfner, V. G. Grigoryan, M. Springborg, H. Cercellier, Y. Fagot-Revurat, B. Kierren, and D. Malterre 'High-resolution photoemission on Ag/Au(111): Spin-orbit splitting and electronic localization of the surface state', *Phys. Rev. B* **72**, 045419 (2005)

[24] F. Forster, S. Hüfner, and F. Reinert 'Rare gases on noble-metal surfaces: An angle-resolved photoemission study with high energy resolution', *J. Phys. Chem. B* **108**, 14692 (2004)

[25] L. Petersen and P. Hedegård 'A simple tight-binding model of spin-orbit splitting of *sp*-derived surface states', *Surface Science* **459**, 49 (2000)

[26] R. Winkler *Spin-orbit coupling effects in two-dimensional electron and hole systems*, Springer Berlin (2003)

[27] S. R. Park, C. H. Kim, J. Yu, J. H. Han, and C. Kim 'Orbital-angular-momentum based origin of Rashba-type surface band splitting', *Phys. Rev. Lett.* **107**, 156803 (2011)

[28] I. Gierz, B. Stadtmüller, J. Vuorinen, M. Lindroos, F. Meier, J. H. Dil, K. Kern, and C. R. Ast 'Structural influence on the Rashba-type spin splitting in surface alloys', *Phys. Rev. B* **81**, 245430 (2010)

[29] I. Gierz, T. Suzuki, E. Frantzeskakis, S. Pons, S. Ostanin, A. Ernst, J. Henk, M. Grioni, K. Kern, and C. R. Ast 'Silicon surface with giant spin splitting', *Phys. Rev. Lett.* **103**, 046803 (2009)

[30] S. Datta and B. Das 'Electronic analog of the electro-optic modulator', *Applied Physics Letters* **56**, 665 (1990)

[31] C. L. Kane and E. J. Mele 'Quantum spin hall effect in graphene', *Phys. Rev. Lett.* **95**, 226801 (2005)

[32] B. A. Bernevig, T. L. Hughes, and S.-C. Zhang 'Quantum spin hall effect and topological phase transition in HgTe quantum wells', *Science* **314**, 1757 (2006)

[33] M. König, S. Wiedmann, C. Brüne, A. Roth, H. Buhmann, L. W. Molenkamp, X.-L. Qi, and S.-C. Zhang ‘Quantum spin hall insulator state in HgTe quantum wells’, *Science* **318**, 766 (2007)

[34] S. Chadov, X. Qi, J. Kübler, G. H. Fecher, C. Felser, and S. C. Zhang ‘Tunable multifunctional topological insulators in ternary Heusler compounds’, *Nat. Mater.* **9**, 541 (2010)

[35] L. Fu, C. L. Kane, and E. J. Mele ‘Topological insulators in three dimensions’, *Phys. Rev. Lett.* **98**, 106803 (2007)

[36] J. E. Moore and L. Balents ‘Topological invariants of time-reversal-invariant band structures’, *Phys. Rev. B* **75**, 121306 (2007)

[37] L. Fu and C. L. Kane ‘Topological insulators with inversion symmetry’, *Phys. Rev. B* **76**, 045302 (2007)

[38] D. Hsieh, D. Qian, L. Wray, Y. Xia, Y. S. Hor, R. J. Cava, and M. Z. Hasan ‘A topological Dirac insulator in a quantum spin hall phase’, *Nature* **452**, 970 (2008)

[39] H. Zhang, C.-X. Liu, X.-L. Qi, X. Dai, Z. Fang, and S.-C. Zhang ‘Topological insulators in Bi_2Se_3, Bi_2Te_3 and Sb_2Te_3 with a single Dirac cone on the surface’, *Nat. Phys.* **5**, 438 (2009)

[40] Y. Xia, D. Qian, D. Hsieh, L. Wray, A. Pal, H. Lin, A. Bansil, D. Grauer, Y. S. Hor, R. J. Cava, and M. Z. Hasan ‘Observation of a large-gap topological-insulator class with a single Dirac cone on the surface’, *Nat. Phys.* **5**, 398 (2009)

[41] Y. L. Chen, J. G. Analytis, J.-H. Chu, Z. K. Liu, S.-K. Mo, X. L. Qi, H. J. Zhang, D. H. Lu, X. Dai, Z. Fang, S. C. Zhang, I. R. Fisher, Z. Hussain, and Z.-X. Shen ‘Experimental realization of a three-dimensional topological insulator, Bi_2Te_3’, *Science* **325**, 178 (2009)

[42] M. König, H. Buhmann, L. W. Molenkamp, T. Hughes, C.-X. Liu, X.-L. Qi, and S.-C. Zhang ‘The quantum spin hall effect: Theory and experiment’, *J. Phys. Soc. Jpn.* **77**, 031007 (2008)

[43] C. L. Kane ‘Condensed matter: An insulator with a twist’, *Nat. Phys.* **4**, 348 (2008)

[44] S.-C. Zhang ‘Topological states of quantum matter’, *Physics* **1**, 6 (2008)

[45] J. E. Moore 'The birth of topological insulators', *Nature* **464**, 194 (2010)

[46] M. Z. Hasan and C. L. Kane 'Colloquium', *Rev. Mod. Phys.* **82**, 3045 (2010)

[47] M. Franz 'Topological insulators: Starting a new family', *Nat. Mater.* **9**, 536 (2010)

[48] X.-L. Qi and S.-C. Zhang 'Topological insulators and superconductors', *Rev. Mod. Phys.* **83**, 1057 (2011)

[49] Y. L. Chen, Z. K. Liu, J. G. Analytis, J.-H. Chu, H. J. Zhang, B. H. Yan, S.-K. Mo, R. G. Moore, D. H. Lu, I. R. Fisher, S. C. Zhang, Z. Hussain, and Z.-X. Shen 'Single Dirac cone topological surface state and unusual thermoelectric property of compounds from a new topological insulator family', *Phys. Rev. Lett.* **105**, 266401 (2010)

[50] T. Sato, K. Segawa, H. Guo, K. Sugawara, S. Souma, T. Takahashi, and Y. Ando 'Direct evidence for the Dirac-cone topological surface states in the ternary chalcogenide $TlBiSe_2$', *Phys. Rev. Lett.* **105**, 136802 (2010)

[51] Y. S. Hor, A. Richardella, P. Roushan, Y. Xia, J. G. Checkelsky, A. Yazdani, M. Z. Hasan, N. P. Ong, and R. J. Cava 'p-type Bi_2Se_3 for topological insulator and low-temperature thermoelectric applications', *Phys. Rev. B* **79**, 195208 (2009)

[52] J. G. Analytis, R. D. McDonald, S. C. Riggs, J.-H. Chu, G. S. Boebinger, and I. R. Fisher 'Two-dimensional surface state in the quantum limit of a topological insulator', *Nat. Phys.* **6**, 960 (2010)

[53] D. Kong, Y. Chen, J. J. Cha, Q. Zhang, J. G. Analytis, K. Lai, Z. Liu, S. S. Hong, K. J. Koski, S.-K. Mo, Z. Hussain, I. R. Fisher, Z.-X. Shen, and Y. Cui 'Ambipolar field effect in the ternary topological insulator $(Bi_xSb_{1-x})_2Te_3$ by composition tuning', *Nat. Nano.* **6**, 705 (2011)

[54] J. Zhang, C.-Z. Chang, Z. Zhang, J. Wen, X. Feng, K. Li, M. Liu, K. He, L. Wang, X. Chen, Q.-K. Xue, X. Ma, and Y. Wang 'Band structure engineering in $(Bi_{1-x}Sb_x)_2Te_3$ ternary topological insulators', *Nat. Commun.* **2**, 574 (2011)

[55] T. Arakane, T. Sato, S. Souma, K. Kosaka, K. Nakayama, M. Komatsu, T. Takahashi, Z. Ren, K. Segawa, and Y. Ando 'Tunable Dirac cone in the topological insulator $Bi_{2-x}Sb_xTe_{3-y}Se_y$', *Nat. Commun.* **3**, 636 (2012)

[56] J. G. Checkelsky, Y. S. Hor, R. J. Cava, and N. P. Ong 'Bulk band gap and surface state conduction observed in voltage-tuned crystals of the topological insulator Bi_2Se_3', *Phys. Rev. Lett.* **106**, 196801 (2011)

[57] H. Peng, K. Lai, D. Kong, S. Meister, Y. Chen, X.-L. Qi, S.-C. Zhang, Z.-X. Shen, and Y. Cui 'Aharonov-bohm interference in topological insulator nanoribbons', *Nat. Mater.* **9**, 225 (2010)

[58] X. Chen, X.-C. Ma, K. He, J.-F. Jia, and Q.-K. Xue 'Molecular beam epitaxial growth of topological insulators', *Advanced Materials* **23**, 1162 (2011)

[59] S. Das Sarma and Q. Li 'Many-body effects and possible superconductivity in the two-dimensional metallic surface states of three-dimensional topological insulators', *Phys. Rev. B* **88**, 081404 (2013)

[60] S. A. Wolf, D. D. Awschalom, R. A. Buhrman, J. M. Daughton, S. von MolnÃ¡r, M. L. Roukes, A. Y. Chtchelkanova, and D. M. Treger 'Spintronics: A spin-based electronics vision for the future', *Science* **294**, 1488 (2001)

[61] D. Hsieh, Y. Xia, L. Wray, D. Qian, A. Pal, J. H. Dil, J. Osterwalder, F. Meier, G. Bihlmayer, C. L. Kane, Y. S. Hor, R. J. Cava, and M. Z. Hasan 'Observation of unconventional quantum spin textures in topological insulators', *Science* **323**, 919 (2009)

[62] J. Linder, Y. Tanaka, T. Yokoyama, A. Sudbø, and N. Nagaosa 'Unconventional superconductivity on a topological insulator', *Phys. Rev. Lett.* **104**, 067001 (2010)

[63] C. R. Ast, G. Wittich, P. Wahl, R. Vogelgesang, D. Pacilé, M. C. Falub, L. Moreschini, M. Papagno, M. Grioni, and K. Kern 'Local detection of spin-orbit splitting by scanning tunneling spectroscopy', *Phys. Rev. B* **75**, 201401 (2007)

[64] C. R. Ast, J. Henk, A. Ernst, L. Moreschini, M. C. Falub, D. Pacilé, P. Bruno, K. Kern, and M. Grioni 'Giant spin splitting through surface alloying', *Phys. Rev. Lett.* **98**, 186807 (2007)

[65] L. Moreschini, A. Bendounan, I. Gierz, C. R. Ast, H. Mirhosseini, H. Höchst, K. Kern, J. Henk, A. Ernst, S. Ostanin, F. Reinert, and M. Grioni 'Assessing the atomic contribution to the rashba spin-orbit splitting in surface alloys: Sb/Ag(111)', *Phys. Rev. B* **79**, 075424 (2009)

[66] G. Bihlmayer, S. Blügel, and E. V. Chulkov 'Enhanced Rashba spin-orbit splitting in Bi/Ag(111) and Pb/Ag(111) surface alloys from first principles', *Phys. Rev. B* **75**, 195414 (2007)

[67] F. Meier, H. Dil, J. Lobo-Checa, L. Patthey, and J. Osterwalder 'Quantitative vectorial spin analysis in angle-resolved photoemission: Bi/Ag(111) and Pb/Ag(111)', *Phys. Rev. B* **77**, 165431 (2008)

[68] J. Premper, M. Trautmann, J. Henk, and P. Bruno 'Spin-orbit splitting in an anisotropic two-dimensional electron gas', *Phys. Rev. B* **76**, 073310 (2007)

[69] P. R. Wallace 'The band theory of graphite', *Phys. Rev.* **71**, 622 (1947)

[70] K. S. Novoselov, A. K. Geim, S. V. Morozov, D. Jiang, Y. Zhang, S. V. Dubonos, I. V. Grigorieva, and A. A. Firsov 'Electric field effect in atomically thin carbon films', *Science* **306**, 666 (2004)

[71] K. S. Novoselov, A. K. Geim, S. V. Morozov, D. Jiang, M. I. Katsnelson, I. V. Grigorieva, S. V. Dubonos, and A. A. Firsov 'Two-dimensional gas of massless Dirac fermions in graphene', *Nature* **438**, 197 (2005)

[72] Y. Zhang, Y.-W. Tan, H. L. Stormer, and P. Kim 'Experimental observation of the quantum hall effect and Berry's phase in graphene', *Nature* **438**, 201 (2005)

[73] A. K. Geim and K. S. Novoselov 'The rise of graphene', *Nat. Mater.* **6**, 183 (2007)

[74] P. Sharma, J. Gomez-Diaz, A. Ionescu, and J. Perruisseau-Carrier 'Determination of minimum conductivity of graphene from contactless microwaves measurements', In 'Nanotechnology (IEEE-NANO), 12th IEEE Conference on', pages 1–4 (2012)

[75] Y. Zhang, V. W. Brar, C. Girit, A. Zettl, and M. F. Crommie 'Origin of spatial charge inhomogeneity in graphene', *Nat. Phys.* **5**, 722 (2009)

[76] A. K. Geim 'Graphene: Status and prospects', *Science* **324**, 1530 (2009)

[77] C. McConville, D. Woodruff, and S. Kevan 'The electronic structure of graphitic overlayers on Ni(100)', *Surface Science* **171**, (1986)

[78] A. M. Shikin, G. V. Prudnikova, V. K. Adamchuk, F. Moresco, and K.-H. Rieder 'Surface intercalation of gold underneath a graphite monolayer on Ni(111) studied by

angle-resolved photoemission and high-resolution electron-energy-loss spectroscopy', *Phys. Rev. B* **62**, 13202 (2000)

[79] A. Varykhalov, J. Sánchez-Barriga, A. M. Shikin, C. Biswas, E. Vescovo, A. Rybkin, D. Marchenko, and O. Rader 'Electronic and magnetic properties of quasifreestanding graphene on Ni', *Phys. Rev. Lett.* **101**, 157601 (2008)

[80] A. B. Preobrajenski, M. L. Ng, A. S. Vinogradov, and N. Mårtensson 'Controlling graphene corrugation on lattice-mismatched substrates', *Phys. Rev. B* **78**, 073401 (2008)

[81] N. Kholin, E. Rut'kov, and A. Tontegode 'The nature of the adsorption bond between graphite islands and iridium surface', *Surface Science* **139**, 155 (1984)

[82] I. Pletikosić, M. Kralj, P. Pervan, R. Brako, J. Coraux, A. T. N'Diaye, C. Busse, and T. Michely 'Dirac cones and minigaps for graphene on Ir(111)', *Phys. Rev. Lett.* **102**, 056808 (2009)

[83] H. Zi-Pu, D. Ogletree, M. V. Hove, and G. Somorjai. 'Leed theory for incommensurate overlayers: Application to graphite on Pt(111)', *Surface Science* **180**, 433 (1987)

[84] M. Sasaki, Y. Yamada, Y. Ogiwara, S. Yagyu, and S. Yamamoto 'Moiré contrast in the local tunneling barrier height images of monolayer graphite on Pt(111)', *Phys. Rev. B* **61**, 15653 (2000)

[85] A. V. Bommel, J. Crombeen, and A. V. Tooren 'LEED and auger electron observations of the SiC(0001) surface', *Surface Science* **48**, 463 (1975)

[86] M. Orlita, C. Faugeras, P. Plochocka, P. Neugebauer, G. Martinez, D. K. Maude, A.-L. Barra, M. Sprinkle, C. Berger, W. A. de Heer, and M. Potemski 'Approaching the Dirac point in high-mobility multilayer epitaxial graphene', *Phys. Rev. Lett.* **101**, 267601 (2008)

[87] M. Sprinkle, D. Siegel, Y. Hu, J. Hicks, A. Tejeda, A. Taleb-Ibrahimi, P. Le Fèvre, F. Bertran, S. Vizzini, H. Enriquez, S. Chiang, P. Soukiassian, C. Berger, W. A. de Heer, A. Lanzara, and E. H. Conrad 'First direct observation of a nearly ideal graphene band structure', *Phys. Rev. Lett.* **103**, 226803 (2009)

[88] F. Varchon, R. Feng, J. Hass, X. Li, B. N. Nguyen, C. Naud, P. Mallet, J.-Y. Veuillen, C. Berger, E. H. Conrad, and L. Magaud 'Electronic structure of epitaxial graphene layers on SiC: Effect of the substrate', *Phys. Rev. Lett.* **99**, 126805 (2007)

[89] T. Seyller, A. Bostwick, K. V. Emtsev, K. Horn, L. Ley, J. L. McChesney, T. Ohta, J. D. Riley, E. Rotenberg, and F. Speck 'Epitaxial graphene: a new material', *Physica status solidi (b)* **245**, 1436 (2008)

[90] C. Berger, Z. Song, T. Li, X. Li, A. Y. Ogbazghi, R. Feng, Z. Dai, A. N. Marchenkov, E. H. Conrad, P. N. First, and W. A. de Heer 'Ultrathin epitaxial graphite: 2D electron gas properties and a route toward graphene-based nanoelectronics', *J. Phys. Chem. B* **108**, 19912 (2004)

[91] K. V. Emtsev, F. Speck, T. Seyller, L. Ley, and J. D. Riley 'Interaction, growth, and ordering of epitaxial graphene on SiC0001 surfaces: A comparative photoelectron spectroscopy study', *Phys. Rev. B* **77**, 155303 (2008)

[92] J. Jobst, D. Waldmann, F. Speck, R. Hirner, D. K. Maude, T. Seyller, and H. B. Weber 'Quantum oscillations and quantum hall effect in epitaxial graphene', *Phys. Rev. B* **81**, 195434 (2010)

[93] F. Owman, C. Hallin, P. Mårtensson, and E. Janzén 'Removal of polishing-induced damage from 6H-SiC(0001) substrates by hydrogen etching', *Journal of Crystal Growth* **167**, 391 (1996)

[94] V. Ramachandran, M. Brady, A. Smith, R. Feenstra, and D. Greve 'Preparation of atomically flat surfaces on silicon carbide using hydrogen etching', *Journal of Electronic Materials* **27**, 308 (1998)

[95] K. V. Emtsev, A. Bostwick, K. Horn, J. Jobst, G. L. Kellogg, L. Ley, J. L. McChesney, T. Ohta, S. A. Reshanov, J. Rohrl, E. Rotenberg, A. K. Schmid, D. Waldmann, H. B. Weber, and T. Seyller 'Towards wafer-size graphene layers by atmospheric pressure graphitization of silicon carbide', *Nat. Mater.* **8**, 203 (2009)

[96] C. Riedl, C. Coletti, and U. Starke 'Structural and electronic properties of epitaxial graphene on SiC(0 0 0 1): a review of growth, characterization, transfer doping and hydrogen intercalation', *Journal of Physics D: Applied Physics* **43**, 374009 (2010)

[97] C. Riedl, C. Coletti, T. Iwasaki, A. A. Zakharov, and U. Starke ‘Quasi-free-standing epitaxial graphene on SiC obtained by hydrogen intercalation’, *Phys. Rev. Lett.* **103**, 246804 (2009)

[98] A. Bostwick, T. Ohta, J. L. McChesney, K. V. Emtsev, T. Seyller, K. Horn, and E. Rotenberg ‘Symmetry breaking in few layer graphene films’, *New Journal of Physics* **9**, 385 (2007)

[99] C. Riedl, U. Starke, J. Bernhardt, M. Franke, and K. Heinz ‘Structural properties of the graphene-SiC(0001) interface as a key for the preparation of homogeneous large-terrace graphene surfaces’, *Phys. Rev. B* **76**, 245406 (2007)

[100] P. Mallet, F. Varchon, C. Naud, L. Magaud, C. Berger, and J.-Y. Veuillen ‘Electron states of mono- and bilayer graphene on SiC probed by scanning-tunneling microscopy’, *Phys. Rev. B* **76**, 041403 (2007)

[101] A. Bostwick, T. Ohta, T. Seyller, K. Horn, and E. Rotenberg ‘Quasiparticle dynamics in graphene’, *Nat. Phys.* **3**, 36 (2007)

[102] T. Ohta, A. Bostwick, T. Seyller, K. Horn, and E. Rotenberg ‘Controlling the electronic structure of bilayer graphene’, *Science* **313**, 951 (2006)

[103] S. Y. Zhou, G.-H. Gweon, A. V. Fedorov, P. N. First, W. A. de Heer, D.-H. Lee, F. Guinea, A. H. Castro Neto, and A. Lanzara ‘Substrate-induced bandgap opening in epitaxial graphene’, *Nat. Mater.* **6**, 770 (2007)

[104] J. A. Robinson, M. Wetherington, J. L. Tedesco, P. M. Campbell, X. Weng, J. Stitt, M. A. Fanton, E. Frantz, D. Snyder, B. L. VanMil, G. G. Jernigan, R. L. Myers-Ward, C. R. Eddy, and D. K. Gaskill ‘Correlating Raman spectral signatures with carrier mobility in epitaxial graphene: A guide to achieving high mobility on the wafer scale’, *Nano Letters* **9**, 2873 (2009)

[105] H. Hertz ‘Über einen Einfluss des ultravioletten Lichtes auf die electrische Entladung’, *Annalen der Physik* **267**, 983 (1887)

[106] A. Einstein ‘Über einen die Erzeugung und Verwandlung des Lichtes betreffenden heuristischen Gesichtspunkt’, *Annalen der Physik* **322**, 132 (1905)

[107] S. Hüfner *Photoelectron Spectroscopy - Principles and Applications*, Springer Berlin (2003)

[108] M. P. Seah and W. A. Dench 'Quantitative electron spectroscopy of surfaces: A standard data base for electron inelastic mean free paths in solids', *Surface and Interface Analysis* **1**, 2 (1979)

[109] C. N. Berglund and W. E. Spicer 'Photoemission studies of copper and silver: Theory', *Phys. Rev.* **136**, A1030 (1964)

[110] F. Reinert 'Spin-orbit interaction in the photoemission spectra of noble metal surface states'. *Journal of Physics: Condensed Matter* **15**, S693 (2003)

[111] P. B. Allen 'Electron-phonon effects in the infrared properties of metals', *Phys. Rev. B* **3**, 305 (1971)

[112] S. Tougaard 'Quantitative analysis of the inelastic background in surface electron spectroscopy', *Surface and Interface Analysis* **11**, 453 (1988)

[113] Moulder *Handbook of X-ray Photoelectron Spectroscopy*, Physical Electronics (Inc. Minnesota USA) (1995)

[114] D. Hsieh, Y. Xia, D. Qian, L. Wray, J. H. Dil, F. Meier, J. Osterwalder, L. Patthey, J. G. Checkelsky, N. P. Ong, A. V. Fedorov, H. Lin, A. Bansil, D. Grauer, Y. S. Hor, R. J. Cava, and M. Z. Hasan 'A tunable topological insulator in the spin helical Dirac transport regime', *Nature* **460**, 1101 (2009)

[115] B. Sacepe, J. B. Oostinga, J. Li, A. Ubaldini, N. J. Couto, E. Giannini, and A. F. Morpurgo 'Gate-tuned normal and superconducting transport at the surface of a topological insulator', *Nat. Commun.* **2**, 575 (2011)

[116] F. Xiu, L. He, Y. Wang, L. Cheng, L.-T. Chang, M. Lang, G. Huang, X. Kou, Y. Zhou, X. Jiang, Z. Chen, J. Zou, A. Shailos, and K. L. Wang 'Manipulating surface states in topological insulator nanoribbons', *Nat. Nano.* **6**, 216 (2011)

[117] J. Chen, H. J. Qin, F. Yang, J. Liu, T. Guan, F. M. Qu, G. H. Zhang, J. R. Shi, X. C. Xie, C. L. Yang, K. H. Wu, Y. Q. Li, and L. Lu 'Gate-voltage control of chemical potential and weak antilocalization in Bi_2Se_3', *Phys. Rev. Lett.* **105**, 176602 (2010)

[118] D. Kong, W. Dang, J. J. Cha, H. Li, S. Meister, H. Peng, Z. Liu, and Y. Cui 'Few-layer nanoplates of Bi_2Se_3 and Bi_2Te_3 with highly tunable chemical potential', *Nano Letters* **10**, 2245 (2010)

[119] Z. Ren, A. A. Taskin, S. Sasaki, K. Segawa, and Y. Ando 'Large bulk resistivity and surface quantum oscillations in the topological insulator Bi_2Te_2Se', *Phys. Rev. B* **82**, 241306 (2010)

[120] J. Wang, A. M. DaSilva, C.-Z. Chang, K. He, J. K. Jain, N. Samarth, X.-C. Ma, Q.-K. Xue, and M. H. W. Chan 'Evidence for electron-electron interaction in topological insulator thin films', *Phys. Rev. B* **83**, 245438 (2011)

[121] Y. Takagaki, B. Jenichen, U. Jahn, M. Ramsteiner, and K.-J. Friedland 'Weak antilocalization and electron-electron interaction effects in Cu-doped Bi_2Se_3 films', *Phys. Rev. B* **85**, 115314 (2012)

[122] H. K. Pal, V. I. Yudson, and D. L. Maslov 'Effect of electron-electron interaction on surface transport in the Bi_2Te_3 family of three-dimensional topological insulators', *Phys. Rev. B* **85**, 085439 (2012)

[123] P. M. Ostrovsky, I. V. Gornyi, and A. D. Mirlin 'Interaction-induced criticality in $\mathbb{Z}_2$ topological insulators', *Phys. Rev. Lett.* **105**, 036803 (2010)

[124] L. A. Wray, S.-Y. Xu, Y. Xia, D. Hsieh, A. V. Fedorov, Y. S. Hor, R. J. Cava, A. Bansil, H. Lin, and M. Z. Hasan 'A topological insulator surface under strong coulomb, magnetic and disorder perturbations', *Nat. Phys.* **7**, 32 (2011)

[125] M. Hohenadler and F. F. Assaad 'Correlation effects in two-dimensional topological insulators', *Journal of Physics: Condensed Matter* **25**, 143201 (2013)

[126] J. Xiong, A. Petersen, D. Qu, Y. Hor, R. Cava, and N. Ong 'Quantum oscillations in a topological insulator Bi_2Te_2Se with large bulk resistivity', *Physica E: Low-dimensional Systems and Nanostructures* **44**, 917 (2012)

[127] H. M. Benia, C. Lin, K. Kern, and C. R. Ast 'Reactive chemical doping of the Bi_2Se_3 topological insulator', *Phys. Rev. Lett.* **107**, 177602 (2011)

[128] M. Bianchi, R. C. Hatch, D. Guan, T. Planke, J. Mi, B. B. Iversen, and P. Hofmann 'The electronic structure of clean and adsorbate-covered Bi_2Se_3: an angle-resolved photoemission study', *Semiconductor Science and Technology* **27**, 124001 (2012)

[129] R. C. Hatch, M. Bianchi, D. Guan, S. Bao, J. Mi, B. B. Iversen, L. Nilsson, L. Hornekær, and P. Hofmann 'Stability of the $Bi_2Se_3(111)$ topological state: Electron-phonon and electron-defect scattering', *Phys. Rev. B* **83**, 241303 (2011)

[130] M. Hengsberger, R. Frésard, D. Purdie, P. Segovia, and Y. Baer ‘Electron-phonon coupling in photoemission spectra’, *Phys. Rev. B* **60**, 10796 (1999)

[131] A. A. Kordyuk, S. V. Borisenko, A. Koitzsch, J. Fink, M. Knupfer, and H. Berger ‘Bare electron dispersion from experiment: Self-consistent self-energy analysis of photoemission data’, *Phys. Rev. B* **71**, 214513 (2005)

[132] K. Yang, W. Setyawan, S. Wang, M. Buongiorno Nardelli, and S. Curtarolo ‘A search model for topological insulators with high-throughput robustness descriptors’, *Nat. Mater.* **11**, 614 (2012)

[133] Z. Zhu, Y. Cheng, and U. Schwingenschlögl ‘Topological phase diagrams of bulk and monolayer $TiS_{2-x}Te_x$’, *Phys. Rev. Lett.* **110**, 077202 (2013)

[134] S.-Y. Xu ‘Discovery of several large families of topological insulator classes with backscattering-suppressed spin-polarized single-Dirac-cone on the surface’ arXiv:1007.5111v1 (2010)

[135] J. Wilson and A. Yoffe ‘The transition metal dichalcogenides discussion and interpretation of the observed optical, electrical and structural properties’, *Advances in Physics* **18**, 193 (1969)

[136] R. Friend and A. Yoffe ‘Electronic properties of intercalation complexes of the transition metal dichalcogenides’, *Advances in Physics* **36**, 1 (1987)

[137] A. H. Castro Neto ‘Charge density wave, superconductivity, and anomalous metallic behavior in 2D transition metal dichalcogenides’, *Phys. Rev. Lett.* **86**, 4382 (2001)

[138] Y. Arnaud and M. Chevreton ‘Etude comparative des composÃ©s TiX_2 (X = S, Se, Te). structures de $TiTe_2$ et TiSeTe’, *Journal of Solid State Chemistry* **39**, 230 (1981)

[139] A. Shkvarin, Y. Yarmoshenko, N. Skorikov, M. Yablonskikh, A. Merentsov, E. Shkvarina, and A. Titov ‘Electronic structure of titanium dichalcogenides TiX_2 (X = S, Se, Te)’, *Journal of Experimental and Theoretical Physics* **114**, 150 (2012)

[140] Y.-W. Z. Hongliang Shi, Hui Pan and B. I. Yakobson ‘Quasiparticle band structures and optical properties of strained monolayer MoS_2 and WS_2’, *Phys. Rev. B* **87**, 155304 (2013)

[141] L. Shao, G. Chen, H. Ye, Y. Wu, H. Niu, and Y. Zhu 'Theoretical study on electronic properties of MoS_2 antidot lattices', *Journal of Applied Physics* **116**, 113704 (2014)

[142] A. K. Geim and I. V. Grigorieva 'Van der waals heterostructures', *Nature* **499**, 419 (2013)

[143] D. Kong and Y. Cui 'Opportunities in chemistry and materials science for topological insulators and their nanostructures', *Nat. Chem.* **3**, 845 (2011)

[144] M. Chhowalla, H. S. Shin, G. Eda, L.-J. Li, K. P. Loh, and H. Zhang 'The chemistry of two-dimensional layered transition metal dichalcogenide nanosheets', *Nat. Chem.* **5**, 263 (2013)

[145] H. L. Zhuang and R. G. Hennig 'Computational search for single-layer transition-metal dichalcogenide photocatalysts', *The Journal of Physical Chemistry C* **117**, 20440 (2013)

[146] D. Jariwala, V. K. Sangwan, L. J. Lauhon, T. J. Marks, and M. C. Hersam 'Emerging device applications for semiconducting two-dimensional transition metal dichalcogenides', *ACS Nano* **8**, 1102 (2014)

[147] Q. H. Wang, K. Kalantar-Zadeh, A. Kis, J. N. Coleman, and M. S. Strano 'Electronics and optoelectronics of two-dimensional transition metal dichalcogenides', *Nat. Nano.* **7**, 699 (2012)

[148] H. Pan 'Metal dichalcogenides monolayers: Novel catalysts for electrochemical hydrogen production', *Sci. Rep.* **4**, 5348 (2014)

[149] E. Gourmelon, O. Lignier, H. Hadouda, G. Couturier, J. Bernede, J. Tedd, J. Pouzet, and J. Salardenne 'MS_2 (M= W, Mo) photosensitive thin films for solar cells', *Solar Energy Materials and Solar Cells* **46**, 115 (1997)

[150] T. Cao, G. Wang, W. Han, H. Ye, C. Zhu, J. Shi, Q. Niu, P. Tan, E. Wang, B. Liu, and J. Feng 'Valley-selective circular dichroism of monolayer molybdenum disulphide', *Nat. Commun.* **3**, 887 (2012)

[151] K. F. Mak, K. He, J. Shan, and T. F. Heinz 'Control of valley polarization in monolayer MoS_2 by optical helicity', *Nat. Nano.* **7**, 494 (2012)

[152] W. Chen, S. Chen, D. C. Qi, X. Y. Gao, and A. T. S. Wee 'Surface transfer p-type doping of epitaxial graphene', *Journal of the American Chemical Society* **129**, 10418 (2007)

[153] C. Coletti, C. Riedl, D. S. Lee, B. Krauss, L. Patthey, K. von Klitzing, J. H. Smet, and U. Starke 'Charge neutrality and band-gap tuning of epitaxial graphene on SiC by molecular doping', *Phys. Rev. B* **81**, 235401 (2010)

[154] I. Gierz, C. Riedl, U. Starke, C. R. Ast, and K. Kern 'Atomic hole doping of graphene', *Nano Letters* **8**, 4603 (2008)

[155] K. Pi, K. M. McCreary, W. Bao, W. Han, Y. F. Chiang, Y. Li, S.-W. Tsai, C. N. Lau, and R. K. Kawakami 'Electronic doping and scattering by transition metals on graphene', *Phys. Rev. B* **80**, 075406 (2009)

[156] T. O. Wehling, K. S. Novoselov, S. V. Morozov, E. E. Vdovin, M. I. Katsnelson, A. K. Geim, and A. I. Lichtenstein 'Molecular doping of graphene', *Nano Letters* **8**, 173 (2008)

[157] D. A. Siegel, C.-H. Park, C. Hwang, J. Deslippe, A. V. Fedorov, S. G. Louie, and A. Lanzara 'Many-body interactions in quasi-freestanding graphene', *Proceedings of the National Academy of Sciences* **108**, 11365 (2011)

[158] J. L. McChesney, A. Bostwick, T. Ohta, T. Seyller, K. Horn, J. González, and E. Rotenberg 'Extended van Hove singularity and superconducting instability in doped graphene', *Phys. Rev. Lett.* **104**, 136803 (2010)

[159] A. Bostwick, J. L. McChesney, K. V. Emtsev, T. Seyller, K. Horn, S. D. Kevan, and E. Rotenberg 'Quasiparticle transformation during a metal-insulator transition in graphene', *Phys. Rev. Lett.* **103**, 056404 (2009)

[160] G. Schubert and H. Fehske 'Metal-to-insulator transition and electron-hole puddle formation in disordered graphene nanoribbons', *Phys. Rev. Lett.* **108**, 066402 (2012)

[161] G. Profeta, M. Calandra, and F. Mauri 'Phonon-mediated superconductivity in graphene by lithium deposition', *Nat. Phys.* **8**, 131 (2012)

[162] C. Weeks, J. Hu, J. Alicea, M. Franz, and R. Wu 'Engineering a robust quantum spin hall state in graphene via adatom deposition', *Phys. Rev. X* **1**, 021001 (2011)

[163] N. M. R. Peres 'The transport properties of graphene: An introduction', *Rev. Mod. Phys.* **82**, 2673 (2010)

[164] H. Medina, Y.-C. Lin, D. Obergfell, and P.-W. Chiu 'Tuning of charge densities in graphene by molecule doping', *Advanced Functional Materials* **21**, 2687 (2011)

[165] F. Schedin, A. K. Geim, S. V. Morozov, E. W. Hill, P. Blake, M. I. Katsnelson, and K. S. Novoselov 'Detection of individual gas molecules adsorbed on graphene', *Nat. Mater.* **6**, 652 (2007)

[166] D. A. Siegel, W. Regan, A. V. Fedorov, A. Zettl, and A. Lanzara 'Charge carrier screening in single layer graphene', *Phys. Rev. Lett.* **110**, 146802 (2013)

[167] T. Wehling, M. Katsnelson, and A. Lichtenstein 'Adsorbates on graphene: Impurity states and electron scattering', *Chem. Phys. Lett.* **476**, 125 (2009)

[168] K. Nakada and A. Ishii 'Migration of adatom adsorption on graphene using DFT calculation', *Solid State Communications* **151**, 13 (2011)

[169] J.-H. Chen, C. Jang, S. Adam, M. S. Fuhrer, E. D. Williams, and M. Ishigami 'Charged-impurity scattering in graphene', *Nat. Phys.* **4**, 377 (2008)

[170] F. de Juan, E. H. Hwang, and M. A. H. Vozmediano 'Spectral and optical properties of doped graphene with charged impurities in the self-consistent born approximation', *Phys. Rev. B* **82**, 245418 (2010)

[171] E. H. Hwang and S. Das Sarma 'Single-particle relaxation time versus transport scattering time in a two-dimensional graphene layer', *Phys. Rev. B* **77**, 195412 (2008)

[172] A. L. Walter, A. Bostwick, K.-J. Jeon, F. Speck, M. Ostler, T. Seyller, L. Moreschini, Y. J. Chang, M. Polini, R. Asgari, A. H. MacDonald, K. Horn, and E. Rotenberg 'Effective screening and the plasmaron bands in graphene', *Phys. Rev. B* **84**, 085410 (2011)

[173] T. Horiguchi 'Lattice green's functions for the triangular and honeycomb lattices', *J. Math. Phys.* **13**, 1411 (1972)

[174] J. Lischner, D. Vigil-Fowler, and S. G. Louie ‘Physical origin of satellites in photoemission of doped graphene: An ab initio GW plus cumulant study’, *Phys. Rev. Lett.* **110**, 146801 (2013)

[175] C. Hwang, D. A. Siegel, S.-K. Mo, W. Regan, A. Ismach, Y. Zhang, A. Zettl, and A. Lanzara ‘Fermi velocity engineering in graphene by substrate modification’, *Sci. Rep.* **2**, 590 (2012)

[176] J. P. Robinson, H. Schomerus, L. Oroszlány, and V. I. Fal’ko ‘Adsorbate-limited conductivity of graphene’, *Phys. Rev. Lett.* **101**, 196803 (2008)

[177] P. A. Wolff ‘Localized moments in metals’, *Phys. Rev.* **124**, 1030 (1961)

[178] A. M. Clogston, B. T. Matthias, M. Peter, H. J. Williams, E. Corenzwit, and R. C. Sherwood ‘Local magnetic moment associated with an iron atom dissolved in various transition metal alloys’, *Phys. Rev.* **125**, 541 (1962)

[179] B. Velický, S. Kirkpatrick, and H. Ehrenreich ‘Single-site approximations in the electronic theory of simple binary alloys’, *Phys. Rev.* **175**, 747 (1968)

[180] J. Zhenzhao ‘Absence of a transport signature of spin-orbit coupling in graphene with indium adatoms’, arXiv:1409.8090 (2014)

[181] Y.-W. Tan, Y. Zhang, K. Bolotin, Y. Zhao, S. Adam, E. H. Hwang, S. Das Sarma, H. L. Stormer, and P. Kim ‘Measurement of scattering rate and minimum conductivity in graphene’, *Phys. Rev. Lett.* **99**, 246803 (2007)

[182] S. Das Sarma, S. Adam, E. H. Hwang, and E. Rossi ‘Electronic transport in two-dimensional graphene’, *Rev. Mod. Phys.* **83**, 407 (2011)

[183] M. I. Katsnelson *Graphene: Carbon in Two Dimensions*, Cambridge University Press (2012)

[184] E. Hwang, S. Adam, and S. Das Sarma ‘Carrier transport in two-dimensional graphene layers’, *Phys. Rev. Lett.* **98**, 186806 (2007)

[185] K. Nomura and MacDonald ‘Quantum transport of massless Dirac fermions’, *Phys. Rev. Lett.* **98**, 076602 (2007)

[186] Y. H. Wang, D. Hsieh, D. Pilon, L. Fu, D. R. Gardner, Y. S. Lee, and N. Gedik. 'Observation of a warped helical spin texture in Bi_2Se_3 from circular dichroism angle-resolved photoemission spectroscopy', *Phys. Rev. Lett.* **107**, 207602 (2011)

[187] G. Bian, L. Zhang, Y. Liu, T. Miller, and T.-C. Chiang 'Illuminating the surface spin texture of the giant-Rashba quantum-well system Bi/Ag(111) by circularly polarized photoemission', *Phys. Rev. Lett.* **108**, 186403 (2012)

[188] Y. Wang and N. Gedik 'Circular dichroism in angle-resolved photoemission spectroscopy of topological insulators', *physica status solidi (RRL) Rapid Research Letters* **7**, 64 (2013)

[189] J. Sánchez-Barriga, A. Varykhalov, J. Braun, S.-Y. Xu, N. Alidoust, O. Kornilov, J. Minár, K. Hummer, G. Springholz, G. Bauer, R. Schumann, L. V. Yashina, H. Ebert, M. Z. Hasan, and O. Rader 'Photoemission of Bi_2Se_3 with circularly polarized light: Probe of spin polarization or means for spin manipulation?', *Phys. Rev. X* **4**, 011046 (2014)

[190] W. Jung, Y. Kim, B. Kim, Y. Koh, C. Kim, M. Matsunami, S.-i. Kimura, M. Arita, K. Shimada, J. H. Han, J. Kim, B. Cho, and C. Kim 'Warping effects in the band and angular-momentum structures of the topological insulator Bi_2Te_3', *Phys. Rev. B* **84**, 245435 (2011)

[191] S. R. Park, J. Han, C. Kim, Y. Y. Koh, C. Kim, H. Lee, H. J. Choi, J. H. Han, K. D. Lee, N. J. Hur, M. Arita, K. Shimada, H. Namatame, and M. Taniguchi 'Chiral orbital-angular momentum in the surface states of Bi_2Se_3', *Phys. Rev. Lett.* **108**, 046805 (2012)

[192] H. Mirhosseini and J. Henk 'Spin texture and circular dichroism in photoelectron spectroscopy from the topological insulator Bi_2Te_3: First-principles photoemission calculations', *Phys. Rev. Lett.* **109**, 036803 (2012)

[193] G. Schönhense 'Circular dichroism and spin polarization in photoemission from adsorbates and non-magnetic solids', *Physica Scripta* **1990**, 255 (1990)

[194] I. Gierz, M. Lindroos, H. Höchst, C. R. Ast, and K. Kern 'Graphene sublattice symmetry and isospin determined by circular dichroism in angle-resolved photoemission spectroscopy', *Nano Letters* **12**, 3900 (2012)

[195] M. R. Scholz, J. Sánchez-Barriga, J. Braun, D. Marchenko, A. Varykhalov, M. Lindroos, Y. J. Wang, H. Lin, A. Bansil, J. Minár, H. Ebert, A. Volykhov, L. V. Yashina, and O. Rader 'Reversal of the circular dichroism in angle-resolved photoemission from Bi_2Te_3', *Phys. Rev. Lett.* **110**, 216801 (2013)

[196] J.-H. Park, C. H. Kim, J.-W. Rhim, and J. H. Han 'Orbital rashba effect and its detection by circular dichroism angle-resolved photoemission spectroscopy', *Phys. Rev. B* **85**, 195401 (2012)

[197] V. Arpiainen, V. Zalobotnyy, A. A. Kordyuk, S. V. Borisenko, and M. Lindroos 'Angular dependence of circular dichroism in Pb-doped and pristine', *Phys. Rev. B* **77**, 024520 (2008)

[198] B. Kim, C. H. Kim, P. Kim, W. Jung, Y. Kim, Y. Koh, M. Arita, K. Shimada, H. Namatame, M. Taniguchi, J. Yu, and C. Kim 'Spin and orbital angular momentum structure of Cu(111) and Au(111) surface states', *Phys. Rev. B* **85**, 195402 (2012)

[199] C. Jozwiak, C.-H. Park, K. Gotlieb, C. Hwang, D.-H. Lee, S. G. Louie, J. D. Denlinger, C. R. Rotundu, R. J. Birgeneau, Z. Hussain, and A. Lanzara 'Photoelectron spin-flipping and texture manipulation in a topological insulator', *Nat. Phys.* **9**, 293 (2013)

[200] D.-H. Lee 'Surface states of topological insulators: The Dirac fermion in curved two-dimensional spaces', *Phys. Rev. Lett.* **103**, 196804 (2009)

[201] H.-Z. Lu, J. Shi, and S.-Q. Shen 'Competition between weak localization and antilocalization in topological surface states', *Phys. Rev. Lett.* **107**, 076801 (2011)

[202] A. P. Schnyder, S. Ryu, A. Furusaki, and A. W. W. Ludwig 'Classification of topological insulators and superconductors in three spatial dimensions', *Phys. Rev. B* **78**, 195125 (2008)

[203] M. Polini, R. Asgari, G. Borghi, Y. Barlas, T. Pereg-Barnea, and A. H. MacDonald 'Plasmons and the spectral function of graphene', *Phys. Rev. B* **77**, 081411 (2008)

[204] S. R. Park, W. S. Jung, C. Kim, D. J. Song, C. Kim, S. Kimura, K. D. Lee, and N. Hur 'Quasiparticle scattering and the protected nature of the topological states in a parent topological insulator Bi_2Se_3', *Phys. Rev. B* **81**, 041405 (2010)

[205] W. Y. Liu MinHao 'Electron interaction and localization in ultrathin topological insulator films', *Science China Physics, Mechanics and Astronomy* **55**, 2213 (2012)

[206] H.-C. Liu, H.-Z. Lu, H.-T. He, B. Li, S.-G. Liu, Q. L. He, G. Wang, I. K. Sou, S.-Q. Shen, and J. Wang 'Tunable interaction-induced localization of surface electrons in antidot nanostructured Bi_2Te_3 thin films', *ACS Nano* **8**, 9616 (2014)

[207] C. Nayak, S. H. Simon, A. Stern, M. Freedman, and S. Das Sarma 'Non-abelian anyons and topological quantum computation', *Rev. Mod. Phys.* **80**, 1083 (2008)

[208] S. Raghu, S. B. Chung, X.-L. Qi, and S.-C. Zhang 'Collective modes of a helical liquid', *Phys. Rev. Lett.* **104**, 116401 (2010)

[209] J. W. McIver and D. Hsieh and H. Steinberg and P. Jarillo-Herrero and N. Gedik 'Control over topological insulator photocurrents with light polarization', *Nat. Nano.* **7**, 96 (2012)

[210] C.-H. Park and S. G. Louie. 'Spin polarization of photoelectrons from topological insulators', *Phys. Rev. Lett.* **109**, 097601 (2012)

[211] C. R. Ast, D. Pacilé, L. Moreschini, M. C. Falub, M. Papagno, K. Kern, M. Grioni, J. Henk, A. Ernst, S. Ostanin, and P. Bruno 'Spin-orbit split two-dimensional electron gas with tunable Rashba and Fermi energy' *Phys. Rev. B* **77**, 081407 (2008)

[212] R. Balog, B. Jorgensen, L. Nilsson, M. Andersen, E. Rienks, M. Bianchi, M. Fanetti, E. Laegsgaard, A. Baraldi, S. Lizzit, Z. Sljivancanin, F. Besenbacher, B. Hammer, T. G. Pedersen, P. Hofmann, and L. Hornekaer 'Bandgap opening in graphene induced by patterned hydrogen adsorption', *Nat. Mater.* **9**, 315 (2010)

[213] Y.-C. Chen, D. G. de Oteyza, Z. Pedramrazi, C. Chen, F. R. Fischer, and M. F. Crommie 'Tuning the band gap of graphene nanoribbons synthesized from molecular precursors', *ACS Nano* **7**, 6123 (2013)

[214] C. R. Woods, L. Britnell, A. Eckmann, R. S. Ma, J. C. Lu, H. M. Guo, X. Lin, G. L. Yu, Y. Cao, R. V. Gorbachev, A. V. Kretinin, J. Park, L. A. Ponomarenko, M. I. Katsnelson, Y. N. Gornostyrev, K. Watanabe, T. Taniguchi, C. Casiraghi, H.-J. Gao, A. K. Geim, and K. S. Novoselov 'Commensurate-incommensurate transition in graphene on hexagonal boron nitride', *Nat. Phys.* **10**, 451 (2014)

[215] H. Vita, S. Bottcher, K. Horn, E. N. Voloshina, R. E. Ovcharenko, T. Kampen, A. Thissen, and Y. S. Dedkov 'Understanding the origin of band gap formation in graphene on metals: graphene on Cu/Ir(111)', *Sci. Rep.* **4**, 5704 (2014)

[216] J. Hu, J. Alicea, R. Wu, and M. Franz 'Giant topological insulator gap in graphene with $5d$ adatoms', *Phys. Rev. Lett.* **109**, 266801 (2012)

[217] M. Zhao, W. Dong, and A. Wang 'Two-dimensional carbon topological insulators superior to graphene', *Sci. Rep.* **3**, 3532 (2013)

[218] H. B. Heersche, P. Jarillo-Herrero, J. B. Oostinga, L. M. K. Vandersypen, and A. F. Morpurgo 'Bipolar supercurrent in graphene', *Nature* **446**, 56 (2007)

[219] C. Ojeda-Aristizabal, M. Ferrier, S. Guéron, and H. Bouchiat 'Tuning the proximity effect in a superconductor-graphene-superconductor junction', *Phys. Rev. B* **79**, 165436 (2009)

[220] D. Jeong, J.-H. Choi, G.-H. Lee, S. Jo, Y.-J. Doh, and H.-J. Lee 'Observation of supercurrent in PbIn-graphene-PbIn josephson junction', *Phys. Rev. B* **83**, 094503 (2011)

Curriculum Vitae

Name

Name	Carola Straßer
Date of Birth	March 11, 1987
Place of Birth	Lauingen an der Donau, Germany
Nationality	German

School Education

1993-1997	Volksschule Wittislingen, Germany
1997-2006	St. Bonaventura Gymnasium in Dillingen an der Donau, Germany

University Education

2006-2011	Studies of FOKUS Physics at the Julius-Maximilians-Universität Würzburg, Germany
2009	Bachelor of Science
2011	Master of Science with Honors

Professional Experience

2009-2011	Master thesis 'Low-dimensional electron systems on semiconducting and metallic substrates' in the Group of Prof. Klaus Kern at the Max Planck Institute for Solid State Research in Stuttgart, Germany
2011-2015	PhD Student in the Group of Prof. Klaus Kern at the Max Planck Institute for Solid State Research in Stuttgart, Germany Topic: 'Investigation of interactions in two-dimensional electron gases with angular resolved photoemission spectroscopy'
2012	Research project on Tl adatoms on a monolayer of epitaxial graphene for three months at the University of British Columbia in Vancouver in the group of Prof. Andrea Damascelli

Publications

1. M. Assig, A. Koch, W. Stiepany, C. Straßer, A. Ast, K. Kern, and C. R. Ast
   'Miniature active damping stage for scanning probe applications in ultra high vacuum'
   Rev. Sci. Instrum. **83**, 033701 (2012)

2. M. Morgenstern, A. Georgi, C. Straßer, C. R. Ast, S. Becker, and M. Liebmann
   'Scanning tunneling microscopy of two-dimensional semiconductors: Spin properties and disorder'
   Physica E: Low-dimensional Systems and Nanostructures **44**, 1795 (2012)

3. C. Straßer, B. M. Ludbrook, G. Levy, A. J. Macdonald, S. A. Burke, T. O. Wehling, K. Kern, A. Damascelli, and C. R. Ast
   'Long-range versus short-range scattering in doped epitaxial graphene'
   (submitted)

4. B. M. Ludbrook, G. Levy, M. Zonno, M. Schneider, D. J. Dvorak, C. N. Veenstra, S. Zhdanovich, D. Wong, P. Dosanjh, C. Straßer, A. Stöhr, S. Forti, C. R. Ast, U. Starke, and A. Damascelli
   'Evidence for superconductivity in Li-decorated graphene'
   (submitted)

5. H. M. Benia, C. Straßer, K. Kern, and C. R. Ast
   'The surface band structure of $Bi_{1-x}Sb_x(111)$'
   (submitted)

6. C. Straßer, I. Gierz, H. M. Benia, K. Kern, and C. R. Ast
   'Photon-energy dependence of circular dichroism in the measured band structure of surface alloys'
   (in preparation)

Acknowledgements – Danksagungen

Zum Erfolg dieser Arbeit haben viele Leute beigetragen. Deshalb möchte ich mich bedanken bei

Prof. Klaus Kern, der mir die Möglichkeit gegeben hat als Doktorandin in seiner Abteilung am Max-Planck-Institut für Festkörperforschung zu arbeiten und die verschiedenen Forschungsprojekte durchzuführen. Er hat stets dafür gesorgt, dass alle notwendigen Rahmenbedingungen bestens erfüllt waren.

Dr. Christian Ast für die direkte Betreuung meiner Arbeit, die unzähligen Ratschläge und vielen fruchtbaren Diskussionen, für seine unglaubliche Begeisterung für die Wissenschaft und für sein offenes Ohr. Ein großes Dankeschön auch für die sorgfältigen Korrekturen und hilfreichen Anmerkungen zu dieser Arbeit.

Prof. Andrea Damascelli for the opportunity to work for three months in his ARPES lab in Vancouver, for his scientific support and for the successful collaboration within the scope of the MPI-UBC center.

Bart Ludbrook and **Giorgio Levy** for introducing me to the ARPES machine at UBC, for the friendly and pleasant working atmosphere and for their technical assistance.

Prof. Sarah Burke and her student **Andrew Macdonald** for the STM measurements on Tl decorated graphene.

Dr. Ulrich Starke, **Dr. Stiven Forti**, **Alexander Stöhr** und **Axel Köhler** für die vielen hochqualitativen Graphen-Proben und die nette und freundliche Atmosphäre bei der Arbeit im 7B15 Labor.

Tolga Acartürk und **Arthur Küster** für ihre stete und schnelle Hilfe bei allen technischen Problemen und Fragen im Labor.

Dr. Alexander Kuhn for growing the $TiTe_{1.5}Se_{0.5}$ samples and **Dr. Chandra Shekhar** for the Bi_2Te_2Se crystals.

Dr. Thomas White for painstakingly proofreading this thesis and for always making me smile when meeting him in the 6C floor.

Dr. Isabella Gierz dafür, dass sie mich als ihre Nachfolgerin perfekt eingelernt und mir gezeigt hat, wie man organisiert und wissenschaftlich präzise im Labor arbeitet. Danke auch für die schöne Zeit in Stuttgart.

Dr. Hadj Benia für die ausführliche und geduldige Einweisung im Labor und die zahlreichen Diskussionen.

Dr. Sören Krotzky für seine unglaubliche Hilfsbereitschaft und sein offenes Ohr zu jeder Zeit sowohl bei physikalischen oder technischen als auch privaten Angelegenheiten.

Dr. Tobias Herden für seine freundliche Unterstützung und seine korrekte und äußerst zuverlässige Art. Vielen Dank für die Unmengen an selbstgebackenen Kuchen!

meinen lieben Bürokollegen **Dr. Maximilian Assig**, **Dr. Steffen Kahle**, **Matthias Eltschka** und **Sven Aeschlimann** dafür, dass wir ein so ordentliches und harmonisches Büroteam waren.

Christian Dette, **Claudius Morchutt**, **Dr. Eike Oliver Schäfer-Nolte** und **Benjamin Wurster** für die unvergesslichen Fahrten mit der Schnecke im Mini!

Dr. Liza Herrera-Diez for passing the responsibility of being the chocolate president on to me. I enjoyed a lot of lovely hours eating huge amounts of chocolate and I am convinced **Diana Hötger** will be a wonderful successor.

Dr. Theresa Lutz, **Verena Schendel**, **Sabine Abb**, **Sebastian Koslowski** für die schönen Joggingrunden um die Bärenseen und die vielen lustigen Stunden sowohl innerhalb als auch außerhalb des Instituts!

meiner Familie und bei **Simon** für die bedingungslose Unterstützung in guten wie in schweren Zeiten.